A STUDY OF THE TRAILING VORTICES
BEHIND A RING WING

Thesis by
Kwasi Kete Bofah

In Partial Fulfillment of the Requirements
for the Degree of
Doctor of Philosophy

California Institute of Technology
Pasadena, California
1975

(Submitted October 22, 1975)

ACKNOWLEDGMENTS

I wish to express my most sincere appreciation to Professor H. W. Liepmann for his advice, encouragement and inspiration. I am indebted to Professor P. G. Saffman for his constant help and invaluable suggestions. Drs. S. J. Barker and P. E. Dimotakis have given their time and help; their contributions to the research are greatly appreciated.

Much is owed to many members of the GALCIT staff. In particular, I wish to thank Mr. Vince Sodha, Mr. Earl Dahl, Mr. Ray Wagoner, Mr. Harry Hamaguchi, Mr. Tom Ward, Mr. George Lundgren and members of the Aeronautics Shop, Mrs. Karen Cheetham, and Mrs. Jean Anderson for their efforts on my behalf.

The excellent typing of the thesis is due to Mrs. Jacquelyn Beard, whose patience and understanding is deeply appreciated. Sincere thanks to Mrs. Betty Wood for her excellent drawings.

Finally I wish to thank the Governments of Ghana and the U. S. A. for making my studies in the United States possible, and the Air Force Office of Scientific Research and Caltech for support of the research.

I dedicate this work to my mother, Aframasika, and to the memory of my father, Kofi Bofah.

A STUDY OF THE TRAILING VORTICES BEHIND A RING WING

ABSTRACT

The flow field of a laminar vortex wake behind a ring wing was investigated. Experiments were conducted in the GALCIT[†] Low Speed Water Channel, using laser Doppler velocimetry techniques to measure vertical and axial velocity components in the trailing vortex wake. A thin cylindrical ring wing model was tested at various axial angles of attack and free stream velocities. Velocity profiles were measured at several downstream stations from the trailing edge to 45 wing diameters downstream.

The inviscid roll-up of the trailing vortex sheet shed by a ring wing was numerically examined. A line vortex representation was used to calculate the evolution of the initially cylindrical vortex sheet. The vortex sheet was found to distort in shape and then smoothly roll up into a pair of doubly connected spirals whose centers originate from approximately the center of gravity of vorticity in the upper quadrants of the ring wing's circular trailing edge. (This origin is at an angle of 38° measured from the horizontal wing diameter.)

The experimental and flow visualization results are consistent with the numerical data and show that a pair of counter-rotating

---

[†] Graduate Aeronautical Laboratories, California Institute of Technology.

vortices do develop from the rolling up of the vortex sheet shed by a ring wing in a nonaxial flow. The vortices trail, downstream of the wing, with their vorticity centroids spaced by $\pi/4$ wing diameters.

Saffman and Moore's theory of axial flow in laminar trailing vortices was adapted and found to be in reasonable agreement with the experimental results. The flow field near the trailing edge was found to be in fair agreement with Weissinger's inviscid calculations.

TABLE OF CONTENTS

TABLE OF CONTENTS (cont.)

APPENDICES

LIST OF SYMBOLS

A	aspect ratio, D/C
A_s	constant relating to radius of spiral
a_s^*	dimensionless radius of spiral
(a, b)	Cartesian coordinates of point vortex for the case M = 2
B_{ji}	Birnbaum coefficients
$B_{ji}^{(0)}$	Birnbaum coefficients per unit angle of attack
b	elliptic wing span
b_j	summation parameter
C	wing chord
c	speed of light
C_o	constant
C_1	constant
C_L	lift coefficient, $L/\frac{1}{2}\rho U^2 S$
$C_{L_{\alpha}o}$	slope of lift versus angle of attack in degrees
C_{Di}	induced drag coefficient, $D_i/\frac{1}{2}\rho U^2 S$
D	ring wing diameter
D_i	induced drag
D'	trailing vortices distance of separation
d_f, d_1, d_2	interference fringe spacing
E	elliptic integral of the first kind
$F_j(\eta)$	tangential velocity function
${}_1F_1$	confluent hypergeometric function
f	fraction of net vorticity rolled up into spiral

LIST OF SYMBOLS (cont.)

$G_j(\eta)$	axial velocity function
$g_1(\xi)$	vorticity density function
$g(x)$	function
$H(\eta)$	axial velocity function
i	complex number, $\sqrt{-1}$
i, j, k	indices
J_o	initial angular impulse
J_r	angular impulse after roll-up
K	elliptic integral of the second kind
K. E.	kinetic energy
$\underset{\sim}{k}_s$	unit vector in the direction of scattered light
$\underset{\sim}{k}_i$	unit vector in the direction of incident beam
L	lift force
M	number of point vortices per half wing in numerical calculation
n	constant
$\underset{\sim}{n}_i$	unit vector in the direction of particle velocity component sensed by LDV
$P_j(\eta)$	pressure function
p	pressure
Q_j	summation parameter
q	dynamic pressure, $\frac{1}{2}\rho U^2$
R	ring wing radius
R_D	Reynolds number based on ring wing diameter, UD/ν
R_b	Reynolds number based on wing span

LIST OF SYMBOLS (cont.)

r, θ	polar coordinates
r_c	line vortex cut-off radius
r_c^*	dimensionless cut-off radius, r_c/R
r_o	vortex core radius defined by edge of irrotational flow
r_1	vortex core radius defined by radial position of maximum tangential velocity
S	wing surface area
s	arc length
s_o	arc length separating neighboring point vortices in numerical calculation
$\bar{s}$	centroid of vorticity in vortex sheet segment
T	orbital period
T^*	dimensionless orbital period
t	time
t_f	scattering particle time of flight between interference fringes
t^*	dimensionless time
t_o^*	dimensionless time when roll-up of vortex sheet begins
t_r^*	dimensionless time when chaotic motion of point vortices begins
t_c^*	dimensionless time for 'complete' roll-up of vortex sheet
U	free stream velocity or wing speed
u, v, w	velocity components in x, y, z axes
u_2	velocity component
u_t	radial velocity

LIST OF SYMBOLS (cont.)

v_θ	tangential velocity
$\underset{\sim}{V}_i$	scattering particle instantaneous velocity vector
$V_\perp$	velocity component sensed by LDV
$\overline{V}_\perp$	mean velocity
$<V_\perp'>$	root mean square velocity fluctuation
W_o	induced downwash velocity
W_g	speed of descent of center of gravity of vortex system
W_g^*	dimensionless speed of descent
w^*	dimensionless vertical velocity
w_o	maximum induced downwash velocity
X	axial position from center of ring wing
X_{ac}	aerodynamic center
(x, y, z)	rectangular cartesian coordinates
x_o	axial distance from ring vortex
$x_o^* = x_o/R$	dimensionless distance
y_o^*	dimensionless lateral position of trailing vortex
Z	complex variable, $Z = y + iz$
Z_o	position of trailing vortex
z_o	vertical position of vortex center of gravity
α	angle of attack (radians)
α^o	angle of attack (degrees)
β	vortex strength parameter, $\lambda \Gamma_o/4R$
Γ	circulation

LIST OF SYMBOLS (cont.)

Γ_o	wing root circulation
Γ_i	point vortex strength
Γ_i^*	dimensionless point vortex strength, Γ_i/Γ_o
Γ_v	net vorticity rolled-up in trailing vortex
γ	parameter
ΔU	the sum of ΔU_δ and ΔU_v
ΔU_δ	axial velocity defect due to boundary layer retardation on wing surface
ΔU_v	axial velocity due to vortex pressure field
Δu_r	initial change in radial velocity on vortex sheet due to cut-off radius
Δu_θ	initial change in tangential velocity on vortex sheet due to cut-off radius
δ	boundary layer thickness
δ_o	axial vorticity on vortex core axis
(η, ζ)	rectangular cartesian coordinates
η	boundary layer variable, $r^2/4\nu t$
η_1	position of maximum tangential velocity in vortex core
Θ	variable
θ	polar angle
θ_c	angle; defined in Moore's amalgamation method
θ_o	vortex sheet roll-up origin on ring wing
$\theta, \theta_1, \theta_2$	LDV scattering angle
θ_∞	integration constant
λ	contraction factor

LIST OF SYMBOLS (cont.)

λ_o	laser wavelength
μ	micron, 10^{-4} cm
ν	kinematic viscosity
ν_s	frequency of scattered light
ν_o	frequency of incident beam
ν_D	Doppler shifted frequency
ξ	variable, $2X/c$
π	constant, 3.14159
ρ	fluid mass density
σ	refractive index
τ	parameter, $\lambda^2 \nu t/R^2$
φ	polar angle
φ_o	vortex sheet roll-up origin on ring wing
χ_δ	constant based on boundary layer thickness
ψ	LDV optics angle
$\Omega(\xi)$	vorticity density
$\omega(\varphi)$	vorticity distribution
ω_o	vorticity in segment of vortex sheet

LIST OF FIGURES

LIST OF FIGURES (cont.)

I. INTRODUCTION

Trailing vortices are known to form by the roll-up of the vortex sheet shed by a lifting surface. This phenomenon was first depicted by Prandtl in 1922. His now famous sketch is reproduced in Figure 1a. Briefly described, the edges of the vortex sheet emanating from the wing's trailing edge roll up into a pair of tightly wound spirals, as a consequence of self-induced velocities. During the roll-up process, vorticity tends to concentrate in the interior of the spirals. In real fluids, viscosity smoothes out the turns of the spirals to form the core of the trailing vortex.

The viscosity of the fluid is responsible for the formation of the vortex sheet, and thus the sheet will possess a finite thickness. However, for vanishingly small viscosity, the sheet would take on the form of a mathematical discontinuity surface on which vorticity is distributed. Therefore, viscosity is neglected to permit inviscid calculations of the roll-up. Such inviscid calculations made in the 1930's gave valuable insight into the shape of the rolled-up spiral.

Kaden (1931, Ref. 1) simulated the roll-up behind a planar wing by analytically calculating the roll-up of a semi-infinite vortex sheet. An identical problem was treated by Anton (1939, Ref. 2) who studied the vortex formation at the edge of an impulsively started flat plate. The results of both investigations gave the shape of the inner turns of the spiral to be of the form $r = \text{const. } \theta^{-2/3}$ (where r and θ are the polar coordinates), thus confirming a result of much earlier work by Prandtl (1922, Ref. 3).

Prandtl's general investigation of vortex formation in an ideal fluid revealed a rolled-up spiral of the type $r = \text{const.}\,\theta^{-n}$ where n is constant and $0 < n < 1$. In connection with these results, it is worth mentioning a much more recent work by Saffman and Moore (1974, Ref. 5). By physical arguments of vortex motion in an inviscid flow, they derived the general shape of the inner portion of the rolled-up spiral behind a lifting planar wing, whose tip loading is proportional to y^{1-n}, where y is measured from the tip of the wing. The resulting spiral was found to be described by $r = \text{const.}\,\theta^{-1/1+n}$ where, for example, $n = \frac{1}{2}$ corresponds to an elliptic wing, in agreement with Kaden's result by a lengthier method. The limiting cases $n = 0$ and $n = 1$ correspond, respectively, to a delta wing and a wing with constant loading.

Until recently the problem of trailing vortex formation had ceased to be one of the leading areas of aerodynamic interest. High interest in aircraft wake turbulence due to heavily loaded aircraft (e.g., jumbo jets) has recently stimulated numerous theoretical and experimental investigations of trailing vortices. These studies have been mainly concerned with planar wings like elliptic and delta wings (Refs. 8 and 9). The least popular lifting surface as an aerodynamic research subject is probably the ring wing. As usual it lags behind planar wings in aerodynamic developments.

To date, research interest has been confined to the aerodynamic characteristics of the ring wing. Perhaps the most comprehensive works on the ring wing are the calculations of Weissinger (Refs. 21 through 24) by linearized lifting surface theory, and the experimental investigation of Fletcher (Ref. 29). The vortex wake of the ring wing, however, has hardly been investigated.

It is the purpose of this study to investigate the formation of trailing vortices by the roll-up of a ring wing generated vortex sheet and to measure, in particular, the flow field associated with the trailing vortices behind a ring wing in a nonaxial subsonic flow. In addition to research interest in the studies of vortex sheet roll-up, the ring wing has some important practical applications as a lifting surface. The ring wing is used as a lifting surface in VTOL-STOL aircraft and as an antidrag cowl in propulsive systems, e.g., propeller shrouds and jet engine intakes.

The simplest flow past a ring airfoil is that of an axially symmetric flow. In this case, there is no net lift on the ring wing and, therefore, no trailing vortex sheet (Ref. 12). The surface of the wing is characterized by bound ring vortices only. In the present investigation, the case of nonaxial flow is studied. A thin cylindrical ring wing, placed at a small axial angle of attack, develops a pressure distribution on both the inner and outer surfaces of the wing so as to cause cross-flows on the wing surface, as depicted in Figure 2. Fluid will tend to flow on both surfaces from the pressure side to the suction side. When the inner and outer flows meet at the trailing edge, vorticity is generated by the action of viscosity. Vorticity thus generated lies, for vanishingly small viscosity, on a cylindrical surface of discontinuity. In a plane perpendicular to the axis of the cylinder, the trace of the vortex sheet is a circle with radius equal to the radius, R, of the ring wing.

The vorticity distribution on vortex sheets generated by elliptic wings, say, and by leading edge separation over slender wings (e.g., delta wings), is characterized by singularities that serve as the origins of the roll-up process. By contrast, a ring wing generates a vortex sheet whose vorticity distribution is free of any singularity. Consequently, the origin of roll-up on the ring wing itself is not obvious. The initial distribution of vorticity on the cylindrical vortex sheet, $\omega(\varphi)$, is given in Appendix A by

$$\omega(\varphi) = 2\, W_o \sin\varphi \,, \qquad 1.1$$

where W_o is the initially induced velocity inside the cylinder, and φ is the polar angle measured from the bottom of the median plane of symmetry.

A steady three-dimensional calculation of the roll-up is highly intractable. For light loading (i.e., for small angles of attack) and/or large downstream distances, an approximation may be made by replacing the steady three-dimensional flow by an equivalent unsteady two-dimensional flow. The problem is treated numerically in Section II, using a discrete point vortex simulation of the cylindrical vortex sheet. A schematic drawing of the roll-up is shown in Figure 1b. The roll-up is very gradual and should not, therefore, significantly affect the aerodynamic characteristics of the ring wing.

In the second half of this study, the roll-up process of the vortex sheet into a pair of trailing vortices and the associated flow field are both investigated by direct measurement of the velocity field. The experimental investigation is confined to laminar flow.

In, perhaps, the first velocity measurements in a trailing vortex, Fage and Simmons (1925, Ref. 28) employed both hot wire and static pressure probes. The former technique showed axial velocity excess, whereas the latter indicated a deficit. Similar results have also been reported by recent investigators. The fact that axial velocities exist in tip vortex cores is well established (Ref. 8). However, because of flow disturbances caused by probes, whether an excess or defect occurs is not experimentally clear.

Trailing vortices, particularly laboratory generated vortices, are very sensitive to any probe placed in the vortex core, and the probe may even cause vortex breakdown. A vortex which finds a probe in its core will tend to wander around the probe. Such "vortex wandering" could cause drastic changes in the vortex structure and, thus, alter the flow field inside the core. The "vortex wandering" phenomenon is primarily due to free stream velocity fluctuations. Its effect on the structure and flow field of the vortex has been discussed in Reference 25. To avoid uncertainties in the vortex flow field, a velocity anemometry technique which is free from disturbing the flow is advised.

Currently, the laser-Doppler velocimetry (LDV) technique is the only one which guarantees no flow disturbance. In addition, the LDV provides high spatial resolution. Some excellent LDV measurements in trailing vortices have recently been reported (Refs. 25 and 26) and have resolved the uncertainty in the direction of axial flow in the vortex core.

Single scattering particle LDV (described in Section IV) was used in this investigation. The experiments were conducted in the GALCIT Low Speed Water Channel which has a very low turbulence level, and therefore "vortex wandering" due to free stream fluctuations was practically eliminated. In addition to its advantage of producing high Reynolds number at relatively low channel speeds, the water channel facilitated flow visualization techniques. Furthermore, the water naturally contained sufficient light scattering particles to provide good Doppler signals without any seeding, as may be found necessary in wind tunnels.

Existing theory on laminar trailing vortices is adapted in Section III and compared to the experimental results in Section V.

II. NUMERICAL CALCULATIONS

II. 1 Approximations of the Vortex Sheet

Calculation of the steady three-dimensional flow behind the ring wing is an intractable problem. Therefore, the usual approximation is made. Time is introduced by $t = x/U$ (where x is in the downstream direction and U is the freestream velocity), and an equivalent unsteady two-dimensional flow is instead studied. The bound ring vortices are thus ignored, and the trailing vortex lines which bend in practice are assumed straight and parallel, extending in both directions to infinity. Such an approximation is of course not expected to represent conditions in the immediate neighborhood of the wing.

With the above approximation, the problem is restated thus: at time $t = 0$ an infinite cylindrical vortex sheet whose constituent vortex lines are straight and parallel to the x-axis intersects the z-y plane in the circle $r = R$, where R is the radius of the ring wing. The initial strength of the vortex sheet (see Appendix A) is given by

$$\omega(\varphi) = \frac{\Gamma_o}{R} \sin\varphi \qquad 2.1$$

where Γ_o is the root circulation. The flow is inviscid and incompressible. The problem is to determine, in the course of time, the evolution of the vortex sheet in the z-y plane.

The equation of the vortex sheet in time is obtained by solving the nonlinear singular integro-differential equation given by Saffman (1974, Ref. 4) in the form

$$\frac{\partial}{\partial t}\,\overline{Z}\,(\Gamma,t) = -\frac{i}{2\pi}\,⨍\,\frac{d\Gamma'}{Z(\Gamma,t) - Z(\Gamma',t)} \qquad 2.2$$

where the bar through the integral sign implies the Cauchy principal value of the integral. The bar over Z denotes the complex conjugate of $Z = y\,(\Gamma,t) + i\,z\,(\Gamma,t)$, where $y(\Gamma,t)$ and $z(\Gamma,t)$ are the parametric representation of the sheet. The circulation Γ is used as a Lagrangian coordinate by

$$\Gamma = \int^{s} \omega(s,t)\; ds \qquad 2.3$$

where

$$\omega(s,t) = \frac{d\Gamma}{ds} \qquad 2.4$$

and $\omega(s,t)$ is the strength of the vortex sheet at time t as a function of arc length s. The initial condition for a vortex sheet generated by a ring wing is

$$Z(\Gamma,0) = \pm\, R\left[1 - (\Gamma/\Gamma_o)^2\right]^{\frac{1}{2}} \pm\, iR\Gamma/\Gamma_o,\quad 0 \le \Gamma \le \Gamma_o \qquad 2.5$$

Perhaps it may be emphasized here that Equation 2.2 is a two-dimensional approximation of the steady three-dimensional problem which, as mentioned before, is intractable. In the two-dimensional approach, the bound vortices (and the starting vortices) are displaced to infinity. In other words, Equation 2.2 describes the flow in the Trefftz plane where the downwash is twice that at the lifting line on the wing. (In practice, most of the errors introduced by ignoring the bound vortices occur within the first wing span distance in the wake.) Furthermore, vorticity is not quite transported downstream at the freestream velocity as assumed by the two-dimensional approach. In addition to lateral displacements (as borne out by results of the numerical calculation in Section V.1) there is stretching of the vortex lines, particularly in the low pressure vortex core. This changes vorticity but not circulation. The two-dimensional approximation (Eq. 2.2) is valid for light wing loading and/or large downstream distances. A formal justification of replacing the steady three-dimensional flow by an unsteady two-dimensional flow is included in the appendix of Moore and Saffman's work (Ref. 5).

The above stated problem, in the form of Equation 2.2 is still intractable; however, it is stated here for future analytic investigation. Further approximation is, therefore, made to make the problem amenable to numerical computation. The usual procedure is to replace the initial continuous vortex sheet by either a number of discrete line vortices which vary in strength, or equistrength, unequally spaced vortex filaments. One then numerically follows the motion of the individual discrete vortices, due to the velocity field induced on each vortex by the remaining vortices.

Rosenhead (1931, Ref. 10) was the first to use such a discretization method. He used this approximation to study the Helmholtz instability problem. Westwater (1935, Ref. 11) later used the same technique to calculate the roll-up of the vortex sheet shed by an elliptically loaded wing. Both studies resulted in a smooth roll up of the vortex sheet into a spiral where vorticity concentrated. However, Birkhoff and Fisher (1959, Ref. 13) criticized and showed Rosenhead's analysis to be doubtful. They further pointed out that an array of discrete vortex filaments in a nonviscous fluid might exhibit a tendency towards randomization of position; results of their calculation of the same problem substantiated their view. Hama and Burke (1960, Ref. 14) also reexamined the Helmholtz instability problem and encountered the same randomization effect. By taking smaller time steps of integration and redistributing the initial vorticity in the sinusoidally perturbed sheet, Hama and Burke were able to obtain a smooth roll-up but no strong concentration of vorticity resulted. It is worth noting though that Euler's step-by-step integration method in itself has a smoothing effect on the point vortices' chaotic motion inside the rolled-up spiral. This is apparently due to the cumulative errors introduced by such an integration scheme. It is believed that this could explain why Rosenhead and Westwater's calculations resulted in a smooth roll-up.

In view of Birkhoff and Fisher's criticism, Takami (Ref. 15) and Moore (Ref. 6) reexamined Westwater's calculation of vortex sheet roll up behind an elliptically loaded wing. Both investigators employed much more refined numerical calculation procedure. But still the inner point vortices moved irregularly, implying that the vortex sheet, represented by these point vortices, would have crossed itself several times. In spite of the randomization effect, Takami and Moore's results show an indication toward vorticity concentration and give a qualitative picture of the roll-up. It is in this view, to obtain a qualitative picture of the roll-up, that a similar numerical calculation is performed on the cylindrical vortex sheet shed by a ring wing.

Some successful techniques to remove chaotic motion of the point vortices have recently been presented in the literature. These are briefly described below.

II. 2 Methods to Control Chaotic Motion

a) Kuwahara and Takami's "artifical viscosity" method (Ref. 16).

In this method the induced velocity field of a line vortex is replaced by the velocity field of a viscous diffusing vortex with a core radius $r_c = (4\nu t)^{\frac{1}{2}}$, where the kinematic viscosity, ν, is chosen arbitrarily. Thus, the tangential velocity due to a line vortex,

$$v_\theta = \frac{\Gamma}{2\pi r} , \qquad 2.6$$

is replaced by that due to a diffusing line vortex,

$$v_\theta = \frac{\Gamma}{2\pi r} [1 - \exp(-r^2/4\nu t)], \qquad 2.7$$

where r is measured radially from the point vortex, around which the circulation is Γ. Kuwahara and Takami's results, from recalculating the vortex sheet roll-up behind an elliptically loaded wing, showed rather remarkably smooth roll-up. However, it is not clear what value of ν should be most appropriate.

b) Chorin and Bernard's cut-off radius method (Ref. 17). This approach is analogous to the artificial viscosity method described above except that unlike the artificial viscosity the effect of the cut-off radius is not cumulative. The velocity field is modified by

$$v_\theta = \frac{\Gamma}{2\pi r}\,, \quad r > r_c$$
$$= \frac{\Gamma}{2\pi r_c^2}\, r, \quad r \le r_c \;. \qquad 2.8$$

The cut-off radius r_c is taken to be in the order of the separation of the initially closest pair of vortices.

Methods a) and b) effectively make the velocity field of the point vortex bounded, and thus suppress the irregular motion of vortices which may come too close together within the rolled-up portion of the vortex sheet.

c) Moore's amalgamation method (Ref. 7).

This method is based on the fact that the velocity field of the inner portion of the rolled-up spiral is approximately axisymmetric. Instead of representing the inner turns of the spiral by a finite number of discrete point vortices, the inner spiral turns are represented by a single tip vortex placed at the center of the spiral. This is accomplished numerically in the following way.

Numbering the point vortices from the tip of the wing, the first point vortex represents the tip vortex. In the course of the numerical integration, the angle subtended by a vector connecting the second and third vortices, and a vector connecting the third and fourth vortices is examined at each integration time step. When this angle exceeds θ_c, vortices one and two are combined to form the new tip vortex with strength equal to the combined strength of the pair. The tip vortex is then placed at the centroid of the pair.

Moore found $\theta_c = 90^\circ$ adequate to prevent randomization of position.

d) Redistribution of vortices, Fink and Soh (1974, Ref. 18). In this technique the vortex sheet is divided into a number of small segments of equal length. Each segment is then represented by a point vortex whose circulation equals the circulation around the segment. The representative point vortex is placed at the mid-point of the segment. (Note that in the previous methods the point vortex is placed at the centroid of vorticity of the segment. The mid-point position makes a logarithmic term in the induced velocity, introduced by the Cauchy principal value, vanish.) The motion of the array of point vortices is followed by Euler's step-by-step integration scheme. At each time step the point vortices become unequally spaced. To ensure that the vortices remain equispaced in the course of time, a new set of vortices are created by again discretizing the new sheet represented by the previous set of discrete vortices. (The strength of the sheet is found by interpolation.) Thus the new set of vortices will have different strengths and positions but remain equispaced as integration proceeds.

Fink and Soh used their method successfully in treating various vortex sheet roll-up problems including that of Westwater and Rosenhead. No randomization of position was encountered. Furthermore, increasing the number of segments bettered the calculation in contrast to previous techniques. This is probably the most successful method. At least no ambiguous parameter like a cut-off radius is introduced. However, the Euler integration smoothing effect as mentioned before cannot be discounted.

It would be interesting to check this approach by other integration schemes such as the Runge-Kutta method.

In a way, this method of redistributing the vortices at each time step is analogous to Moore's amalgamation method. Both methods have the effect of representing the inner portion of the rolled-up spiral with fewer and fewer but stronger discrete vortices to eliminate spurious fluctuations during the cause of integration.

II. 3 Calculations on the Ring Wing

The discretization approximation scheme is used to numerically calculate the roll-up of the cylindrical vortex sheet behind a ring wing. The vortex sheet is divided into 2M arcs of equal length. Each segment is then represented by a point vortex, with strength Γ_i equal to the circulation around the segment, placed at the centroid of vorticity of the arc. To reduce spurious fluctuations of vortices within the spiral, a cut-off radius r_c is introduced as in Equation 2.7. The cut-off radius is kept constant in time and is taken to be on the order of half the arc length.

A system of ordinary differential equations to be solved numerically instead of Equation 2.2 is

$$\frac{\partial}{\partial t} \bar{Z}_k = - \frac{i}{2\pi} \sum_{j \neq k}^{2M} \frac{\Gamma_i}{Z_k - Z_j} \left[1 - \exp\left(- |Z_k - Z_j|^2 / r_c^2 \right) \right] . \qquad 2.9$$

Here $Z_k = y_k + iz_k$ is complex, and the bar over Z indicates the complex conjugate. The initial strength of the vortex sheet is $\Gamma_o R^{-1} \cos\theta$, where θ is measured from a horizontal diameter of the circular cylindrical sheet, and Γ_o is the root circulation.

It is convenient to introduce a dimensionless time, t^*, defined by

$$t^* = \frac{4}{\pi^3} \frac{\Gamma_o}{R^2} t \quad . \qquad 2.10$$

Assuming all the vorticity per half wing is concentrated at the respective centers of gravity, $y = \pm (\pi/4)R$, to form a pair of circular trailing vortices, then $(\pi^3/4)R^2/\Gamma_o$ is the time it takes the pair of trailing vortices to descend through their distance of horizontal separation, $(\pi/2)R$. The strengths of the point vortices are normalized by Γ_o and lengths are nondimensionalized with R.

Equation 2.9 is numerically integrated forward in time on the IBM 370-158 batch processor using the fourth order Runge-Kutta integration method. The symmetry of the sheet about the plane of symmetry, $y = 0$, is used to save computing time. In using the Runge-Kutta method, the time step is determined by the shortest time scale. For the equisegmented sheet vortex subdivision mode (approximately equispaced point vortices), the shortest time scale is the least orbital period of a pair of the point vortices. For a pair of vortices with separation s_o and strength Γ, the orbital period is $4\pi^2 s_o^2/\Gamma$. The closest and strongest pair in the point vortex approximation of the cylindrical vortex sheet is the two point vortices near the horizontal diameter where vorticity is maximum. The separation of this pair is approximately $\pi R/M$, and their strength is $\Gamma_o \pi/M$. The orbital period of the pair is then $4\pi^3 R^2/M\Gamma_o$. Thus, one must ensure that the integrating time step dt^* satisfies the condition $dt^* << 16/M$. (Note that this is a less restrictive condition than $dt^* << 8/\pi M^2$, the condition for the case of an elliptic wing generated vortex sheet (Ref. 7)).

The invariants of the vortex motion are also examined. These invariants (Refs. 19 and 20) are:

the 'vertical impulse', $$\sum_{i=1} \Gamma_i \, y_i$$

the 'angular impulse', $$\sum_{i=1} \Gamma_i \, |Z_i - Z_o|^2$$

about the centroid of vorticity, Z_o, and

the 'energy' $$\sum_{i \neq j} \sum \Gamma_i \, \Gamma_j \log |Z_i - Z_j| \quad .$$

Due to symmetry and the fact that vorticity generated by each half of the wing has opposite signs, the 'angular impulse' invariant is automatically preserved and needs not be calculated. The results of the computation are presented in Section V.

II. 4 Roll-up Rate of the Vortex Sheet

Some insight into the roll-up rate of the vortex sheet behind the ring wing may be gained by the following approximation. Consider the cylindrical vortex sheet to be represented by four point vortices placed at the centroid of vorticity of each quadrant (Fig. 6). Each vortex pair has strength $\pm \Gamma_o$ and is placed at the coordinates $(\pm a, \pm b)$, where $a = \pi/4$ amd $b = \frac{1}{2}$, taking the radius of the wing $R = 1$. Each pair of vortices with the same sign of circulation (e.g., the pair at (a,b) and $(a,-b)$) will orbit on an orbital path centered at the center of gravity of the pair as the system of the four vortices descend. Consider the moving coordinates (η, ζ), with the origin at the center of gravity of the pair. The orbital path† can easily be found analytically from the energy invariance of the four-vortex system to be

$$\eta^2 + \zeta^2 = (a^2 - \eta^2)(a^2 + \zeta^2)/C_o \qquad 2.11$$

where $$C_o = a^2 (1 + a^2/b^2) \quad .$$

After lengthy algebra, the orbital period T is obtained as

$$T = \frac{2\pi^3}{C_1} \frac{R^2}{\Gamma_o} \left[K(C_1) - \frac{1}{1-C_1^2} E(C_1) \right] , \qquad 2.12$$

where $C_1 = (1 + a^2/b^2)^{-1}$, K and E are the complete elliptic integrals of the first and second kinds, respectively. With $a = \pi/4$ and $b = \frac{1}{2}$, the orbital period is

$$T \simeq 15.51 \; R^2/\Gamma_o \, . \qquad 2.13$$

It is assumed that the vortex sheet may be considered essentially rolled-up by the time the upper vortex (Fig. 6) regains its original lateral position of $y = (\pi/4)R$ (i.e., $\zeta = 0$). This time, t_c^*, is half the orbital period. Thus $t_c^* \simeq 1.0$. In terms of downstream distance from the trailing edge of the ring wing, replacing t by x/U,

---

† This is a special case of a vortex pair with the same sign of circulation near a wall as treated in Reference 34.

$$\frac{x}{D} = \frac{\pi^3}{8}\left(\frac{\Gamma_o}{UR}\right)^{-1} t^* \qquad 2.14$$

and roll-up is considered complete when, $t_c^* \simeq 1.0$. Thus

$$\left(\frac{x}{D}\right)_c = \frac{\pi^3}{8}\,\frac{UR}{\Gamma_o} \qquad 2.15$$

$$= \frac{\pi^3}{16}\,\frac{A}{C_L} \quad .$$

From lifting line considerations $\Gamma_o = UCC_L$, where C is the chord length, C_L is the wing lift coefficient, D is the wing diameter and A = D/C is defined as the aspect ratio. (For an elliptic wing, Kaden (Ref. 1) calculates $x/b = 0.28\ A/C_L$ for the downstream station where the vortex sheet may be considered essentially rolled up. Here, b is the wing span and A = b/C).

The above approximation is based on the result that the cylindrical vortex sheet rolls up into a pair of trailing vortices whose centers are located at $y = \pm\ (\pi/4)R$. Approximately, the centers of the trailing vortices originate from the centroids of vorticity in the upper quadrants (Fig. 3). The path of the single point vortex (representing vorticity in the upper quadrant) is assumed to roughly simulate the path of the center of the rolled-up spiral.

Equation 2.15 is compared to the numerical and experimental results and found to be in fair agreement (Section V).

III. THEORETICAL CONSIDERATIONS

III. 1 Inviscid Vortex Flow Field

The structure of the trailing vortex is known to depend on the geometric configuration of the wing. Moore and Saffman (Ref. 5) have recently presented a theory for the structure of a laminar trailing vortex generated by a finite wing with a tip loading of the form $\Gamma(y) \sim y^{1-n}$. Here n is a positive constant with $0 < n < 1$, and y is measured from the wing tip. Their work is adapted to obtain a theory to predict the flow field in the trailing vortex formed behind a ring wing. Detailed reasoning in Reference 5 is not produced here.

The rolled-up vortex is assumed to be axially symmetric, and the spiral structure of the inviscid vortex is neglected. The approximate distribution of circulation $\Gamma(r)$ in the central portion of the vortex is determined to be (Appendix B)

$$\Gamma(r) = \frac{\pi}{2} \Gamma_o \sin \lambda r/R \qquad 3.1$$

and the tangential velocity due to inviscid flow between spiral turns is given by

$$v_\theta = \beta \frac{\sin \lambda r/R}{\lambda r/R} , \qquad 3.2$$

where

$$\beta = \lambda \Gamma_o/4R . \qquad 3.3$$

Here R is the radius of the ring wing, Γ_o is the root circulation and λ is the compression (or contraction) factor (Appendix C). The pressure field developed by the inviscid roll-up is determined from the equation

$$\frac{1}{\rho}\frac{\partial p}{\partial r} = \frac{v_\theta^{\,2}}{r} \qquad 3.4$$

which is obtained from the balance between radial pressure gradient and centrifugal force. The tangential velocity, v_θ, given by the sine function in Equation 3.2, is now replaced by a series of finite terms,

$$v_\theta \simeq \beta \sum_{j=0} (-1)^j \frac{(\lambda r/R)^{2j}}{(2j+1)!} \, , \qquad r \to 0 \quad . \qquad 3.5$$

Equation 3.5 is much easier to manipulate than Equation 3.2; and, in any case, it is a fair approximation in the inner portion of the vortex where the present analysis is concerned.

Equations 3.4 and 3.5 then give

$$\frac{p}{\rho} \sim \frac{\beta^2}{2}\left[\ln\left(\frac{\lambda r}{R}\right)^2 + \sum_{j=1} \frac{b_j}{j}(\lambda r/R)^{2j}\right] \, , \qquad \text{as } r \to 0 \qquad 3.6$$

where

$$b_j = (-1)^j \sum_{k=0}^{j} \left[(2k+1)!\,(2j-2k+1)!\right]^{-1}$$

and R/λ have been used as a convenient length scale in the logarithmic term.

The axial velocity u caused by the inviscid roll-up can now be determined by making the light loading approximation that $u << U$. Then, in the central region of the rolled-up vortex, the requirement that total head be conserved leads to

$$(p - p_o)/\rho + uU + \tfrac{1}{2} v_\theta^{\,2} = 0 \quad . \qquad 3.7$$

Substituting Equations 3.5 and 3.6 into Equation 3.7, one obtains

$$u \sim -\frac{\beta^2}{2}\left[1 + \ln\left(\frac{\lambda r}{R}\right)^2 + \sum_{j=1} b_j\left(1+\frac{1}{j}\right)\left(\frac{\lambda r}{R}\right)^{2j}\right] \qquad 3.8$$

$$\text{as } r \rightarrow 0 \quad .$$

It is seen that the inviscid roll-up introduces singularities in both the pressure and axial velocity on the axis of the vortex core. Viscous effects will remove these singularities. The finite tangential velocity on the core axis will be reduced to zero by viscosity. It is worth noting that $u > 0$ at $r = 0$ is in agreement with results in Reference 5.

III. 2 Viscous Effects

Viscous effects are known to be confined to a slender inner core of the vortex. A solution is sought for this viscous core by using the inviscid solution in Section III. 1 as an initial condition to solve the parabolic equation of boundary layer type approximations, viz.

$$\frac{\partial v_\theta}{\partial t} = \nu\left(\frac{\partial^2 v_\theta}{\partial r^2} + \frac{1}{r}\frac{\partial v_\theta}{\partial r} - \frac{v_\theta}{r}\right) \qquad 3.9$$

$$\frac{v_\theta^{\,2}}{r} = \frac{1}{\rho}\frac{\partial p}{\partial r} \qquad 3.10$$

and

$$\frac{\partial u}{\partial t} = -\frac{1}{\rho U}\frac{\partial p}{\partial t} + \nu\left(\frac{\partial^2 u}{\partial r^2} + \frac{1}{r}\frac{\partial u}{\partial r}\right) \qquad 3.11$$

where, in assuming light loading, t replaces x/U and axial symmetry is assumed. The flow is rotational, laminar and incompressible; the boundary conditions are that $v_\theta = 0$ and u is finite at $r = 0$; and that as the boundary layer variable $r/(\nu t)^{\frac{1}{2}} \to \infty$, the solution matches the inviscid outer solution. A solution is sought by introducing the similarity variable

$$\eta = \frac{r^2}{4\nu t} \quad \infty > \eta > 0 \quad . \tag{3.12}$$

Then the inner solution for v_θ is of the form

$$v_\theta = \beta \sum_{j=0} \left(\frac{\lambda^2 \nu t}{R^2}\right)^j F_j(\eta) \ . \tag{3.13}$$

Substituting Equation 3.13 into 3.9, one obtains the set of ordinary differential equations

$$F_j'' + (1+\frac{1}{\eta})\, F_j' - \left(\frac{j}{\eta}+\frac{1}{4\eta^2}\right) F_j = 0, \quad j = 0, 1, 2 \ldots \tag{3.14}$$

where

$$F_j(0) = 0 \tag{3.15}$$

and

$$F_j(\eta) \to \frac{(-1)^j 4^j \eta^j}{(2j+1)} \quad \text{as } \eta \to \infty \quad . \tag{3.16}$$

Solving, one gets

$$F_j(\eta) = \frac{\pi^{\frac{1}{2}}}{2} \frac{(-1)^j}{j!} \eta^{\frac{1}{2}} \ {}_1F_1\left(\tfrac{1}{2} - j;\ 2;\ -\eta\right), \tag{3.17}$$

and

$$v_\theta = \beta \frac{\pi^{\frac{1}{2}}}{2} \eta^{\frac{1}{2}} \sum_{j=0} (-1)^j \frac{\tau^j}{j} \ {}_1F_1\left(\tfrac{1}{2}-j;\ 2;\ -\eta\right), \tag{3.18}$$

$$\tau = \lambda^2 \ \nu t/R^2$$

where ${}_1F_1$ is a confluent hypergeometric function (p. 504, Ref. 41). It is worth noting that the first term in Equation 3.18 is in agreement with the solution in Reference 5 for n = 0. v_θ is plotted in Figure 10 for different τs. The peak circumferential velocity and the core radius are then obtained and plotted in Figure 12. The core radius is given approximately by

$$r_1 = 1.42\lambda^{-0.43} (\nu t/4R^2)^{0.28} D. \qquad 3.19$$

The pressure can now be determined by substituting Equation 3.13 into Equation 3.10 and integrating to give

$$\frac{p}{\rho} = \frac{\beta^2}{2} \sum_{j=0} \tau^j P_j(\eta) \qquad 3.20$$

where
$$P_j(\eta) = \int_\eta^\infty Q_j(\eta)\, d\eta, \qquad 3.21$$

and
$$Q_j(\eta) = (-1)^j \frac{\pi}{4} \sum_{k=0}^{j} [k!(j-k)!]^{-1} \; {}_1F_1^{(k)} \; {}_1F_1^{(j-k)} \qquad 3.22$$

where
$${}_1F_1^{(k)} = {}_1F_1\,(\tfrac{1}{2} - k;\ 2;\ -\eta) \quad . \qquad 3.23$$

The pressure checks with the asymptotic value and can be evaluated numerically. For small τ the dominant term is given by

$$P_o(\eta) = \text{Const.} + \ln\tau + \int_0^\eta Q_o(\eta)\, d\eta \quad . \qquad 3.24$$

Knowing the pressure enables the axial velocity perturbation u to be determined. Writing u in the form

$$u = -\frac{\beta^2}{2U}\left[(\ln\tau)\, H(\eta) + G_o(\eta) + \sum_{j=1} \tau^j G_j(\eta) \right] \qquad 3.25$$

and substituting with Equation 3.20 into Equation 3.11, a set of ordinary differential equations is obtained by equating coefficients of $\ell n \tau$ and τ^j. The result is

$$\eta H'' + (\eta + 1) H' = 0 \qquad 3.26$$

$$\eta G_o'' + (1 + \eta) G_o' = H - 1 + \eta Q_o, \qquad 3.27$$

and

$$\eta G_j'' + (1 + \eta) G_j' - jG_j = \eta \frac{dP_j}{d\eta} - jP_j \qquad 3.28$$

$$j = 1, 2, \ldots$$

with the boundary conditions

$$H'(0) = G_o'(0) = G_j'(0) = 0 \qquad 3.29$$

$$\left.\begin{array}{l} H \rightarrow 1 \\ G_o(\eta) \rightarrow 1 + \ell n\, 4\eta \\ G_j(\eta) \rightarrow 4^j \left(1 + \frac{1}{j}\right) b_j \eta^j \end{array}\right\} \text{as } \eta \rightarrow \infty \qquad 3.30$$

The solution of Equation 3.26 is H = 1; Equation 3.27 then becomes

$$\eta G_o'' + (1 + \eta) G_o' = \eta Q_o(\eta) \quad . \qquad 3.31$$

On and near the axis of the vortex core the dominant terms of the axial velocity are given by H and G_o. For the purpose of comparison with the experimental result, only H and G_o are solved. This should give a fair approximation to the axial velocity on the axis of the core for small τ. Furthermore, for the range of Reynolds number in which the experiment was conducted, the axial velocities developed by the roll up of the vortex sheet are small compared to velocity defects caused by boundary layer retardation on the wing surface (Fig. 11).

The solution of G_o is

$$G_o(\eta) = \frac{\pi}{4}\int_0^{\eta} \frac{e^{-z}}{z} \int_0^{z} \zeta\, e^{-\zeta} \left[{}_1F_1\,(3/2;\ 2;\ \zeta)\right]^2 d\zeta\, dz \qquad 3.32$$

$$+ \text{ constant}$$

where the constant is determined by matching G_o less the constant (which can be easily evaluated numerically) with its asymptotic value. In fact, a check of Equation 3.32 shows that $G_o \rightarrow \text{const.} + \ell n\, \eta$. The value of G_o on the core axis is found to be 3.08, and

$$\Delta U_v(0) = -\frac{\beta^2}{2U}\left[3.08 + \ell n\, \tau - 0(\tau)\right], \quad \tau << 1 \qquad 3.33$$

where

$$\tau = \frac{\lambda^2 \nu t}{R^2} \qquad 3.34$$

The contribution of axial velocity by boundary layer retardation on the core axis is estimated in Reference 5; for constant wing chord, C, it is given by

$$\Delta U_\delta(0) = \chi_\delta\, \lambda\, (C/x)^{\frac{1}{2}} \quad . \qquad 3.35$$

The value of the constant χ_δ is dependent on whether displacement or momentum thickness is used in determining the boundary layer thickness. In this work it seems more appropriate to use the momentum thickness rather than the displacement thickness since roll-up does not occur immediately at the trailing edge of the ring wing. Roll-up is delayed, consistent with light loading approximation, to far downstream from the trailing edge. Furthermore, as pointed out in Reference 5, the use of the momentum thickness assures the balance of the momentum flux deficit in the vortex core with the skin friction drag on the wing. Based on momentum thickness, $\chi_\delta = 0.19$. This value gives much better agreement with the experimental results (Section V) than the displacement thickness value of $\chi_\delta = 0.48$.

On the core axis the axial flow $\Delta U(0)$ is then given by the sum of $\Delta U_v(0)$ and $\Delta U_\delta(0)$; thus

$$\begin{aligned} \Delta U(0) &= \Delta U_v(0) + \Delta U_\delta(0) \\ &= -\tfrac{1}{2} \frac{\beta^2}{U} \left[3.08 + \ln\left(4\lambda^2 \frac{x}{D}/R_D\right) - \ldots \right] \\ &\quad - \chi_\delta \lambda (C/x)^{\frac{1}{2}} \end{aligned} \tag{3.36}$$

where $$4\lambda^2 \frac{x}{D}/R_D << 1 .$$

Here D is the ring wing diameter, A is the wing aspect ratio, D/C, and $R_D = UD/\nu$ is the Reynolds number. The magnitude of the two terms, Eqs. 3.33 and 3.35, is compared in Figure 11, and the general theoretical results in this section are compared to the experimental results in Section V.

IV. EXPERIMENT

IV. 1 Test Facility

The experiments of this study were conducted in the GALCIT Low-Speed Water Channel (Fig. 13). The channel has a contraction ratio of about 8:1 and a glass wall 216-inch test section of 18 x 24 inch cross section. The flow straighteners and turbulence control system in the contraction chamber consist of honeycomb, porous foam, and fine mesh screens. Additional foam attached downstream at the end of the test section serves to eliminate long wavelength surface waves.

The water channel free stream turbulence level is less than 0.1 percent. Low free stream turbulence level is particularly advantageous to the reduction of vortex wandering (Ref. 25) in trailing vortex experiments. The maximum channel speed is 90cm/sec but because of channel vibrations and depth of water, the experiment was conducted at a maximum free stream velocity of 33cm/sec.

IV. 2 Ring Wing Model and Support Mechanism

The test model employed in the experiment was a thin cylindrical ring wing. It was machined from aluminum tubing and was black anodized to protect it from corrosion. A symmetric NACA 0010 airfoil section with chord length C = 3.81 cm was used. The airfoil section had a leading edge radius of 0.011 chord lengths, a trailing edge thickness of 0.0021 chord lengths, and a maximum section thickness of 0.10 chords at 0.30 chord lengths from the leading edge. The diameter, D, of the ring wing model was 7.62 cm, giving a wing aspect ratio of $A = 2$. (The aspect ratio is defined here as the diameter-to-chord ratio, $A = D/C$.) A schematic drawing of the model and the reference coordinates used is shown in Figure 14.

The model was supported by six thin 0.0127 cm diameter stainless steel wires as shown in Figure 15. The upper four wires attached to the model (two wires on each side of the median plane of symmetry) were fastened to the inside section of a rig above the water surface. The lower two wires, attached to the bottom of the model, were fastened to a point on a small plate glued to the channel floor. The end plates of the inside section of the rig had arc slots which rode on pins fastened to the outside section of the rig. The centers of the arc slots and the bottom wires' point of attachment on the channel floor were arranged to lie on the axis of rotation for the inner section of the rig. The axis spanned the channel floor. By moving the inside section of the rig along the arc slots, the model and wire support system, as a unit, rotated about the axis without adding additional tension to the wires. In this manner the angle of attack was set. A vernier height gauge was then used to measure the angle of attack to within 0.25 degrees. The angle of attack was checked periodically during the course of the experiments and was found to be within the accuracy of measurement.

There were three main problems of concern in the use of the wire support system: Karman street vortex shedding from the wire, model vibrations, and wire breakage. Fortunately, no wire breakage was encountered and the model was free of any noticeable vibrations. Some vortex shedding from the wire were observed, but these quickly decayed within a few wire diameters. At the free stream speeds at which the experiments were run, the wire Reynolds number was about 44. (Karman street vortices are observed to begin at a Reynolds number of about 40 (Ref. 33)).

A wire support system may prove to be a problem at high free stream speeds. Neverthless, for ring wing vortex wake experiments, caution must be exercised in the use of the usual thin strut support. In preliminary tests, a thin strut was used to support the ring wing model. The strut was found to cause substantial disturbance to the vortex formation behind the ring wing. The wake from the strut got entrained into the trailing vortices during the roll up of the vortex sheet. This is the reason why a wire support system was adopted.

IV. 3 Test Conditions

Using the LDV system described in Section IV. 4, axial and vertical velocity profiles were measured at downstream stations from 0. 2 to 45 wing diameters. Horizontal traverses through the vortex core yielded the tangential velocities. Tests were run at angles of attack of 4, 7, 10 and 12 degrees at a Reynolds number (based on wing diameter) of roughly 2.7×10^4. Some measurements were obtained at lower Reynolds numbers of 1.7×10^4 x 2.1×10^4, all within laminar flow range. A wider range of

Reynolds numbers could not be tested because of limited test facilities. The measured results are presented in Section V.

IV. 4 Laser-Doppler Velocimeter (LDV)

Laser-Doppler velocimetry has proven to be very advantageous, particularly to experimental studies of trailing vortices. The LDV has several advantages over conventional velocimeters such as the hot wire and pressure probes. Perhaps the most significant advantage is that the LDV introduces no material into the flow and hence causes no flow interference. On the other hand, hot-wire and static pressure probes may cause significant interference to the flow. Vortices, in particular, are quite sensitive to probes inserted in the vortex cores. Probes thus inserted may drastically change the vortex structure and even induce vortex breakdown. It is also known that a tip vortex tends to wander around a probe inserted in the vortex core. Due to vortex wandering, the measured velocities which are time-averaged will be substantially altered from the instantaneous velocities (Ref. 25). Measured axial and peak tangential velocities will be decreased from the instantaneous velocities, and the vortex core radius will increase.

Other LDV advantages include the comparatively high spatial resolution and the linear response to velocity. High spatial resolution is particularly important in measuring the vortex core where high velocity gradients exist. Because of its linear response to velocity, the LDV requires no calibration except for an easily determined constant obtained independently by measuring an angle.

The principles behind the LDV are now well known. Only a brief account will be given here but more detailed analyses may be found in References 38 through 40. The underlying principle of the LDV is the well-known Doppler effect. Consider a sufficiently small particle moving through a measuring control volume (Fig. 16) with instantaneous velocity vector $\utilde{V}_i$. The particle receives light waves from the incident light source and scatters some of the incident light in all directions. Both receiving and scattering of light by the particle result in a frequency shift due to the Doppler effect. The frequency of scattered light, in the direction of the unit vector $\utilde{k}_s$, sensed by a detector is given by

$$\nu_s = \nu_o \left[1 + \utilde{V}_i \cdot (\utilde{k}_s - \utilde{k}_i)/c\right] \; ; \qquad 4.1$$

for particle velocities much less than the speed of light. The Doppler shift frequency ν_D is then given by

$$\nu_D = \nu_s - \nu_o = \frac{\nu_o}{c} \utilde{V}_i \cdot (\utilde{k}_s - \utilde{k}_i) \qquad 4.2$$

where c is the speed of light, ν_o is the frequency of the incident (or scattering) beam, and $\utilde{k}_i$ is a unit vector in the direction of the incident beam. The quantity ν_o/c equals the wavelength λ_o and

$$\utilde{k}_s - \utilde{k}_i = (2 \sin \theta/2)\, \utilde{n}_i \qquad 4.3$$

where θ, the scattering angle, is the angle subtended by the unit vectors, k_i and k_s; n_i is a unit vector lying in the plane of the unit vectors k_i and k_s and perpendicular to the bisector of the scattering angle.

The Doppler shift frequency (Eq. 4. 1) then becomes

$$\nu_D = \frac{2 \sin \theta/2}{\lambda_o} \underset{\sim}{V_i} \cdot \underset{\sim}{n_i} \qquad 4.4$$

and $V_\perp$, the particle velocity sensed in the direction of $\underset{\sim}{n_i}$ is

$$V_\perp = \frac{\lambda_o}{2 \sin \theta/2} \nu_D \quad . \qquad 4.5$$

Thus, if the scattered light wave is mixed with another light wave (a reference beam, say) from the same coherent light source, the beat frequency is related to the particle velocity through Equation 4. 5.

There exist different modes of LDV operation, as determined by the optical arrangement. In this study, the "local oscillator" mode, also known as the "reference scatter" method, was employed, and a five milliwatt Helium-Neon laser was used as the light source.

In the "reference scatter" method (Fig. 17), the laser beam is split into two beams by a glass beam splitter by means of partial internal reflections. The emerging beams are parallel and have unequal fractions of the laser power. The reference beam is weaker than the scattering beam which contains most of the laser power. The weaker beam may further have to be attenuated by a neutral density filter, according to the photo detector specification. Using a plano-convex lens to reduce spherical aberration, the two emerging beams are focused in the neighborhood of the focal point of the lens. The two beams meet in an overlap volume with approximately planar phase fronts. A particle which moves through the measuring volume (i. e., the overlap volume) scatters light from the scattering beam in all directions, particularly in the direction of the reference beam. A photomultiplier is aligned so that the reference beam is normally incident on the photosensitive area of the photomultiplier. Thus, the photomultiplier detects two waves: the reference beam at the laser frequency ν_o, and the wave scattered in the reference beam direction at a Doppler shift frequency $\nu_s = (\nu_o + \nu_D)$. The two normally incident waves are superimposed on the photosensitive area of the photomultiplier to yield a photocurrent whose AC component is modulated at the Doppler shift frequency, ν_D. The Doppler shift frequency is related, through Equation 4.2, to the particle velocity component, $V_\perp$, which lies in the plane of the intersecting beams and is perpendicular to the bisector of their subtended angle, θ (i. e., the scattering angle).

The photocurrent output of the photomultiplier is amplified and bandpass-filtered to remove noise outside the frequency range of interest. The output signal may then be processed in the frequency domain, the signal frequency (i. e., the Doppler shift frequency) is tracked by a phase-locked loop which produces a continuous square wave of the same frequency as the Doppler signal. A digital counter is then used to average the frequency over a fixed period of, say, 10 seconds.

A brief description of the time domain signal processing will be given here; a detailed analysis is given in Reference 35. Understanding of this system is facilitated by imagining a particle moving across the interference fringe pattern that the two intersecting beams will form on the surface of a square law detector. The linear fringe spacing, d_f, is given by

$$d_f = \frac{\lambda_o}{2 \sin \theta / 2} \qquad 4.6$$

where λ_o is the laser wavelength and θ is the scattering angle, and the particle velocity, $V_\perp$, is given by

$$V_\perp = \frac{d_f}{t_f} \qquad 4.7$$

where t_f is the particle's time of flight between fringes. The time of flight is equal to the time between zero crossings (after DC component removal) of the signal burst from the photomultiplier output. A typical photocurrent pattern (signal burst) is shown in Figure 17b. It is worth noting that the Doppler shift frequency, ν_D, equals the rate at which the particle crosses the interference fringes, i.e., $\nu_D = 1/t_f$, and therefore Equations 4.6 and 4.7 reduce to Equation 4.5.

Time-domain signal processing possesses intrinsic advantages over frequency-domain signal processing. The most important advantage is elimination of "ambiguity noise" caused by finite time of transit of the scattering particle moving through the measuring volume. The problem of "signal drop outs" (caused by the absence of a scattering particle in the measuring volume) is also nonexistent. Furthermore, the spatial resolution can be increased if the Doppler signal is processed in the time domain. The signal processor can be designed to have the capability to reject data from particle trajectories which contain less than a certain specified number of fringes. In addition, it may be specified that the signal must satisfy a preset amplitude (i. e., weak signals are rejected). In essence, a signal burst is processed if the scattering particle crosses the inner portion of the measuring volume and a signal burst is rejected if the particle crosses near the edges of the fringe pattern. Effectively, the spatial resolution is improved.

In the case of the "reference scatter" mode, ambiguity in the scattering angle, θ. still exists irrespective of the signal processing. In practice, the reference beam is heterodyned with light scattered through a small range of angles. Because of the scattering angle ambiguity, it is essential that the reference beam be aligned normal to the photosensitive area of the detector. This may be achieved by a series of pin-hole apertures aligned with the photosensitive area. The scattering angle spread is defined in terms of the effective aperture, (the smallest of reference beam diameter, pinhole aperture and photosensitive area) and the distance from the measuring control volume.

All the velocity measurements presented in this study were obtained with the single scattering particle LDV. Particles naturally present in the water channel were employed as scattering particles. No additional seeding was required. Particle time of flight, i. e., time between fringe spacings, was obtained by measuring the time between zero crossings of the photocurrent signal (after removal of the DC component). This was done using a single scattering particle LDV digital processor designed and built at GALCIT by Dimotakis and Lang (Ref. 37) which has the capabilities mentioned earlier. The time of flight of a single particle for a distance corresponding to 10 fringe spacings was measured, and the corresponding velocity was obtained from Equations 4.6 and 4.7.

For each measuring point in the flow, 256 measurements were processed. The digital data were recorded on a Kennedy Incremental 1600 Tape Recorder, and read on the IBM 370-158 Batch Processor. The mean velocities, $\overline{V}_\perp$, were computed by taking an ensemble average of the 256 samples, and the root mean square velocity fluctuations, $< V_\perp' >$, were also calculated from

$$\overline{V}_\perp = \frac{1}{256} \sum_{i=1}^{256} V_{\perp i} \qquad 4.8$$

and

$$< V_\perp' > = \left[\sum_{i=1}^{256} \frac{V_{\perp i}}{256} - \overline{V}_\perp^{\,2} \right]^{\frac{1}{2}} \quad . \qquad 4.9$$

The above equations (4.8 and 4.9) are not exact because of the sampling bias of the measurement process; however, they are valid for small local velocity fluctuations (Ref. 36). The LDV sampling bias arises from several factors. The randomly dispersed particles in the flow result in a random sampling (in time) of the velocity component. However, the rate at which scattering particles move through the measuring volume depends on the local velocity. Thus, the smapling process is coupled with the measured quantity and cannot, therefore, be treated as statistically independent. The sampling bias is further influenced by the signal processing that introduces a dead time[†] during which more particles are rejected at times when the particle flux is high than when the flux is low. The signal processing may also influence sampling bias by processing only signals from particles that cross a certain fixed number of fringes. A detailed treatment of LDV sampling bias is given in Reference 36.

A schematic representation of the LDV system in reference to the channel test section is shown in Figure 18. The reference scatter mode (Fig. 17a), as described previously, measures only one velocity component. For the purposes of the experiment, the LDV optics section was modified to accommodate a second reference beam. Introduction of a second reference beam enabled the LDV to measure two velocity components simultaneously if a duplicate signal processor were available or to ensure that at least two velocity components were measured at the same point in the flow if only one signal processor were available. There was only one signal processor.

A second reference beam was obtained by placing a second beam splitter in front of the first one to split the scattering beam again (labeled 'S' in Figures 17c and 18). Two weak parallel beams (labeled '2' and '0') emerged in addition to the scattering beam,

---

[†] Time interval after signal burst during which a signal is rejected.

such that beam '0' was centered between beams 'S' and '2'. The two beam splitters were then positioned so that beam '0' was equidistant from the rest (i.e., beams '1', '2' and 'S') which then formed the apices of a right angle triangle. The four parallel beams were then arranged on a plano-convex lens such that beam '0' hit the center of the lens and beams '1', '2' and 'S' were on an equal radius from the center of the lens. The radially positioned beams, as they emerged from the lens (assumed perfect), would lie on the surface of a cone. The central beam ('0') would be the axis of the cone with its apex at the focal point of the lens. This conical arrangement of the beams was important to ensure proper focusing in the flow after the beams refracted through the glass wall of the test section.

The central beam was used for the purpose of alignment only. Beams '1' (the first reference beam) and 'S' (scattering beam) were used to measure the axial velocity component, u, and beams '2' (the second reference beam) and 'S' were used to measure a velocity component, u_2, at an angle, ψ, to the axial velocity component. (From here on quantities subscripted by "1" and "2" refer to above described beams or the corresponding velocity components.) The vertical velocity component, w, was then calculated by resolving the two measured components. Thus

$$w = (u \cos \psi - u_2)/\sin \psi \quad . \qquad 4.10$$

The respective scattering angles, θ_1 and θ_2, and the angle ψ were measured directly to within 0.5% by projecting the beams on a vertical wall at a large distance from the lens focal point. For the measured values of $\theta_1 = 4.32^o$ and $\theta_2 = 7.28^o$, the fringe spacings (Eq. 4.6) were determined to be $d_1 = 8.38\mu$ and $d_2 = 4.99\mu$, respectively.

By observing the LDV signal burst on an oscilloscope, a particle's total time of flight through the measuring volume could be estimated. From the measured velocity of the flow (assumed equal to particle velocity) and the total time of flight, the width of the approximately ellipsoidal measuring volume was estimated to be roughly 320.0μ. The dimensions of the ellipsoidal volume were estimated to be approximately 0.9 x 0.3 x 0.3mm and 0.5 x 0.3 x 0.3mm, respectively, for the two measuring volumes.

IV.5 Traverse Mechanism

On one side of the channel the laser, with its attached optics, was mounted on a traverse mechanism which moved on all three axis (x, y, z) to position the focal volume to within 0.025 mm. The two photomultipliers (to sense the two reference beams and scattered light) were attached to a support mechanism on the other side of the channel. This support mechanism spanned the channel and was bolted to the same traverse mechanism. Thus, the photodetectors remained aligned with the reference beams as the traverse mechanism was moved. (It may be noted here that due to refraction in the water, if the optics system is moved inward toward the channel by, say, Δy, the focal volume is displaced in the same direction by an amount $\sigma \Delta y$, where $\sigma = 1.33$ is the refractive index of water.)

V. RESULTS AND DISCUSSION

V. 1 Numerical Calculation

The initial distribution of the point vortices is given by the complex[†] relationship

$$Z_{\frac{M}{2}+1-j}(0) = y^*_{\frac{M}{2}+1-j} + i\, z^*_{\frac{M}{2}+1-j} \qquad 5.1$$

where
$$y^*_{\frac{M}{2}+1-j} = \tfrac{1}{2}\left\{\frac{\pi}{M} + \tfrac{1}{2}\left[\sin\frac{2\pi}{M}j - \sin\frac{2\pi}{M}(j-1)\right]\right\} / \Gamma^*_{\frac{M}{2}+1-j}$$

$$z^*_{\frac{M}{2}+1-j} = \tfrac{1}{2}\left\{\sin\frac{\pi}{M}j + \sin\frac{\pi}{M}(j-1)\right\}$$

and the point vortex strength is given by

$$\Gamma^*_{\frac{M}{2}+1-j} = \Gamma_{\frac{M}{2}+1-j}/\Gamma_o = \sin\frac{\pi}{M}j - \sin\frac{\pi}{M}(j-1) \qquad 5.2$$

$$j = 1, \ldots, \frac{M}{2} \text{ and } M \geq 2 \quad .$$

(Note that for large M the point vortices are equispaced.)

The above distribution gives the positions of the point vortices in the upper positive quadrant (i.e., $y > 0$, $z > 0$). In the lower quadrant (i.e., $y > 0$, $z < 0$) the positions of the vortices are simply the complex conjugate $\overline{Z}$. Thus

$$Z_{\frac{M}{2}+j}(0) = \overline{Z}_{\frac{M}{2}+1-j}(0)$$

and
$$\Gamma^*_{\frac{M}{2}+j} = \Gamma^*_{\frac{M}{2}+1-j} \quad .$$

The symmetry of the sheet was employed to save computation time.

[†] It was found convenient to carry out the computations in the complex plane.

With the above initial conditions, the system of equations (Section II, Eq. 2. 9) was integrated forward in time using a fourth-order Runge-Kutta integrating scheme with $dt^* = 0.0025$. Double precision arithmetic, giving a sixteen figure accuracy of the basic arithmetic operations, was employed on the IBM 375-158 computer. The results of the calculation for $M = 40$ (point vortices per half wing) and a cut-off radius, $r_c^* = 0.1$ are displayed on Figures 19a through 19h. These figures show the positions[†] of the point vortices in the time interval $0 \leq t^* \leq 1.0$. The spline interpolation scheme was used to draw a smooth curve through the point vortices to indicate the trace of the vortex sheet in the y-z plane. The interpolation, of course, failed in the inner portion of the spiral where there are few vortices per unit length of the sheet. Where possible, the curve was drawn in by hand.

The figures show a distortion of the vortex sheet followed by a smooth roll-up into a pair of doubly branched spirals. Randomization effect of point vortices within the spiral is realized, however, after $t^* = 0.6$. After this time the spiral takes on an elliptic shape.

Although the figures are quite self-descriptive, some interesting features of the roll-up process are not obvious and will therefore be discussed.

Initially, the cylindrical vortex sheet (represented by point

---

[†] Two 'dummy' vortices of zero strength were used to locate the vortex sheet in the plane of symmetry. They are not included in numbering the point vortices.

vortices in Figure 19) undergoes distortion from its initial circular shape. During the distortion phase the upper half of the vortex sheet contracts in length while the lower half of the sheet stretches, as evidenced by the point vortex spacings. (Initially the point vortices were approximately equispaced.) The effect of the stretching and contraction of the sheet is redistribution of vorticity on the sheet.

In the initial state of the vortex sheet, vorticity is maximum at $\varphi = \pm \pi/2$ (φ measured from the bottom of the median plane of symmetry). During the distortion phase of the roll-up process, the point of maximum vorticity moves from its initial position on the sheet to a point which originates from an intermediate value of $\varphi = \pi/2$ and $\varphi = \pi$ on the initial cylindrical vortex sheet. The origin of maximum vorticity thus varies in time. At some final value, φ_0, distortion ends, and the sheet begins to roll up about the point of maximum vorticity into a pair of doubly branched spirals. The centers of the spirals thus originated from points, $\pm\varphi_0$, on the upper quadrants of the ring wing, between $\varphi = \pi/2$ and $\varphi = \pi$.

The value of φ_0 is obtained from the numerical results and corresponds to the initial position of vortex number 12. The value of φ_0 is approximately 128°. (The position of vortex number 12 is shown by an arrow on Figure 19.) It is interesting to note that the origins of roll-up approximately correspond to the initial centroids of vorticity shed from the upper quadrants of the ring wing. An analytical verification of this fact, if possible, may be worthwhile.

The roll-up process of the ring wing generated vortex sheet is different from, say, the roll-up process of the vortex sheet behind an elliptic wing. In this latter case, the initially induced velocity normal to the sheet is uniform. Therefore, the vortex sheet immediately rolls up about the edges of the sheet without initially distorting in shape. The origin of roll-up corresponds to a mathematical singularity in the vorticity distribution. The singularity originates from the tip of the wing, where vorticity shed is theoretically infinite. On the other hand, the vortex sheet shed by a ring wing contains no singularity. The strength of the vortex sheet is $2W_o \cos\varphi$.[†] The sheet is actually a shell and, therefore, has no free edges about which to roll up. At the outset, one may suppose the sheet to roll up about the initial points of maximum vorticity ($\varphi = \pm \pi/2$). However, as discussed earlier, this is not the case. Distortion of the sheet, due to nonuniform induced velocities on the sheet, causes the position of the maximum vorticity to shift.

The mean initial radially induced velocity distribution on the cylindrical sheet is $W_o \cos\varphi$ and the mean tangential velocity is zero everywhere on the sheet. The lower half of the sheet thus initially experiences positive (i. e., outward) radial velocities resulting in stretching of the vortex sheet; whereas, the upper half

---

[†] W_o is the initially induced downwash velocity within the cylindrical vortex sheet. It is equal to Γ_o/D, where Γ_o is the root circulation and D is wing diameter.

of the sheet, on the other hand, experiences negative (i. e., inward) radial velocities that result in contraction of the upper portion of the vortex sheet. Thus, the net effect of the nonuniform radial velocities is distortion of the sheet.

The center of gravity of the vortex system initially accelerates downward during the distortion phase, to a uniform downward velocity as the sheet rolls up. After complete roll-up, the separation of the trailing vortices is $\frac{\pi}{4}D$, and their speed of descent is $(4/\pi^2)\ W_o$. This change in velocity is twice as large as that change experienced in the case of an elliptic wing. Figure 7 shows the result from the numerical calculation. The maximum downwash in the plane of symmetry increases from the initial value of W_o to $(16/\pi^2)\ W_o$ after complete roll-up. In contrast, for the elliptic wing case, the maximum downwash in the plane of symmetry decreases from W_o to $(8/\pi^2)\ W_o$ (where $W_o = \Gamma_o/b$, for a wing span of b). These fundamental features of the ring wing are borne out by experimental results (Section Vb). It may be noted here, however, that due to departure of the shape of the trailing vortices from circular to elliptic, the theoretical velocity values are not fully realized.

The point vortex approximation and the introduction of a cutoff radius have the effect of reducing the initial induced radial velocities and of introducing small tangential velocities. The effect of these errors is to slightly slow down the rate of roll-up. (This effect will be discussed further when the rate of roll-up is estimated.) The magnitude of the slowdown effect is not calculated but the relative effects on roll-up, due to the cut-off radii, can be seen on Figures 19a, b, and c. The influence of the cut-off radius is localized, and induced velocities of distant portions of the sheet are not affected. The evolution of the vortex sheet for different cut-off radii, thus differ where vorticity concentrates.

As anticipated, the cut-off radius effectively prevents early randomization of the point vortices. The times, t_r^*, after which chaotic motion of the vortices sets in, initial changes in radial velocity, Δu_r, and tangential velocities, Δu_θ, are shown in Table 1, for different cut-off radii r_c^*.

TABLE 1

r_c^*	$\frac{\Delta u_r}{W_o}$	$\frac{\Delta u_\theta}{W_o}$	t_r^*
0	0.016	-0.012	0.16
0.05	0.029	-0.015	0.35
0.10	0.056	-0.028	0.6

Figure 20b shows the beginning of chaotic motion for the case of $r_c^* = 0.05$. It may be noted here that, for the times considered, chaotic motion is confined to vortices within the region of vorticity concentration and does not affect distant portions of the sheet. However, such spurious motions of the vortices might eventually spread outward to disrupt other vortices.

A different kind of failure is noted in the case without a cut-off radius. In this case an instability sets in as early as $t^* = 0.16$, before the sheet even gets a chance to roll up. This unphysical feature of the sheet, unlike randomization of the vortices, quickly propagates outward to affect other point vortices. The point vortices tend to pair up as they are drawn toward the region of vorticity concentration where chaotic motion then sets in. Figure 21 displays the instability of the point-vortex representation of the vortex sheet. The instability occurs on the sheet where vorticity is maximum in agreement with Saffman's prediction (Ref. 4).

The instability and randomization features of the sheet approximation by point vortices were anticipated before hand. Such anticipation led to introducing the cut-off radius in the first place. However, since these are most probably the first calculations on a ring wing generated vortex sheet, it was worthwhile to perform the calculations without a cut-off radius. Furthermore, the results confirm the fact that the randomization of point vortices is encountered even in the case of vortex sheets which are free of singularities. In the case of the vortex sheet roll-up behind an elliptic wing, chaotic motion of vortices sets in quickly if no method for smooth roll-up is employed. However, as the results presented here show, it is possible to study at least the distortion phase of the sheet behind a ring wing without any scheme for smoothing effect. For the purpose of this study, the numerical calculations were performed to obtain some insight into the sheet vortex roll-up behind a ring wing. Introduction of the cut-off radius seems to satisfactorily meet that objective. The subject of instabilities will not, therefore, be discussed any further. Discussions of it may be found in References 4 and 7.

No estimate of errors introduced by the cut-off radius was made. However, calculations of the point vortex motion invariants indicate that such errors might not be serious. These invariants were calculated from the dimensionless expressions below for $M = 40$.

$$\frac{1}{2} \sum_{i=1}^{M} \Gamma_i^* y_i^* \qquad 5.3a$$

$$- \frac{1}{4\pi} \sum_{i \neq j}^{2M} \sum \Gamma_i^* \Gamma_j^* \log |Z_i - Z_j| \qquad 5.3b$$

The first invariant is the 'vertical impulse' divided by the net vorticity per half wing to obtain y_o^*, the lateral position of vorticity centroid. The initial value of y_o^* is $\pi/4$. The lateral position of vorticity centroid remained constant for all times considered, even during chaotic motions; different cut-off radii did not affect it either. The 'energy' invariant, the second expression listed above, was also preserved. For all conditions considered, the energy invariant varied in the third decimal place by 0.007 at worst. The preservation of the invariants lends confidence to the accuracy of the computations.

A further check on the calculation was made by computing W_g^*, the nondimensional descent speed of the vortex center of gravity (Fig. 7), and the computed value was found to be 1.50. If the vortices are considered to be completely rolled up and circular, the theoretical value of W_g^* is $\pi/2 \simeq 1.57$. The velocity field at different times, due to the point vortices, was also calculated and was found to be in fair agreement with experimental results presented later in this section.

Figure 5a shows the trajectories of some particular point vortices for $r_c^* = 0.1$. The path of vortex number 12 is of most interest since it marks the position of the spiral center. The sudden kink in the path corresponds to the onset of spurious fluctuations within the rolled-up spiral. This occured at $t^* = 0.6$ and prevented the center of the spiral from reaching the eventual lateral position, $\pi/4$. Figure 5b shows this approach toward the lateral position more clearly. The path is initially smooth until fluctuations set in. In reality, since the vortex sheet does not completely roll up, the center of the spiral approaches $y^* = \pi/4$ asymptotically. On the same Figure 5b, a dashed line is drawn to indicate roughly the mean path of vortex number 12. Note that the dashed line cuts $y^* = \pi/4$ at about $t^* = 1.06$. This time is roughly that predicted (Section II) for the roll up to be considered essentially complete. To recall, the time of complete roll-up, $t_c^* \simeq 1.0$ was estimated by assuming that it is equivalent to half the orbital period for $M = 2$ (Fig. 6) point vortex representation of the sheet.

An attempt was made to verify the estimated results obtained in Appendix B. These results, referring to the inner portion of the spiral, are summarized below in the present notation. The contraction factor $\lambda = 2$ is used. The circulation distribution around a circle with radius r^* centered with the spiral is given by

$$\frac{\Gamma}{\Gamma_o} = \frac{\pi}{2} \sin 2 r^* \qquad 5.4$$

The polar equation of the inner portion of the spiral is

$$r_i^* = \frac{\pi^3}{8} \frac{t^* - t_o^*}{\theta - \theta_\infty} \qquad 5.5$$

for the 'inner' spiral[†], and for the 'outer' spiral the polar equation is given by

$$r_o^* = \frac{\pi^3}{8} \frac{t^* - t_o^*}{\theta + \pi - \theta_\infty} \qquad 5.6$$

where t_o^* is the time the sheet begins to roll up, and θ_∞ is an arbitrary constant of integration. The radius of the inner portion of the spiral is

$$a_s^* = A_s \, (t^* - t_o^*) \qquad 5.7$$

where A_s is an undetermined constant. From Equations 5.4 and 5.7, the rate of roll-up is obtained as

$$f = \frac{\Gamma}{2\Gamma_o} = \frac{\pi}{4} \sin 2 A_s \, (t^* - t_o^*) \qquad 5.8$$

The rolled-up portion of the sheet is arbitrarily defined to be the portion between the points where a horizontal line through the center of the spiral (taken to be vortex number 12) last cuts the inner and outer spirals. The diameter of the spiral was taken to be the separation of the two points, and a circle with radius equaling half

---

[†] The 'inner' spiral refers to the branch of the spiral consisting of sheet lying to the left of roll-up origin φ_o (i. e., the segment lying in $\varphi_o \leq \varphi \leq \pi$, where $\cos\varphi_o = -\pi/4$). The tail end of the inner spiral is the upper point where the sheet cuts the plane of symmetry. The other branch of the spiral is referred to as the 'outer' spiral.

this distance was then drawn, centered on the spiral. For times less than $t^* = 0.6$, the spiral was found to be quite symmetric on lines through the center, and the above definition of spiral radius held quite well. The definition was not so good after chaotic motion set in and ellipticity of the spiral shape began, due to mutual interaction of the two spirals. The best possible circles were then drawn, and the mean radius was taken. The worst case was at $t^* = 1.0$, the largest time considered, and even here the spread in radii of the spiral from the mean was only $\pm 0.03R$.

The circulation about the drawn circle was then obtained by noting the vortices within the circle and their strengths. For point vortices found near the circle, their strength within the circle was obtained proportionately, according to the ratio of the segment within the circle to the length of the sheet segment the vortex represents. This length of the sheet was taken to be halfway between the particular point vortex and its neighbors on the sheet. In other words, the segment of the sheet was assumed to be equally divided between neighboring point vortices near the circle. The fractional strength of the vortex, included in the circle, was thus taken to be the ratio of the sheet within the circle to the total length of sheet segment that the point vortex represents. If a point vortex was found exactly on the circle half its strength was taken since initially the point vortices were approximately equispaced.

The radius of the spiral is plotted on Figure 8, as a_s/D, where D is the diameter of the ring wing, ($a_s^* = 2a_s/D$), and is found to be fairly linear, thus confirming the prediction (Eq. 5.7). The slope of a straight line through points at $t^* < .6$ is found to be roughly $\pi/8$, giving $A_s \simeq \pi/4$. Extrapolating the line back to cut the time axis, t_o^* is obtained to be roughly 0.13.

The fraction of rolled-up vorticity, f, is also plotted on Figure 8. Note that for a cut-off radius of 0.1 the value of f and a_s/D are less than the values corresponding to $r_c^* = 0.05$ for times less than 0.4. This indicates that the cut-off radius retards the roll-up rate. Thus, for small times, $r_c^* = 0.05$ is more representative than $r_c^* = 0.1$.

Using $A_s = \pi/4$ and t_o^* 0.13, Equation 5.8 is compared to the numerical data on Figure 8. The agreement is fairly reasonable for $t^* < 0.6$. It is worth noting that due to the point vortex approximation, f already has an initial value of 0.03 due to vortex number 12 (center of spiral). The agreement between prediction and numerical data becomes better if 0.03 is subtracted from the data. At $t^* > .6$ the induced velocity field from the other spiral is felt and the two mutually interact, tending to make the spiral more elliptic than circular. It may be recalled here that the basic assumption in obtaining Equations 5.4 through 5.8 was that one has an isolated circular vortex. This assumption is only true in the early stages of roll-up and in the inner portion of the spiral. The assumption of circular inner portions of the spiral holds better here than in the case of an elliptic wing, because of the double branch feature in the spiral formed behind a ring wing.

As seen in Figure 8, the rate of roll-up in the case of the ring wing is very slow, as compared to the case of an elliptic wing. Numerical data from Reference 7 are compared to the present study. (The time scale from this reference has been reduced to the time scale of this study.) For example, about 90 percent of the vorticity is rolled-up behind the elliptic wing at $t^* = 0.51$, in contrast to about 25 percent in the case of the ring wing.

The large difference in the roll-up rate of the two wings is explainable. Vorticity is distributed over a wide surface area on the ring wing ($\omega(\varphi) = 2W_o \sin\varphi$), whereas the elliptic wing has vorticity which is concentrated near the wing tip and is given by

$$\omega(y) \simeq 2W_o \, (y/b)^{-\frac{1}{2}} \quad . \qquad 5.9$$

Here y is measured from the wing tip, W_o is the initially induced velocity on the sheet and b is the wing span. Thus roll-up is very rapid in the latter case. In fact, from Reference 7, 50 percent of the vorticity is rolled up at $t^* = 0.02$.

The slow roll-up behind the wing justifies the provisional assumption of light loading approximation, and thus the replacement of the three-dimensional steady flow by a two-dimensional unsteady flow is reasonable.

Figure 9 compares Equation 5.4, the circulation distribution about the inner portion of the spiral, to numerical data. Again the agreement is reasonably fair, and is almost excellent if 0.06 (the initial vorticity concentration of point vortex number 12) is subtracted from the data.

Finally, the polar Equations 5.5 and 5.6 are compared to numerical results. The derivations that led to the polar equation of the spiral (Appendix B) do not determine the constants t_o^* and θ_∞; the coordinates of the spiral center were not determined either. The time roll-up begins, t_o^* is taken to be ~ 0.13 as determined earlier from the numerical data. The integrating constant, θ_∞, is also determined from the numerical results. This is done by equating Equation 5.5 to Equation 5.7, the radius of the spiral; the polar angle, θ, is arbitrarily chosen to be 2π at the radius[†] of the 'inner' spiral. Using these constants, t_o^* and θ_∞, the spiral was plotted and centered on vortex number 12. The results are presented on Figure 4 for the times indicated. (Only the spiral to the right of the median plane of symmetry is shown; its reflection in the plane of symmetry is the other spiral.) The agreement obtained is found to be quite satisfactory, except for the point vortices in the innermost portion of the spiral, i.e., in the immediate neighborhood of the spiral center (vortex number 12). The disagreement here is expected. As the vortex sheet rolls up into a spiral, the sheet continuously stretches (evidenced by the separation of the point vortices) to make more and more turns as the center is approached. Theoretically the central portion of the spiral (as $\theta \to \infty$) consists of an infinite number of turns. One cannot, therefore, represent the

---

[†] The numerical spiral radius was arbitrarily defined as the horizontal line from the spiral center to the last turn of the 'inner' spiral.

central portion with a finite number of point vortices. Thus, the point vortex approximation breaks down in the central portion of the spiral.

For $r_c^* = 0.05$, at $t^* = 0.30$, point vortex number 8 deviates from the spiral sheet. Examination of the numerical data showed that the velocity vector of vortex #8 is as shown by the arrow on Figure 4. This point vortex may therefore be ignored. The second spiral on the same figure corresponds to $r_c^* = 0.10$ at $t^* = 0.40$. The slow down effect on roll-up, due to the cut-off radius, can be seen by comparing the inner portion of the spiral to that of $r_c^* = 0.05$ at $t^* = 0.30$. The numerical results show that the latter, at $t^* = 0.30$, has made more turns than the former at a later time $t^* = 0.40$.

At $t^* = 0.55$, the last turn of the 'outer' spiral distorts from its theoretical shape. This is due to interaction from the spiral on the left side of the plane of symmetry (not shown in the figure). Mutual interaction of the two vortices formed by the rolled-up spirals was ignored in the derivations of the spiral's polar equations. The agreement obtained here ($t^* = 0.55$, $r_c^* = 0.10$) is still very good.

It may be noted that for all three cases of the spiral shape the same constants of t_o^* and θ_∞ were used. The agreement obtained here verifies Saffman and Moore's result (Ref. 5) for the case $n = 0$ (see Appendix B of this study). The similarity of the spiral in time, referred to by Kaden (Ref. 1) as proportional expansion of the spiral, is also demonstrated.

V.2 Experiment

As described in Section IV, LDV measurements included axial and vertical velocity profiles in the vortex wake behind a ring wing model of aspect ratio, A = 2. At least two traverses were made at each downstream station x; one vertical traverse in the median plane of symmetry, z axis, and one horizontal traverse, y axis. Flow visualization techniques, using dye and hydrogen bubbles, were employed to study the vortex formation. Unfortunately no presentable pictures were obtained. However, flow visualizations and velocity measurements substantiated the main numerical result, that the vortex sheet generated by a ring wing rolls up into a pair of trailing vortices. The experimental study suggested two main regions of the vortex wake: a) roll-up of the vortex sheet, and b) decay of the trailing vortices thus formed by the roll-up. Results and discussion pertaining to these two regions will be presented here in that order.

V.2.1 Roll-up of the Vortex Sheet

An attempt was made to verify the origin of roll-up on the wing as suggested by the numerical results. The result was that the vortex center originated from a point on the ring wing, defined by $\theta = 38^{\circ}$, where θ is measured upward from the horizontal diameter of the wing. Test of this result consisted of injecting dye on the periphery of the wing. The only position of dye injection where a discernible vortex core could be observed was in the neighborhood of $\theta = 45^{\circ}$ on the wing. In other positions of dye injection, the dye simply diffused over a large area of the vortex sheet. Dye injected at the center of the model, for example, was entrained by both vortices trailing downstream. The cross flow (Fig. 2) on the surface of the wing was observed. The vortex sheet was observed to roll up into a pair of vortices at about 10 - 15 diameters downstream from the trailing edge.

LDV traverses were made in the roll-up regions of the wake to locate the position of the wake in the y-z plane. The results are shown in Figure 22, for $\alpha = 10^{o}$ at 2.5 and 5 wing diameters downstream. The numerical results are shown in the same figure for comparison. There is a clear indication of distortion and roll-up of the vortex sheet[†] which, in practice, is the wake.

Figure 26 presents vertical velocity profiles in the wake at a downstream station $x/D = 0.2$. This was the closest station to the trailing edge that was traversable. The profiles consist of data from $\alpha^{o} = 4, 7, 10$ and 12 degrees as indicated and other plots which will soon be explained. On-diameter horizontal traverse, giving the upwash and downwash, is shown on the right. The plot on the left shows the downwash in the plane of symmetry. The ring wing's trailing edge is shown as a circle. The non-dimensional vertical velocity $w/\alpha^{o}U$ is plotted as a function of

---

[†] In reality viscosity is responsible for generating vorticity in the sheet which the wake approaches for vanishingly small viscosity in the mathematical sense.

y/R and z/R respectively, for horizontal and vertical velocity profiles. The angle of attack α^o is in degrees; U is the free-stream velocity (or wing speed) and R is the wing radius. The data shown here were taken at $U = 33$ cm/sec, corresponding to a Reynolds number $R_D = 27{,}000$.

The plot marked 'A' corresponds to the potential flow field of an infinite cylindrical vortex sheet of strength $\omega(\varphi) = (\Gamma_o/D)\sin\varphi$. Here D is the ring wing diameter, Γ_o is the root circulation about the wing, and φ is the polar angle measured from the bottom of the median plane of symmetry, i.e., $y = 0$. The downwash inside the cylindrical sheet is $W_o = \Gamma_o/D$, and the vertical velocity field outside the cylinder is given by

$$w = W_o R^2 \frac{y^2 - z^2}{(z^2 + y^2)^2} \quad , \quad \sqrt{z^2 + y^2} > R \qquad 5.10$$

(Note that the flow field is equivalent to the potential flow about a cylinder with radius R and speed W_o.)

From Prandtl's lifting line considerations,

$$\frac{W_o}{\alpha^o U} = \frac{\Gamma_o}{\alpha^o UD} = \frac{\pi^2}{90\,(A + \pi/2)} \qquad 5.11$$

where $A = D/C$, the wing diameter to chord ratio, is the aspect ratio. For $A = 2$, the aspect ratio of the wing model tested, $W_o/\alpha_o U = 0.01535$. This value was used to plot 'A' on Figure 26. Plot 'A' also includes the numerical calculation by point vortex approximation described earlier, using a cut-off radius of zero and 0.1. Deviations from the analytic solution are seen to be restricted to points near the sheet, with the severest change occurring in the maximum upwash.

As noted earlier in Section II, the two-dimensional approximation is not expected to hold in close proximity to the wing. The downwash at a lifting line, for example, is only half the two-dimensional value at infinity, or the Trefftz plane. (For rectangular or elliptic wings, most of the deviations from calculations using the Biot-Savart law and taking into account the bound vortices on the wing occur over about a wing-span distance downstream.) Furthermore, vorticity is not quite transferred downstream at the free stream velocity. As demonstrated earlier (Section V. 1) during roll-up of the vortex sheet the vortex lines undergo stretching and bending in addition to lateral displacements, thus changing vorticity. However, the numerical results on the ring wing (Section V. 1) demonstrated that roll-up of the sheet vortex is delayed far downstream and should not, therefore, incur serious errors in the flow field near the wing. It is demonstrated below that the Trefftz plane is not far removed from the ring wing, at least for the case of the aspect ratio of 2 considered.

The plot marked 'B' on Figure 26 was obtained from an inviscid three-dimensional calculation by Weissinger (Ref. 21). Using the Biot-Savart law he calculated the flow field about the ring wing represented by a distribution of vortex rings and their trailing vorticity cylinder. For a thin cylindrical ring wing, $\Omega\ (\xi,\varphi)$, the vorticity density on the wing surface is represented by

$$\Omega\ (\xi,\varphi) = Ug_1\ (\xi)\ \cos\varphi \qquad 5.12$$

where $g_1(\xi)$ is represented by Birnbaum series,

$$g_1(\xi) = B_{o1}\ \mathrm{ctg}\ \frac{\Theta}{2} + \sum_{j=1}^{\infty} B_{j1}\ \sin j\Theta \qquad 5.13$$

where

$$\xi = \frac{2X}{C} = -\ \cos\Theta,\ \ -1 < \xi < 1$$

and X is the axial distance measured from the center of the wing with chord C. (Note that the Kutta condition at the trailing edge, $\Omega\ (1,\varphi) = 0$, is satisfied.) The calculations are lengthy and laborious and are performed for each individual wing aspect ratio, A. A summary of the calculations to obtain B_{j1}[†] may be found in Reference 28. Fortunately the Birnbaum coefficients were available for A = 2 (Refs. 23 or 30), the wing aspect ratio employed in this study, thus making it possible to compare the experimental data to Weissinger's calculations. Reference 21 contains tables for the flow field about the ring wing for the case of a single bound ring vortex with circulation distribution $\Gamma = \Gamma_o \cos\varphi$. This is appropriate for large aspect ratios. For small aspect ratios, the wing is represented by a continuous distribution of ring vortices (Eq. 5.12), and the induced velocities are obtained by integration from the induced velocities of the single ring vortex model.

[†] For A = 2, $B^{(0)}_{01} = 1.098$, $B^{(0)}_{11} = -0.238$, $B^{(0)}_{21} = -0.018$, $B^{(0)}_{31} = 0.002$ and $B^{(0)}_{j1} = 0$ for $j > 3$, for a unit angle of attack, α in radians.

In most cases the single vortex model is sufficient as found here for A = 2.

Plot 'B' on Figure 26 comprises the two cases of a single bound ring vortex and one hundred ring vortices distributed according to Equation 5.12. A similar approach of the point vortex approximation was used. (One may refer to this in a similar manner as the ring vortex approximation.) The wing surface was divided into 100 ring segments and each segment was represented by a single ring vortex, with strength equal to the net vorticity in the segment. The ring vortex was then placed at the centroid of vorticity of the segment. The induced velocities were then obtained by summing over the induced velocities from each of the 100 vortex rings and their trailing vortex cylinders. The velocity field, thus obtained at the downstream station x/D = 0.2, is seen on Figure 26 to hardly differ from the velocity field of the single ring vortex model.

The single ring vortex with circulation $\Gamma = \Gamma_o \cos \varphi$ was placed at the aerodynamic center, X_{ac}, of the ring wing, given by (Ref. 24)

$$\frac{X_{ac}}{C} = -\frac{1}{8}\,\frac{2\,B^{(0)}_{01} + B^{(0)}_{21}}{B^{(0)}_{01} + \frac{1}{2}\,B^{(0)}_{11}} \qquad 5.14$$

and the root circulation Γ_o is obtained by integrating Equation 5.12 over the wing surface

$$\Gamma_o = \tfrac{1}{2}\, UC \int_{-1}^{1} g_1\,(\xi)\, d\xi$$
$$= \frac{\pi}{2}\, UC \left(B^{(0)}{}_{01} + \tfrac{1}{2}\, B^{(0)}{}_{11} \right) \alpha \qquad 5.15$$

For the aspect ratio $A = 2$, $X_{ac} = -0.278C$ (0.222 chords from the leading edge) which is roughly the quarter chord point, the aerodynamic center for $A \to \infty$. The root circulation is given by

$$\frac{\Gamma_o}{UD} = \frac{W_o}{U} = 0.01342\,\alpha^{o}\ , \qquad 5.16$$

where the axial angle of attack α^o is in degrees. (It is worth noting that the wing lift coefficient is $C_L = \Gamma_o/UC = 0.02684\,\alpha^o$ for $A = 2$. Lifting line approximations give $C_L = 0.03071\,\alpha^o$ and $W_o/U = 0.01535\,\alpha^o$ for $A = 2$.) It is seen in Figure 26 that Weissinger's calculations are in fair agreement with the experimental results. It will now be demonstrated that the two-dimensional inviscid flow field is a fair approximation.

An examination of the two-dimensional flow field (Plot 'A', Fig. 26) shows that if one uses the net lift on the wing predicted by Weissinger's calculation, instead of that obtained by the lifting line theory, the two-dimensional flow field agrees fairly well with the three-dimensional calculations by Weissenger (Plot 'B'). Although the results obtained above are for a wing aspect ratio of 2, the two-dimensional calculation is a fair approximation for other aspect ratios. This deduction is based on the fact that the aerodynamic center, where the lifting line may be most appropriately placed, lies between the leading edge and the mid-chord point for all aspect ratios of the cylindrical ring wing. Thus the trailing edge is at least 3/4 chords from the lifting line. The above stated results of the flow field indicate that the Trefftz plane is quite close to the trailing edge of the ring wing, within roughly one wing radius downstream.

It may be pointed out, however, that some features of the flow field are missed by the two-dimensional calculations. Firstly, the downwash within the cylindrical sheet is not exactly constant; the downwash rises slightly from the center toward the cylindrical sheet vortex. Secondly, the peak upwash is less than the maximum downwash; at the downstream station $x/D = 0.2$, the maximum upwash is about 91% of the downwash in the center of the cylindrical sheet vortex. Thirdly, induced axial velocities are not realized by the two-dimensional approximation.

The features mentioned above are reasonably substantiated by the experimental data. The agreement with Weissinger's results is fair. The lower experimental values may be due to viscous effects, in view of the low Reynolds number, ($R_D = 27,000$). As plotted, the experimental data display a significant amount of scatter, although for each angle of attack the velocity profiles have very little scatter (see, for example, Figure 24a). The low angle of attack (4^o) seems to deviate the most from the general trend. This is because of errors involved in measuring the low velocities associated with low angles of attack and further normalizing the measured velocity by the angle of attack.

Figures 25a through 25h display velocity profiles obtained by vertical traverses in the play of symmetry at different downstream stations. In these profiles, the positions of the axial velocity defect mark the locations of the vortex sheet in the plane of symmetry. Horizontal traverses were made through the position of maximum downwash to obtain tangential and axial velocities in the vortex core. There is, of course, no well-defined vortex core during the distortion phase, and one cannot, therefore, speak of tangential velocities in the core. In such a situation the velocities measured are simply referred to as vertical velocities. Figures 24a through 24h present velocity profiles obtained by horizontal traverses. Only proviles at 12° angle of attack and $U = 33$ cm/sec are presented here; they are typical of the flow field in the vortex wake.

Figures 24a-h and 25a-h clearly show the variations in the flow field as the vortex sheet distorts and rolls up. The measured flow field in the roll-up regions show a striking resemblance to the numerically calculated flow field in the vortex wake (Figs. 23a through 23e). The steps in the horizontal traverse profiles are due to the vortex core and the unrolled portion of the vortex sheet. On Figure 27, the measured maximum downwash velocities, w_o, are compared to the numerical results.

In view of the light loading approximation $t = x/U$ and the nondimensional time scale of the numerical calculation, t^* is related to the downstream station by

$$\frac{x}{D} = \frac{\pi^3}{16}\frac{A}{C_L}t^* \qquad 5.17$$

where $t^* = 0$ is taken to correspond to the trailing edge, and the dimensionless velocity w^* is related to the vertical velocity w by

$$\frac{w}{U} = \frac{8}{\pi^3}\frac{C_L}{A}w^* \quad . \qquad 5.18$$

In view of the above relationships it was found convenient to plot $(w_o/\alpha_o U)(A/C_{L_\alpha o})$ against $(\alpha^o x/D)(C_{L_\alpha o}A^{-1})$. The slope of the lift curve $C_{L_\alpha o}$, was obtained from Weissinger's calculations (Refs. 21,23) as described earlier. For $A = 2$, $A^{-1}C_{L_\alpha o} = 0.01342$. This value of $C_{L_\alpha o}$ will be used in future comparisons of experimental data to theory.

The initial downwash within the cylindrical vortex sheet before roll-up, W_o, is also shown on Figure 27. In the non-dimensionalized form the two-dimensional downwash is equal to one. It may be recalled that if the vortex sheet is assumed to completely roll up into a pair of vortex filaments, the separation of the pair is $(\pi/4)D$, and the maximum induced downwash is $(16/\pi^2)W_o$; this gives a value of roughly 1.6 in the dimensionless form plotted.

The experimental data are seen to fall between the two dimensional values of downwash, except for the data at $x/D = 0.2$ (the nearest data to the trailing edge, $x/D = 0$), which are a little lower than W_o. The data also seem to follow the general trend of the numerical data which show some decay downstream; this apparent decay is due to two main causes. Firstly, during roll-up the vortex centers move apart laterally, thus decreasing the induced velocities in the plane of symmetry. Secondly, the mutual interaction of the pair of trailing vortices tend to distort the shape of the vortex from circular to an elliptic shape, thus changing vorticity and the induced velocities. In the case of the experimental data, decay is further caused by viscous effects. The roll-up process is not entirely independent of viscosity, but it is simultaneously accompanied by viscous diffusion.

Figure 27 also shows the results from Weissinger's three-dimensional inviscid calculations for a single ring vortex model (Ref. 23). The maximum downwash on the axis of the cylindrical vortex sheet, in nondimensional form, is given by

$$\frac{w_o}{\alpha^0 U}\,\frac{A}{C_{L_\alpha o}} = -\tfrac{1}{2}\left[1 + g(x^*_o)\right] \qquad 5.19$$

where $$g(x^*_o) = \frac{x^*_o}{(1+x^{*2}_o)^{\frac{1}{2}}}\left[1 + \frac{1}{1+x^{*2}_o}\right]$$

and $$x_o^* = x_o/R$$

and x_o is measured from the center of the ring vortex. (In this comparison the ring vortex was placed at the aerodynamic center of the ring wing). The three-dimensional results are seen to differ very little from the two-dimensional results (the maximum deviation is 0.04 W_o), again indicating the closeness of the Trefftz plane to the trailing edge.

Figure 28 shows the position of the vortex core in all three axes. The vertical position of the vortex center was taken to be the position of maximum downwash in the plane of symmetry, since the maximum downwash occurs midway between regions of vorticity concentration, i.e., the vortex cores. The vortex core is seen to accelerate to approximately a uniform speed of descent after roll-up of the sheet vortex is complete.

Now, if the vortex sheet were to completely roll up into a pair of circular vortices, the net vorticity in each vortex will be $2\Gamma_o$ and their separation distance will be $\pi D/4$. The speed of descent of the vortex pair is then given by

$$W_g = \frac{4}{\pi^2} \cdot \frac{\Gamma_o}{D} = \frac{4}{\pi^2} \cdot W_o \qquad 5.20$$

and the vertical position, $z_o = W_g t$ (upon replacing the time t, by x/U) is given by

$$\frac{z_o}{D} = \frac{4}{\pi^2} \frac{C_{L_\alpha o}}{A} \left(\alpha^o \frac{x}{D}\right) \qquad 5.21$$

where Γ_o/UD has been replaced by C_L/A. Equation 5.21 is compared to the experimental result (Fig. 28), using $C_{L_\alpha o}/A$ = 0.01342 as previously calculated for the wing aspect ratio of 2, and the numerical result is also shown for comparison. The experimental value of the vortex descent speed is lower than that predicted by Equation 5.21 above. Assuming that the ring wing has the net lift predicted by theory, and since channel wall effects were noted to be negligible (in the cause of the experiments), then the vortex low speed of descent may be attributed to three main causes.

The first cause is distortion of the vortices from their circular shapes through their mutual interaction, as demonstrated by the numerical results (Section V. 1); this is seen to be true by the nonsymmetric nature of the velocity profiles (Fig. 24e). Secondly, vorticity of opposite sign could annul each other at the median plane of symmetry and thus decrease the strength of the vortices, reducing their speed of descent. Thirdly, in view of the low Reynolds number at which the experiments were conducted, there could be a loss of energy (and thus loss of vorticity) through viscous effects; this is evident from the data plotted on Figure 28.

It is possible to estimate the strength of the vortex by Equation 5. 21. From Figure 28, the slope of the dashed line through the data point is roughly 4.24×10^{-3} (this line is weighted toward the higher angles of attack of 12 and 10 degrees, and higher Reynolds number of 2.7×10^{4}). Equating the slope to the derivative of Equation 5. 21, one obtains the strength of the vortex in dimensionless form as

$$\frac{\Gamma_v}{\alpha^o UD} = 2 \frac{\pi^2}{4} (4.24 \times 10^{-3}) \simeq 0.021 \; ; \qquad 5.22$$

a reduction of about 20% from the expected value (i. e., net vorticity generated per half wing) which is given by

$$2 \frac{\Gamma_o}{\alpha^o UD} = 2 \; (0.01342) = 0.0268 \, . \qquad 5.23$$

It is interesting to note here that the maximum net vorticity predicted to be rolled up into the vortex core (Eq. B2, Appendix B) is given by

$$\frac{\pi}{2} \frac{\Gamma_o}{\alpha^o UD} \cong 0.021 \quad . \qquad 5.24$$

If this is correct, it would seem that the vorticity contained in the unrolled portion of the sheet has been annihilated by viscosity. However, the above stated fact is debatable due to the uncertainty in the contraction factor, λ, and other assumptions. The lateral position of the vortex core was taken to be the position of maximum vorticity (i. e., maximum slope), as shown on Figure 29, for it is at this position that the vorticity, due to the vortex itself, is zero. The ordinate gives the speed of descent of the pair of trailing vortices due to their mutual interaction. After complete roll-up the pair of vortices attain a uniform speed of descent. Due to the uncertainty involved in locating the position of maximum slope from the velocity profile such as that shown on Figure 29, it was found convenient to use the experimentally determined value of the vortex descent speed to locate the position of maximum slope. From Figure 28 the experimental speed of descent is

$$\frac{W_g}{U} = 0.0042\alpha^o \quad . \qquad 5.25$$

The vortex center may also be defined by the position of maximum axial velocity defect which, on theoretical grounds, occurs on the axis of the vortex core; the lateral position of the vortex thus defined is shown by 'tagged' symbols on Figure 28. The two definitions of the vortex center are roughly in mutual agreement. The experimental result is in reasonable agreement with the theoretical prediction of $(\pi/4)D$ vortex core separation after roll-up. During the roll-up stage, the vortex is seen to approach the plane of symmetry, i.e., $y = 0$, then return to the final position of $y = \pi/8D$, approximately substantiating a result of the numerical calculation.

The downstream station where the vortex sheet could be considered to be essentially rolled-up was predicted in Section II.2 to be given by

$$\frac{x}{D}_c \simeq \frac{\pi^3}{16}\frac{A}{C_L} \quad . \qquad 5.26$$

Using $C_{L_{\alpha^o}}/A = 0.01342$, the dimensionless downstream station of roll-up completion is given by

$$\frac{x}{D}_c \simeq 144/\alpha^o \quad , \qquad 5.27$$

and it is shown by the broken line labelled 'complete roll-up' on Figure 28. The predicted station roughly coincides with the station where the vortex core resumes its final lateral position of $y = \pi D/8$, and also attains its uniform speed of descent; both properties of the roll-up process roughly indicate completion of roll-up. (Note that during roll-up, the center of the vortex core does not coincide with the center of vorticity per half wing.)

V.2.2 Decay of the Rolled-up Trailing Vortices

The experimental data will now be compared with the theoretical predictions (Section III). For convenience, the theoretical predictions will be reproduced as comparison proceeds.

The measured velocity profiles in the trailing vortex (such as those shown on Figure 24d) are time averages at positions fixed relative to the wing, and are therefore weighted averages of the theoretically predicted instantaneous profiles. Vortex wandering is believed to cause deviations of the measured profiles from their instantaneous profiles. In Reference 25, because substantial vortex wandering was observed, it was found necessary to account for vortex wandering effects before making the comparison with the experimental data.

However, in the present study, vortex wandering as described in Reference 25 was not observed, and therefore the comparisons that follow are free of corrections for the vortex wandering phenomenon. Furthermore, in the case of a ring wing, maximum velocities in the trailing vortex (Fig. 10) do not peak as much as the maximum velocities in the vortices behind an elliptic or rectangular wing, as evidenced in the typical velocity profiles presented on Figures 24h and 24i for both wings. It is believed, therefore, that vortex wandering effects on peak velocities will not be severe in the case of the ring wing; vortex wandering, however, will add to the uncertainties in the core radius.

Besides vortex wandering, caused by free-stream turbulence, mutual interaction of the vortices will also cause some degree of wandering in addition to distortion of the vortices. In this study the vortices were observed to interact, as evidenced in the non-symmetric tangential velocity profiles; but the mutual interaction of the vortices did not cause serious velocity fluctuations in the vortex core (Fig. 24e). At present, such vortex interactions are not incorporated in the theoretical predictions. The experimental data are, therefore, compared to an ideal case of a circular isolated vortex. The vortex is assumed to form at the trailing edge and then decay from here on. This assumption seems to contradict the finding that the vortices form far downstream from the trailing edge. However, as stated earlier, the roll-up process itself is not free of viscous decay. Placing the initial conditions of the decay process at the trailing edge should therefore be a fair approximation.

V. 2. 2. 1 Axial Velocity

The axial velocity u(r,x) measured relative to the free stream is the sum of two terms. The first term, u_v, is caused by the pressure field induced by the roll-up and decay of the trail vortex. The second term, u_δ, is a velocity defect due to retardation in the boundary layer on the wing. The velocity on the axis of the vortex core, i.e., r = 0, is written as $\Delta U(0)$, where

$$\begin{aligned}\frac{\Delta U(0)}{U} &= \frac{\Delta U_v(0)}{U} + \frac{\Delta U_\delta(0)}{U} \\ &= \frac{1}{2}\left(\frac{\beta}{U}\right)^2 \left[3.08 + \ln\left(4\lambda^2 \frac{x}{D} R_D^{-1}\right) - \ldots\right] \\ &\quad - \chi_\delta \lambda A^{-\frac{1}{2}} \left(\frac{x}{D}\right)^{-\frac{1}{2}}\end{aligned} \qquad 5.28$$

Here $x_{\delta_2} = 0.188$, based on the momentum thickness of a Blasius boundary layer, i.e., $\delta_2 = 1.33\ (\nu C/U)^{\frac{1}{2}}$; x is the distance downstream from the trailing edge of the wing; D is the wing diameter. A is the wing aspect ratio (or diameter to chord ratio, D/C); and R_D is the Reynolds number defined by

$$R_D = \frac{UD}{\nu} \qquad 5.29$$

where U is the free stream velocity or speed of the wing, and ν is the kinematic viscosity. The contraction factor λ (Appendix C) is set equal to 2. The quantity β is related to the wing loading and mechanism of roll-up, and it is given by

$$\beta = \frac{\lambda \Gamma_o}{2D} = \frac{\Gamma_o}{D} \quad . \qquad 5.30$$

The value of β used in the following comparison was obtained from Reference 30 and for A = 2 is given by $\beta = 0.01342\,\alpha^o U$, where α^o is the axial angle of attack in degrees. (The quantity β may also be obtained from Equation A12 by the relation

$$\beta = \Gamma_o/D = U\ (\Gamma_o/UC)/A = UA^{-1}C_L.) \qquad 5.31$$

Figure 30 shows the axial velocity defect. The quantity $\left(-\frac{1}{2}\ A^{\frac{1}{2}}\right)[\Delta U(0)/U - \Delta U_v(0)/U]$ is plotted agains $(x/D)^{-\frac{1}{2}}$. The experimental data was found to fit the theoretical prediction based on δ_2 (the momentum thickness). The agreement is quite reasonable in view of the ambiguity in λ and δ.

V.2.2.2 Tangential Velocity

The tangential velocity near the center of the vortex core is given by

$$v_\theta = \beta \frac{\pi^{\frac{1}{2}}}{2} r \, (4\nu x/U)^{-\frac{1}{2}} \sum_{j=0} (-1)^j \tau^j \; {}_1F_1 \left(\tfrac{1}{2} - j;\ 2;\ -Ur^2/4\nu x\right) \qquad 5.32$$

where $\tau = \frac{4\lambda^2 \nu x}{UD^2} = 4\lambda^2 \frac{x}{D} R_D^{-1}$

and ${}_1F_1$ is the confluent hypergeometric function. The radius of the vortex core, r_1, is defined as the value of r for which v_θ is a maximum. The dimensionless forms of the core radius $\eta_1 = Ur_1^2/4\nu x$, and the maximum tangential velocity v_θ/β, are plotted on Figure 12 as a function of τ. (These were numerically calculated for 10 terms in Equation 5.32.) The dimensionless core radius is linear over a wide range of τ, and can be described by

$$\eta_1 = 0.92 \, \tau^{-0.43} \qquad 5.33$$

from which the core radius r_1 is obtained as

$$\frac{r_1}{D} = 1.42 \, \lambda^{-0.43} \, {\frac{x}{D} R_D^{-1}}^{\,0.28} \ , \qquad 5.34$$

where the contraction factor λ is set equal to 2 .

The axial vorticity ζ_o on the core axis is $2 \, \partial v_\theta/\partial r$ evaluated at $r = 0$, and is given by the dimensionless form

$$\frac{A}{C_L} \cdot \frac{\zeta_o D}{U} = \frac{\pi^{\frac{1}{2}}}{2} \left(\frac{x}{D} \cdot R_D^{-1}\right)^{-\frac{1}{2}} \left[1 - 16 \left(\frac{x}{D} R_D^{-1}\right) + \ldots \right] \qquad 5.35$$

where λ has been set equal to 2, and $\beta = UC_L/A$ has been used.

Figure 31 compares the predicted peak tangential velocity with the measured values, $\overline{W}$. (Since the velocity profile is not symmetric about $r = 0$, $\overline{W}$ was taken equal to half the jump in the vertical velocity as defined in Figure 29.) The nondimensional quantity $(\overline{W}/\alpha^o U)\ (A^{-1}C_{L_{\alpha^o}})$ vs. $(x/D)\ R_D^{-1}$ is plotted. (Here $C_{L_{\alpha^o}} = \partial C_L/\partial\alpha^o$ is the slope of the lift curve.) Considering the assumptions involved, the agreement is reasonably fair. The peak tangential velocity decays as $x^{-0.3}$ approximately, as compared to $x^{-\frac{1}{4}}$, in the case of trailing vortices behind an elliptic wing (Ref. 4).

On the same plot (Fig. 31), the predicted position of complete roll-up is shown for $\alpha^o = 12$ and $R_D = 2,7000$, and roughly agrees with the downstream station where the vortex begins to decay, thus confirming the prediction.

V. 2. 2. 3 Vortex Core Radius

Figure 32 shows predicted and measured values of the core radius, r_1/R, as a function of $(x/D)\ R_D^{-1}$. (Here R is the wing radius and R_D is the Reynolds number based on wing diameter. The symbols with 'tags' indicate that the vortex center was defined by the position of maximum axial velocity defect instead of maximum vorticity.) The contraction factor λ was set equal to 2 in Equation 5. 34 to obtain $r_1/R = 2.1\ ((x/D)/R_D)^{0.28}$. The theoretical prediction underestimates the core radius of the vortex; however, the growth rate is seen to be in reasonable agreement.

In the case of an elliptic wing, the core radius grows with the downstream distance like $x^{\frac{1}{2}}$, which is a much faster growth rate than $x^{0.28}$ as obtained for the ring wing. From Reference 5, the core radius of the trailing vortex behind an elliptic wing is given by

$$r_1 = 2.92 \, ((x/b)R_b)^{\frac{1}{2}} \, b, \qquad 5.36$$

where b is the wing span, and R_b is the Reynolds number based on wing span. A simple comparison is made here to illustrate the vortex core size difference between the two wings, i. e., the ring and elliptic wings.

Consider an elliptic wing with wing span equal to the ring wing diameter and let both wings fly at the same Reynolds number, i. e., $R_b = R_D$. Then, according to the theoretical predictions, the core radius of the trailing vortices from both wings will be equal at a downstream station $x = 9.6 \times 10^{-3} R_D$ wing diameters (or spans); the core radius being 0.28 diameters (or spans). For downstream stations less than $9.6 \times 10^{-3} R_D$, the vortex core in the case of a ring wing, is larger than that of an elliptic wing.

It is understandable that initially a ring wing has a larger vortex core than an elliptic wing because the initial vorticity in the vortex cores are differently distributed. In the case of the ring wing, vorticity is more evenly distributed over the wing surface, as compared to an elliptic wing whose vorticity distribution is very much concentrated at the wing tips. Vorticity in the vortices formed behind the wings is similarly distributed. Axial vorticity, in the case of a ring wing generated vortex, is distributed over a wide cross sectional area, whereas in the case of an elliptic wing, vorticity is concentrated at the vortex center. Thus, the vortex core is initially smaller in the latter case than in the former. For the same reason, tangential velocities in the ring wing generated vortex are much lower than the tangential velocities in the vortex behind an elliptic wing. The vortex wake behind a ring wing is associated with less energy as compared to an elliptic wing. Consequently, for the same lift, the ring wing has less induced drag[†] than the elliptic wing spanning the wing diameter.

The idea of drag reduction by distributing the vorticity over a wider surface (on the wing) is incorporated in the wing design by end plates. It will be interesting to investigate the practicality and aerodynamic effects of replacing the end plates by ring wings. It is believed that such a wing configuration, if possible, will also alleviate the trailing vortex hazard.

V. 2. 2. 4 Axial Vorticity on the Vortex Core Axis

On Figure 33, Equation 5. 35 is compared to the experimental data. It is seen that the theory highly over-predicts axial vorticity on the core axis. However, vorticity decays as $x^{-\frac{1}{2}}$, as predicted. (cf. In the case of an elliptic wing, vorticity on the core axis decays like $x^{-3/4}$, Ref. 5.) Note that the predicted

---

[†] For a ring wing $D_i = L^2/(4D^2q)$ and for an elliptic wing $D_i = L^2/b^2q$, where $q = \frac{1}{2}\rho U^2$.

station of complete roll-up coincides roughly with the onset of decay.

V. 2. 2. 5 Maximum Downwash in Plane of Symmetry

Finally, the maximum downwash in the plane of symmetry is plotted on Figure 34 to show the Reynolds number dependence. The downwash velocity is seen to decay like $x^{-0.3}$; however, the experiments were not conducted over a wide enough range of Reynolds numbers to warrant any conclusive remarks. Again, the predicted complete roll-up station is demonstrated.

V. 3 Suggested Future Investigations

Some areas of investigation that may be of interest in connection with this study are listed below:

a) Experiments convering higher Reynolds numbers than those reported here should be conducted; this will ensure a thinner wake and better approximate the mathematical model of the vortex sheet.

b) Measurements of vorticity distribution in the vortex wake should be interesting. In this respect, an LDV vorticity meter presently being developed at GALCIT will prove to be an invaluable tool. Vorticity measurements should be compared to measured loading on the ring wing to determine loss of vorticity downstream in the wake due to frictional heating effect.

c) Photographs of the vortex wake cross section will be invaluable.

d) Experiments may be conducted for various wing aspect ratios.

e) The mutual interaction of the trailing vortices should be incorporated in the theory.

f) Numerical computations of the sheet vortex roll-up process may be repeated, using a different scheme to reduce point vortex randomization effects. In particular, methods due to Fink and Soh or Moore (Section II) are suggested.

VI CONCLUDING REMARKS

The vortex sheet emanating from the trailing edge of a thin cylindrical ring wing in a nonaxial flow has been shown to roll up to form a pair of counter rotating trailing vortices, spaced by $\pi/4$ wing diameters. The roll up process may be classified into three phases. These are:

(a) Distortion phase
(b) Roll-up phase
(c) Decay phase

In the distortion phase, the vortex sheet simply distorts in shape under its own induced velocities. Vorticity is redistributed on the sheet to concentrate at two points that originate from the upper half of the wing. The vortex sheet then rolls up about these points into a pair of doubly branched spirals whose turns viscosity smoothes out. These points of roll-up origins at the trailing edge are numerically determined to be approximately 52 degrees from the upper side of the median plane of symmetry. The origins of roll up have been observed by flow visualization techniques.

In practice, the beginning or the end of roll-up is not well defined. Numerical calculations suggest that roll-up begins at roughly $0.26\ A/C_L$ diameters downstream from the trailing edge. The downstream station where the vortex sheet may be considered to be essentially rolled up has been estimated to be approximately $2A/C_L$ diameters; this has been observed for a wing aspect ratio of two.

The trailing vortex has been shown to decay according to theory based on Moore and Saffman's model of laminar trailing vortices.

APPENDIX A

Development and Strength of the Trailing Vortex Sheet Generated by a Ring Wing

Consider a thin cylindrical ring wing in a nonaxial flow (i.e., the ring wing is at an axial angle of attack). On the surface of the ring wing, a pressure distribution develops in a manner that causes a cross-flow as depicted in Figure 2. On the inner surface of the wing, the fluid will tend to flow from the pressure side (the upper part) to the suction side (the lower part). A similar flow develops on the outer surface, except that here the pressure side is at the lower half of the wing and the suction side is at the upper half of the wing. When the inner and outer flows meet at the trailing edge of the wing, the tangential velocities on the inner and outer surfaces are in opposite directions. Thus a surface of discontinuity, in which vorticity is distributed, is formed. The trailing vortex sheet thus formed is a thin cylindrical shell with a circular cross section of radius R, the ring wing radius (Fig. 2). The vorticity has opposite signs on the adjacent sides of the median plane of symmetry.

The cylindrical trailing vortex sheet is unstable, however, and will first distort in shape due to its own induced velocities and roll up as sketched in Figure 1b. Analytical treatment of the roll-up process is difficult. The usual procedure is to numerically calculate the evolution of an infinite vortex sheet in an unsteady flow. This problem is treated in Section II.

The vorticity distribution in the vortex sheet may be obtained by the following analogous problem. Consider an infinite cylindrical fluid inside an infinitesimally thin rigid cylindrical shell, with radius R. Now let the infinite cylinder of fluid descend steadily, through a fluid medium, with velocity W_o, perpendicular to the cylinder axis. Suppose at some time during the motion, the thin shell interface is made to vanish instantly. An unstable surface of discontinuity is thus created. The instantaneous flow field is equivalent to the flow about an infinite cylinder, which is well known.

With respect to a stationary coordinate system, the instantaneous tangential velocity on the outer surface of the discontinuity surface is given by

$$v_\theta^+ = W_o \sin\varphi \quad . \qquad \text{A1}$$

On the inner surface, the instantaneous tangential velocity is

$$v_\theta^- = - W_o \sin\varphi \quad . \qquad \text{A2}$$

The jump in tangential velocity across the discontinuity surface is equivalent to the circulation per unit arc length, $\omega(\varphi)$, i. e., the vorticity. Thus

$$\omega(\varphi) = v_\theta^+ - v_\theta^- = 2\, W_o \sin\varphi \quad . \qquad \text{A3}$$

The circulation distribution $\Gamma(\varphi)$ is then given by integrating Equation A3. One obtains

$$\Gamma(\varphi) = \int_{\varphi}^{\pi/2} \omega(\varphi)\ R d\varphi = 2RW_o \cos\varphi \qquad \text{A4}$$

where φ is a polar angle measured from the bottom of the vertical plane of symmetry.

A practical problem, in view of the above described problem, is the case of the motion of gas bubbles in a fluid medium. The vortex sheet formed in this case will be spherical, and will roll up into a vortex ring depending on shear stresses at the interphase. The "mushrooming" effect from atomic blasts may also be described in a similar fashion.

The strength of the trailing vortex sheet is equivalent to the wing loading. For large diameter-to-chord ratios, the well-known Prandtl's lifting line theory may be applied to the ring wing. From Reference 27, the circulation distribution is

$$\Gamma(\varphi) = \Gamma_o \cos\varphi \qquad \text{A5}$$

where Γ_o is the root circulation. From Equation A4

$$W_o = \Gamma_o/2R = \Gamma_o/D \qquad \text{A6}$$

which is the initially induced downwash inside the infinite vortex sheet. The initial downwash is constant everywhere within the cylindrical sheet. The initial mean tangential velocity on the vortex sheet is zero and the mean radial velocity $v_r = W_o \cos\varphi$. The initial radial velocity distribution explains why the sheet first undergoes distortion before rolling up. (By contrast, the induced normal velocity on the vortex sheet generated by an elliptically loaded wing is constant and equals Γ_o/b, where b is the wing span. In this case the sheet rolls up immediately.)

From lifting line considerations, the root circulation for the ring wing is given by

$$\Gamma_o = \frac{\pi U C \alpha}{1 + \pi/2A} \quad , \qquad \text{A7}$$

where α is the axial angle of attack, U is the wing speed, and A is the aspect ratio defined by the diameter-to-chord ratio, i.e., $A = D/C$ (the two-dimensional sectional lift coefficient slope of 2π is used here). The ring wing lift coefficient is then

$$C_L = \frac{\Gamma_o}{UC} \quad , \qquad \text{A8}$$

and the induced drag coefficient is

$$C_{D_i} = \frac{C_L^2}{2A} \quad . \qquad \text{A9}$$

For large aspect ratios, Equation A7 is a valid approximation and

$$C_L = \frac{\pi \alpha}{1 + \pi/2A} \qquad \text{A10}$$

and for very small aspect ratios, i.e., $C >> D$, the downwash $W_o \simeq U\alpha$, giving $\Gamma_o = UD\alpha$ and from Equation A8

$$C_L = A\alpha \ . \qquad \text{A11}$$

The drag and lift coefficients are defined as

$$C_L = \frac{\text{Lift}}{\frac{1}{2}\rho\ U^2 S}$$

$$C_{D_i} = \frac{\text{Induced Drag}}{\frac{1}{2}\rho\ U^2 S}$$

where ρ is the fluid density and $S = \pi DC$ is the wing surface area.

Weissinger (Ref. 24) uses linearized lifting surface theory to calculate the aerodynamic coefficients of the ring wing. The calculations are long and involved but the results (presented in Ref. 22) are in excellent agreement with the experimental data (Ref. 29). He gives an approximation to the lift coefficient of a cylindrical ring wing by

$$C_L = \frac{\pi A \alpha}{A + \pi/2 + \arctan(1.2/A)} \quad . \qquad \text{A12}$$

(Note that this approximation matches with Equations A10 and A11.) In the practical range of aspect ratio, the lifting line theory over-predicts lift by about 10-20%.

APPENDIX B

B.1. Estimate of Circulation Distribution, $\Gamma(r)$, within Rolled-up Spiral

The initial distribution of circulation about the cylindrical vortex sheet (Fig. 3) is given by $\Gamma = \Gamma_o \sin\theta$ (Eq. A5), where θ is measured from the horizontal diameter. The problem is to determine the circulation distribution about circles concentric with the center of the spiral formed by the roll-up of the infinite vortex sheet.

It is assumed that the central portion of the spiral consists of approximately concentric circles. This assumption is valid in the inner portion where the spiral consists of tightly wound turns and, due to the double branch nature of the spiral, the center of the spiral closely approximates the vorticity centroid.

The vortex sheet rolls up into a doubly branched spiral whose center originates from a point, $\theta = \theta_o$, on the original cylindrical vortex sheet. Results from the numerical calculations (Section II) give $\theta_o = \arccos(\pi/4)$, approximately. Referring to Figure 3a, take a contour C_s enclosing θ_o such that the arc lengths, s, on both sides of θ_o are equal. The net vorticity Γ_c, in the segment of vortex sheet enclosed by the contour is

$$\Gamma_c = \Gamma_o \sin(\theta_o + s/R) - \Gamma_o \sin(\theta_o - s/R) \qquad \text{B1}$$

$$= 2\,\Gamma_o \cos\theta_o \sin(s/R)$$

where R is the radius of the cylindrical vortex sheet.

The sheet segment enclosed by the contour C_s rolls up into a doubly branched spiral enclosed by a circle of radius r, concentric with the center of the spiral (Fig. 3). The original net vorticity in the sheet segment is then equal to the net vorticity in the spiral enclosed by the circle.

In the inner portion of the spiral where the spiral turns are roughly circular, the mean radial velocity is zero; furthermore, the flow is inviscid. Thus the net vorticity in the circle (i. e., the circulation about the circle) is not a function of time. By making the linear transformation $s \rightarrow \lambda r$, relating the arc length to the radius of the circle, and putting $\cos\theta_o = \pi/4$ in Equation B1, the net vorticity, $\Gamma(r)$, within the spiral is roughly given by

$$\Gamma(r) = \frac{\pi}{2}\Gamma_o \sin(\lambda r/R), \quad \frac{\lambda r}{R} < \frac{\pi}{2} \qquad \text{B2}$$

$$= \frac{\pi}{2}\Gamma_o \qquad \frac{\lambda r}{R} \geq \frac{\pi}{2}$$

where λ is a dimensionless constant known as the contraction factor. It indicates the size of the circle into which a segment of the original vortex sheet rolls (Ref. 5). In Appendix C, the value of λ is estimated to be 2.

From the approximations outlined above, it is seen that a fraction of $\pi/4$, of the original total vorticity per half wing $2\Gamma_o$, is rolled up. The remaining vorticity is contained in the unrolled portion of the vortex sheet.

B. 2 Nature of the Rolled-up Spiral

From Reference 5, for a circulation distribution of the form $\Gamma(r) = 2\gamma(\lambda r)^{1-n}$, the polar equation of the inner spiral is given by

$$r = {\frac{\gamma\lambda^{1-n}}{\pi}\;\frac{t}{\theta-\theta_\infty}}^{\frac{1}{1+n}} , \qquad \text{B3}$$

and the radius of the central portion is

$$a_s\,(t)\ \alpha\ {\frac{\gamma\lambda^{1-n}}{\pi}\;t}^{\frac{1}{1+n}} . \qquad \text{B4}$$

In the case of the ring generated vortex sheet, $\Gamma(r) \sim 2\,\frac{\pi\Gamma_o}{2D}\,(\lambda\,r)$, for $r \rightarrow 0$. Thus $n = 0$ and $\gamma = \pi\Gamma_o/2D$. The polar equation[†] is

$$r = \frac{\lambda\,\Gamma_o}{2D}\;\frac{t - t_o}{\theta-\theta_\infty} \qquad \text{B5}$$

where θ_∞ is a constant of integration. The radius of the central portion of the spiral is

$$a_s(t)\ \alpha\ \frac{\lambda\,\Gamma_o}{2D}\,(t - t_o) \qquad \text{B6}$$

where t_o is the time when the sheet begins to roll up.

Results obtained here are compared to the numerical results in Section V.

[†] In the case of the ring wing the spiral consists of two branches. The polar equation of the other branch is obtained by replacing θ by $\theta + \pi$ in Equation B5.

APPENDIX C

Estimate of the Contraction Factor λ

Three methods are outlined below to find an approximate value for λ. The first two are based on similar derivations from Reference 5.

(a) Betz' Theorem of Conservation of Angular Impulse

Betz theorem (Ref. 32) states that for a given net vorticity in a strip of a vortex sheet (0, s) say, the angular impulse, J, measured relative to the centroid of vorticity, remains constant as the strip rolls up into a spiral to fill a circle of radius r. The theorem is based on the assumption that the change in A due to the induced velocity caused by the vorticity external to the considered spiral is negligible. Therefore, the theorem should be valid in the inner portion of the spiral where vorticity is concentrated.

Now consider the initial cylindrical vortex sheet with vorticity distribution $\omega(\theta) = \Gamma_o R^{-1} \cos\theta$. The net vorticity in the arc length s (Fig. 3) is given by

$$\Gamma(s) \sim \frac{\pi\Gamma_o}{4R} s \qquad \text{C1}$$

and

$$\omega(s) = \frac{d\Gamma}{ds} = \frac{\pi\Gamma_o}{4R} = \omega_o \quad . \qquad \text{C2}$$

The center of gravity of vorticity in the strip $\bar{s}$ is given by

$$\bar{s} = \frac{\int_o^s \omega(s')\, s'\, ds'}{\int_o^s \omega(s')\, ds'} = \tfrac{1}{2}s \quad , \qquad \text{C3}$$

ignoring the curvature in the arc. The angular impulse relative to $\bar{s}$ is

$$J_o = -\tfrac{1}{2}\rho \int_0^s \omega(s')\,(s' - \bar{s})^2\, ds' \qquad \text{C4}$$

$$= -\frac{1}{24}\rho\, \omega_o s^3 \quad .$$

The vorticity in s is then assumed to roll up into a circle of radius r (Fig. 3) around which the circulation contributed by the segment s is

$$\Gamma(r) = \omega_o s(r) \quad . \qquad \text{C5}$$

The angular impulse of vorticity within the circle is given by

$$J_r = -\tfrac{1}{2}\rho \int_0^r r'^2 \frac{d\Gamma}{dr'}\, dr'$$

$$= -\tfrac{1}{2}\rho\, \omega_o \int_0^r r'^2 \frac{ds}{dr'}\, dr' \qquad \text{C6}$$

By Betz approximation, $J_r = J_o$. Equating C4 and C6 and differentiating, one obtains

$$s = 2r \qquad \text{C7}$$

and

$$\lambda = 2 \qquad \text{C8}$$

where λ , known as the contaction factor, indicates the radius of the circle into which vorticity in a segment of the vortex sheet is compressed.

(b) Conservation of Energy (Refs. 5 and 31).

In this approach, the vortex core radius is obtained by equating the energy per unit length of the vortex wake to the induced drag (i. e., energy spent to generate a unit length of the trailing vortex sheet).

The vortex sheet is assumed to completely roll up into a pair of circular trailing vortices with core radius r_o. The distance of separation of the vortex cores, D', may be obtained from conservation of vertical impulse. Before roll-up the vertical impulse, due to the cylindrical vortex sheet with vorticity distribution $\omega(\varphi) = 2D^{-1}\,\Gamma_o\,\sin\varphi$, is given by

$$2\,\rho \int_0^{\pi} \omega(\varphi)\,\frac{D}{2}\,\sin\varphi\,\frac{D}{2}\,d\varphi = \rho\,\frac{\pi}{2}\,D\Gamma_o\ .$$

After complete roll-up, the impulse is

$$2\,\rho\,(2\,\Gamma_o)\,\frac{D'}{2}\ .$$

Equating the two quantities, one obtains

$$D' = \frac{\pi}{4}\,D$$

where D is the diameter of the ring wing.

The circulation distribution in the vortex cores is taken to be

$$\begin{aligned} \Gamma\,(r) &= 2\Gamma_o\,\sin\,(2\lambda r/D), & \frac{2\lambda r}{D} &< \frac{\pi}{2} \\ &= 2\Gamma_o & \frac{2\lambda r}{D} &\geq \frac{\pi}{2}\ . \end{aligned}$$

(Since complete roll-up is considered, the total vorticity shed per half wing, $2\Gamma_o$ is used (Eq. B2 of Appendix B).)

The kinetic energy per unit length of the vortex wake is approximately given by

$$K.E. = \frac{\rho}{2\pi} \int_0^{r_o} \frac{\Gamma(r)^2}{r} dr + \frac{\rho}{2\pi} \int_{r_o}^{D'} \frac{(2\Gamma_o)^2}{r} dr$$

$$= \frac{\rho}{2\pi} (2\Gamma_o)^2 \left[\ln \frac{D'}{r_o} + \frac{1}{2} \mathrm{Cin}(\pi) \right] , \qquad C12$$

where $\quad \mathrm{Cin}\ (\pi) = \int_0^{\pi} \frac{1-\cos x}{x} dx = 1.648 \quad .$

The induced drag on the ring wing is given by

$$D_i = \frac{\pi}{4} \rho \Gamma_o^2 \quad . \qquad C13$$

From Equations C12 and C13, one obtains

$$r_o \simeq 0.664\ D' = 0.52\ D \qquad C14$$

and with $2\lambda r_o/D = \pi/2$, one gets

$$\lambda \simeq 1.57 \quad . \qquad C15$$

Note that the estimated core radius is greater than half the vortex separation, thus violating the assumption that the vortex pair does not interact. The vortices actually interact and distort to take on an elliptic shape.

(c) Geometric Consideration

It is assumed that axial velocities caused by the rolling up of the vortex sheet are negligible compared to the free stream velocity. This is a fair assumption for light loading (i. e., for small angles of attack). Since no fluid crosses the cylindrical vortex sheet, then by mass conservation the cross sectional area enclosed by the vortex sheet must necessarily remain constant as the sheet rolls up.

The cylindrical vortex sheet is assumed to roll up into a pair of circular vortices with radius r_o. The cross sectional area of each vortex is then πr_o^2. Half the initial area enclosed by the cylindrical vortex sheet is $(\pi/8)D^2$. Equating the two quantities, one obtains

$$r_o \simeq 0.35D, \qquad \text{C16}$$

and with $2\lambda r/D = \pi/2$ one gets

$$\lambda \simeq 2.2 \quad . \qquad \text{C17}$$

The values of λ, obtained by each of the three different methods above, are of the same order of magnitude. However, they are not exact and should be taken as approximate values. In particular, the method by geometric consideration does not take into account the fact that fluid initially outside the cylindrical sheet is entrained into the vortex. Furthermore, the vortex sheet does not completely roll-up. It seems the entrained fluid is balanced by fluid enclosed by the unrolled-up portions of the sheet. Thus, the rather crude method by geometric considerations gives a value of λ which is quite close to the value estimated by Betz theorem, which is reasonably appropriate for the inner portion of the rolled-up spiral. The method by energy considerations is also not quite appropriate since it concerns only the final state of roll-up. When required, $\lambda = 2$ is used in this investigation.

REFERENCES

1. Kaden, H., "Aufwicklung einer unstabilen Unstetigkeitsfläche," Ingenieur-Archiv 2, pp. 140-168, 1931. (Library Translation No. 403.)

2. Anton, L., "Ausbildung eines Wirbels ander Kante einer Platte," Gottingen Dissertation, Ingenieur-Archiv, vol. X, pp. 411-427, 1939, (T.M. 1398).

3. Prandtl, L., "Über die Entstehung von Wirbeln in der Idealen Flüssigkeit mit Andwendung auf die Tragflügeltheorie und andere Aufgaben," Vorträge aus dem Gebiete der Hydro -und Aerodynamik (Innsbruck 1922), ed. von Karman und Levi-Civita, Springer, Berlin, pp. 23-25 and 27-33, 1924. (Library Translation No. 1099.)

4. Saffman, P.G., "The Structure and Decay of Trailing Vortices," Archives of Mechanics 26, 3, pp. 423-439, Warsaw, 1974.

5. Moore, D.W. and Saffman, P.G., "Axial Flow in Laminar Trailing Vortices," Proc. Roy. Soc. A333, pp. 491-508, 1973.

6. Moore, D.W., "The Discrete Vortex Approximation of a Finite Vortex Sheet," Calif. Inst. of Tech. Report AFOSR-1804-69, 1971.

7. Moore, D.W., "A Numerical Study of the Roll-up of a Finite Vortex Sheet," J. Fluid Mech 63, 2, pp. 225-235, 1974.

8. Olsen, J.H., Goldburg, A., and Rogers, M. (eds), Aircraft Wake Turbulence and its Detection, Plenum Press, New York, 1971.

9. Kucheman, D. (ed.), Progress in Aeronautical Sciences, vol. 7, Pergamon Press, London, 1966.

10. Rosenhead, L., "The Formation of Vortices from a Surface of Discontinuity," Proc. Roy. Soc. A134, pp. 170-192, 1931.

11. Westwater, F.L., "Rolling Up of the Surface of Discontinuity behind an Aerofoil of Finite Span," Aero Res. Council, R & M, No. 1692, 1935.

12. Stewart, H.J., "The Aerodynamics of a Ring Airfoil," Quart. Appl. Math. 2, pp. 136-141, 1944.

13. Birkhoff, G. and Fisher, J., "Do Vortex Sheets Roll Up?" Rend. Circ. Mat. Palermo, Ser. 2, 8, pp. 77-90, 1959.

REFERENCES (Cont.)

14. Hama, F.R. and Burke, E.R., "On the Rolling-Up of a Vortex Sheet," Univ. of Maryland Tech. Note BN-220, 1960.

15. Takami, H., "Numerical Experiment with Discrete Vortex Approximation, with Reference to the Rolling Up of a Vortex Sheet," Stanford Univ. Report SUDAER 202, 1964.

16. Kuwahara, K. and Takami, H., "Numerical Studies of Two-dimensional Vortex Motion by a System of Point Vortices," J. Phys. Soc. Japan 34, p. 247, 1973.

17. Chorin, A.J. and Bernard, P.S., "Discretization of a Vortex Sheet, with an Example of Roll-up," J. Comp. Phys. 13, pp. 423-429, 1973.

18. Fink, P.T. and Soh, W.K., "Calculation of Vortex Sheets in Unsteady Flow and Applications in Ship Hydrodynamics," Report Nav/ARCH 74/1, 1974.

19. Lamb, H., Hydrodynamics, 6th Edition, Dover Publications, pp. 214-220, 1945.

20. Batchelor, G.K., An Introduction to Fluid Dynamics, Cambridge Univ. Press, pp. 528-532, 1967.

21. Weissinger, J., "Theoretical Investigations on Ring Wing Airfoils," ARDC AF 61 (514) - 1207, (AFOSR TN 60-343), 1960.

22. Weissinger, J., Advances in Aeronautical Sciences, vol. 2, ed. von Karman, Pergamon Press, pp. 798-831, 1959.

23. Weissinger, J., "Ring Airfoil Theory. Problems of Interference and Boundary Layer," ARDC AF 61(514)-1207, (AFOSR TN 59-226), 1959.

24. Weissinger, J., "Zur Aerodynamik des Ringflügels. I. Die Druckverteilung dünner, fast drchsymmetrischer Flügel in Unterschallströmung," DVL-Ber, Nr. 2, 1955. (U.S. Navy-DTMB Aero. Re. 899.)

25. Baker. G.R., Barker, S.J., Bofah, K.K. and Saffman, P.G., "Laser Anemometer Measurements of Trailing Vortices in Water," J. Fluid Mech. 65, part 2, pp. 325-336, 1974.

REFERENCES (cont.)

26. Orloff, K., and Grant, G., "The Application of a Scanning Laser-Doppler Velocimeter to Trailing Vortex Definition and Alleviation." AIAA Paper, no. 73-680, 1973. (TMX-62, 243, 1973.)

27. Ribner, H. S., "The Ring Airfoil in Non-axial Flow," J. Aero. Sc. 14, p. 529, 1947.

28. Fage, A. and Simmons, L. F. G., "An Investigation of the Airflow Pattern in the Wake of an Aerofoil of Finite Span," Phil. Trans. Roy. Soc. A225, pp. 303-330, 1925.

29. Fletcher, H. S., "Experimental Investigation of Lift, Drag, and Pitching Moment of Five Annular Airfoils," NACA TN 4117, 1957.

30. Reynolds, J. F., "Lifting-Surface Theory Applied to Isolated Ring Wings at Angle of Attack," NAVWEPS Rep. 8401, 1963.

31. Spreiter, J. R. and Sacks, A. H., "The Rolling Up of the Trailing Vortex Sheet and its Effect on the Downwash Behind Wings," J. Aero Sci. 18, 21, 1951.

32. Betz, A., "Verhalten von Wirbelsystemen," Z. f. a. M. M., vol. X12, no. 3, pp. 164-174, 1932. (TM No. 713.)

33. Roshko, A., "On the Development of Turbulent Wakes from Vortex Streets," Ph. D. Thesis, Calif. Inst. of Tech., 1952.

34. Friedrichs, K. O., Special Topics in Fluid Dynamics, Gordon and Breach Science Publishers, Inc., New York, pp. 121-131, 1966.

35. Dimotakis, P. E., "Single Scattering Particle Laser Doppler Velocimetry," (to be published in J. Fluid Mech.) 1975.

36. Dimotakis, P. E., "Single Scattering Particle Laser Doppler Measurements of Turbulence," 1975 (to be published).

37. Dimotakis, P. E., and Lang, D. B., "Single Scattering Particle Laser Doppler Velocimetry," Bull. Am. Phys. Soc., p. 1145, 1974.

38. Durst, F., and Whitelaw, J. H., "Optimization of Optical Anemometers," Proc. Roy. Soc. A324, pp. 157-181, 1971.

REFERENCES (cont.)

39. Wang, C., "Instantaneous Turbulence Velocity Measurement by Laser Doppler Velocimeter," Appl. Phys. Letter 20, p. 339, 1972.

40. Yeh, Y. and Cummins, H. Z., "Localized Fluid Flow Measurements with an He-Ne Laser Spectrometer," Appl. Phys. Letter 4, p. 176, 1964.

41. Abramovitz, M. and Stegun, I. A., Handbook of Mathematical Functions, Dover Publications, New York, 1964.

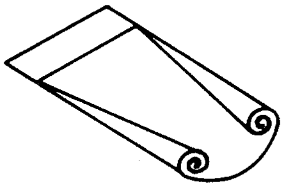

Fig. 1a Prandtl's Drawing

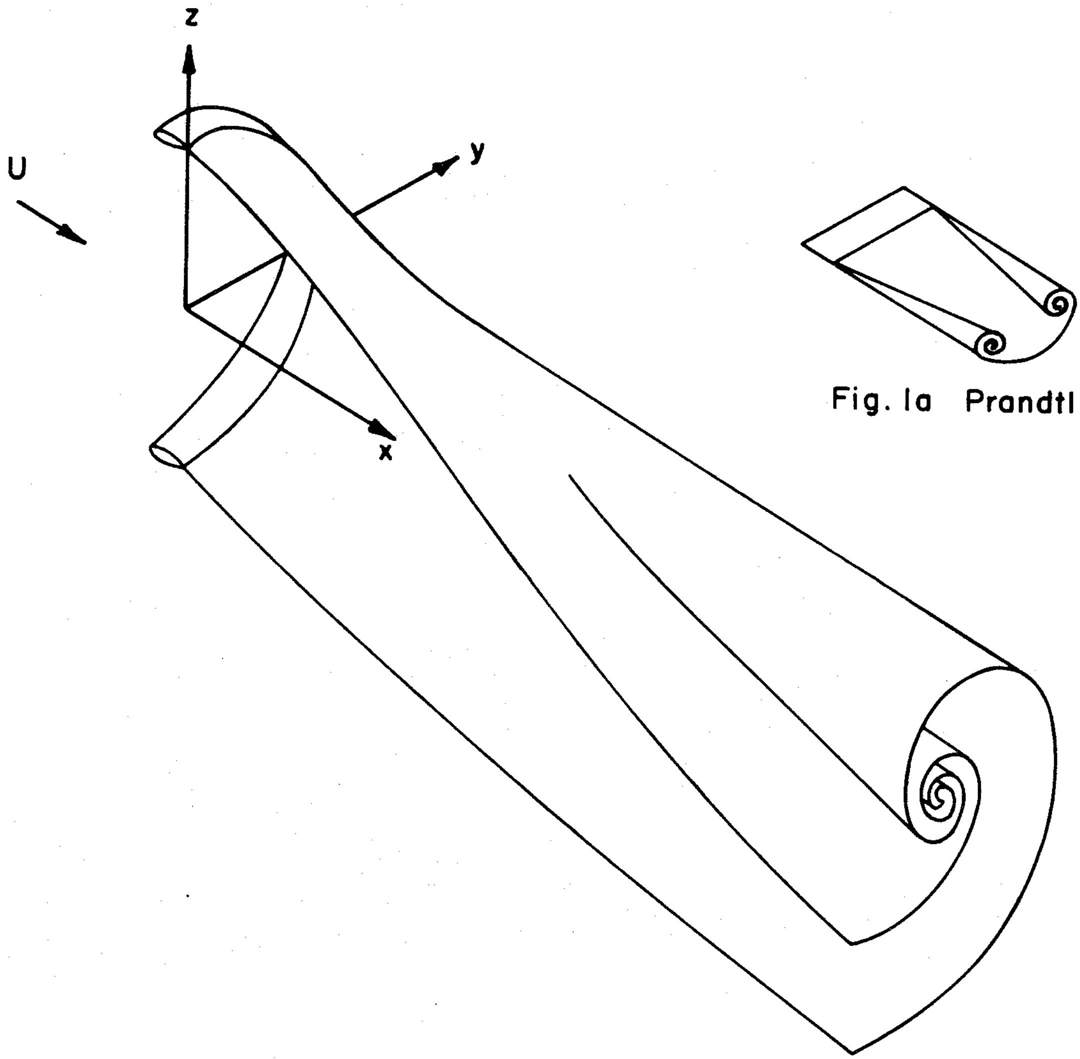

FIG. 1b SCHEMATIC OF THE ROLL-UP OF THE CYLINDRICAL VORTEX SHEET BEHIND A RING WING

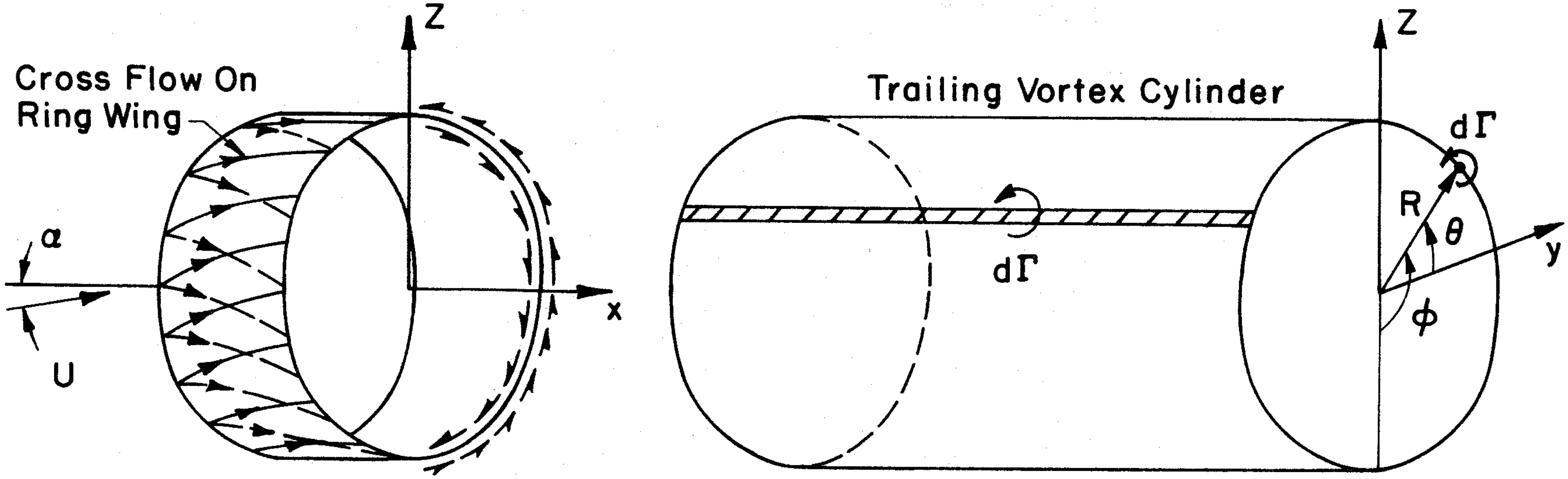

FIG. 2 FORMATION OF TRAILING VORTEX SHEET (SCHEMATIC), $\omega(\phi) = \Gamma_o R^{-1} \sin \phi$

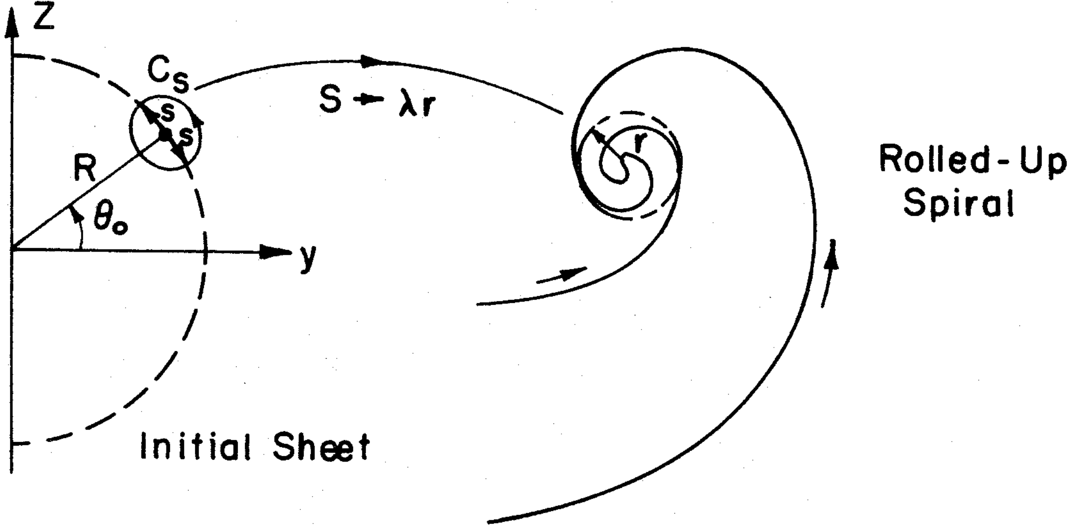

FIG. 3 ROLL-UP OF VORTEX SHEET INTO A SPIRAL

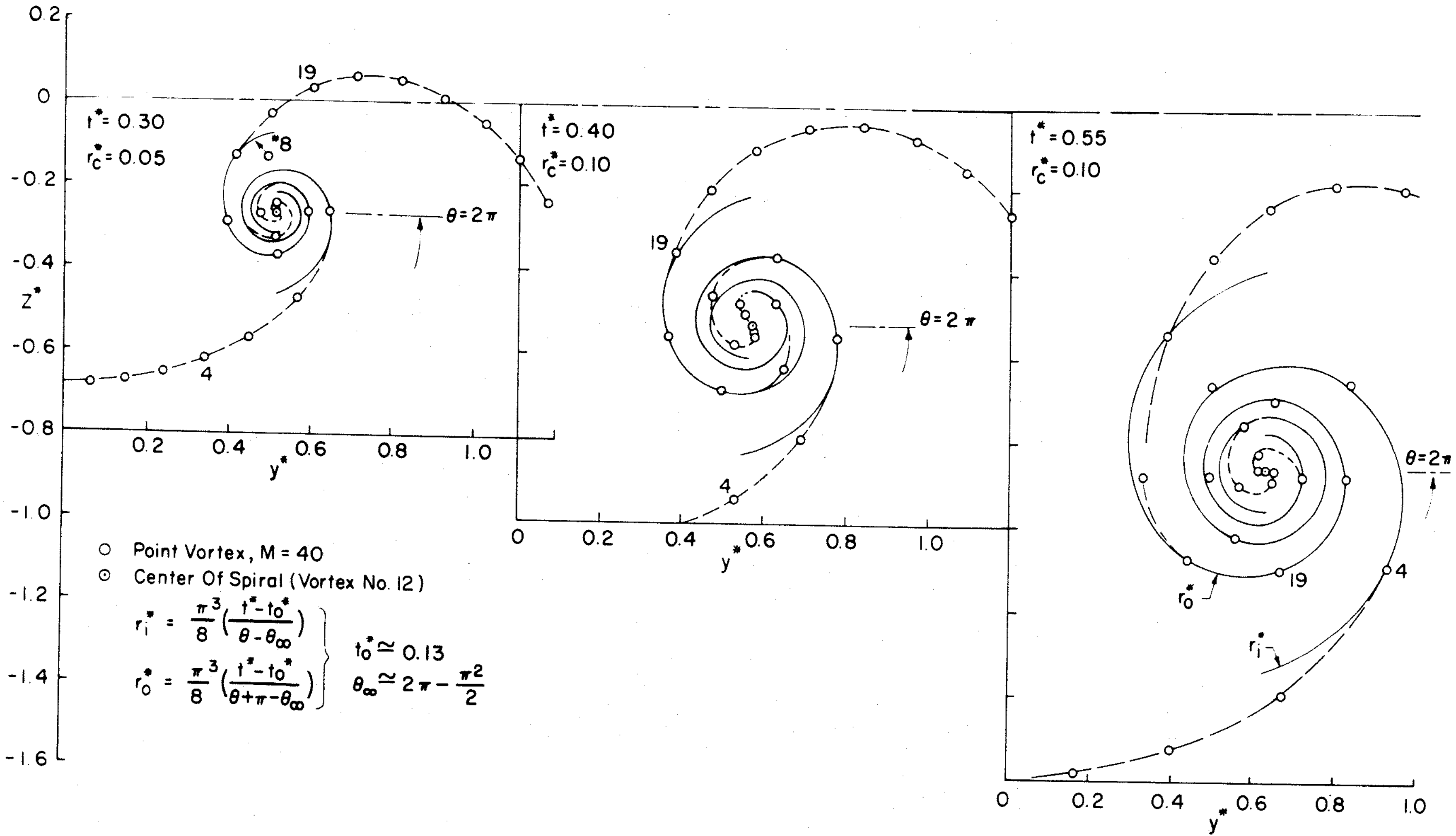

FIG. 4 COMPARISON OF NUMERICAL DATA TO THEORETICAL SPIRAL SHAPE

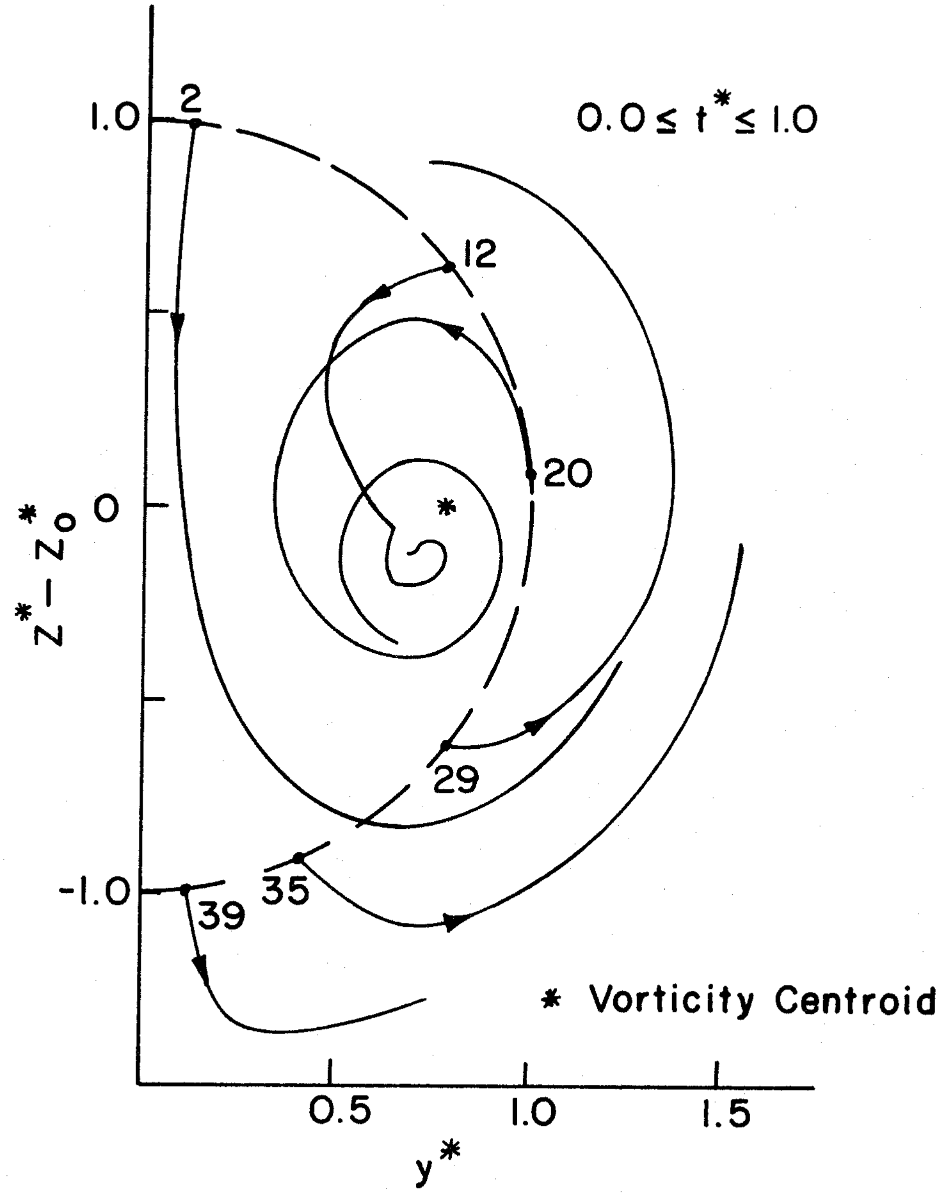

FIG. 5 POINT VORTEX TRAJECTORIES RELATIVE TO VORTICITY CENTROID, M=40

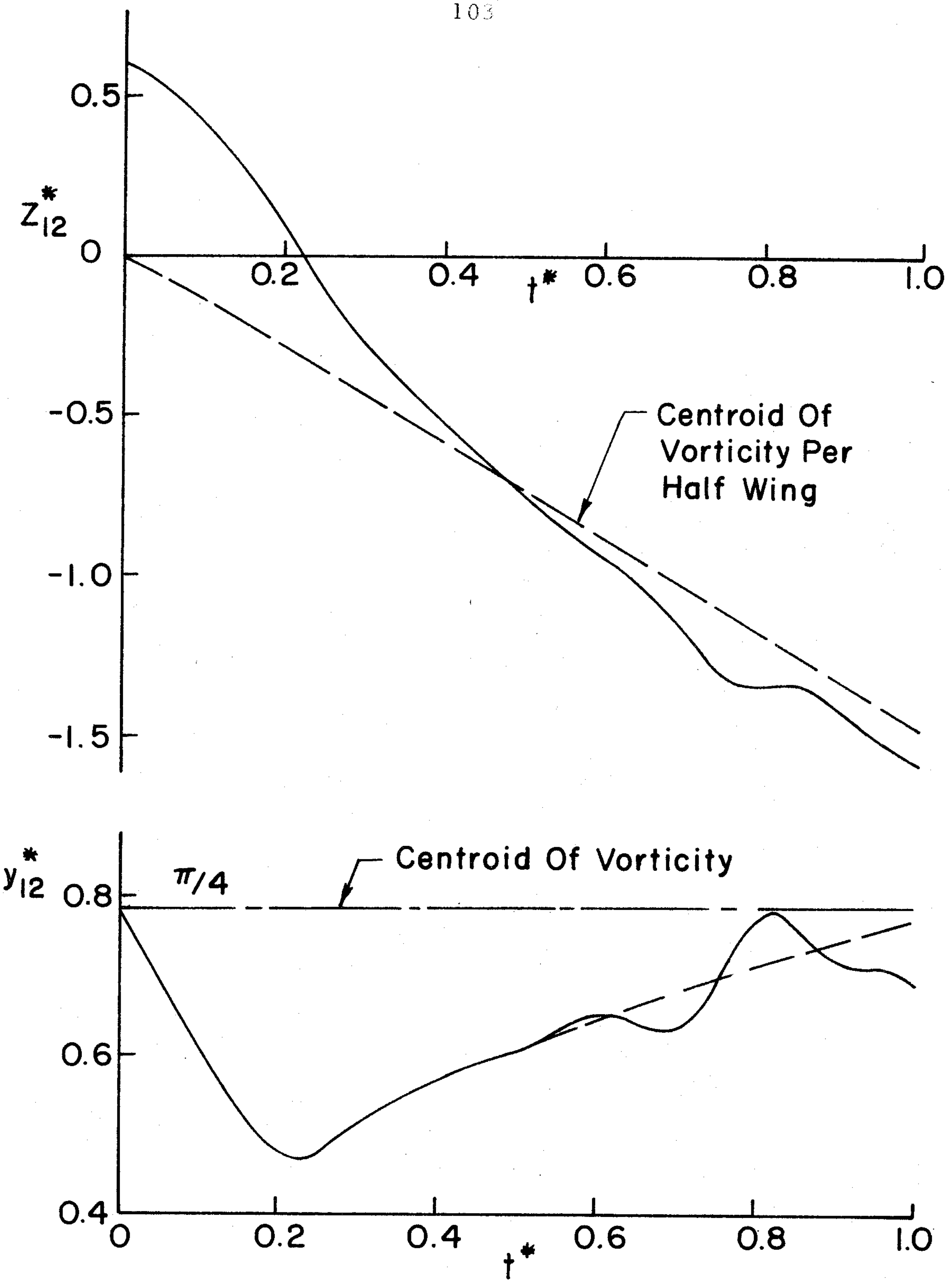

FIG. 5b POSITION OF POINT VORTEX NUMBER 12 AS CENTER OF SPIRAL

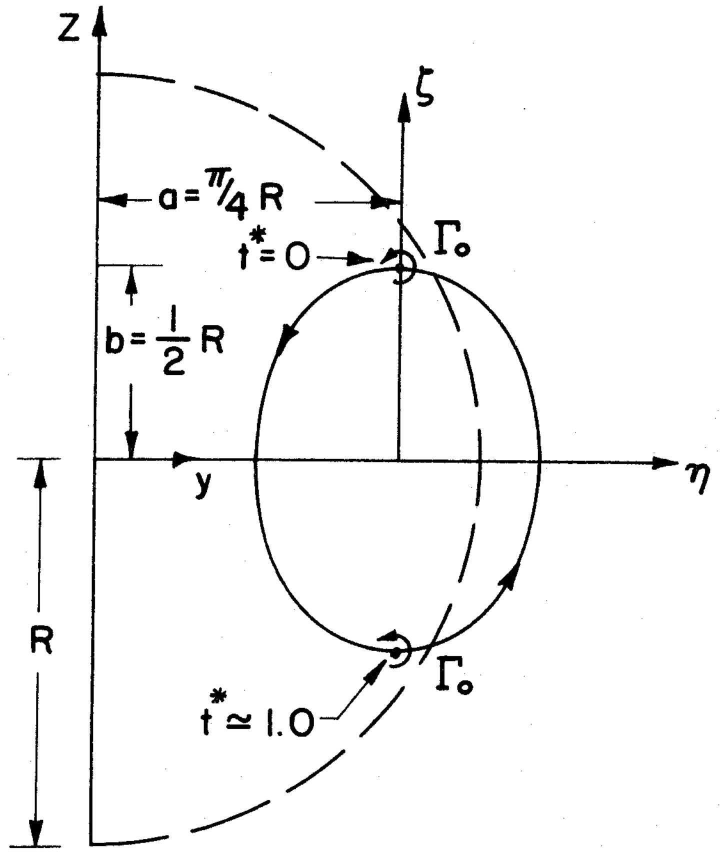

FIG. 6 ORBITAL PATH OF TWO POINT VORTICES

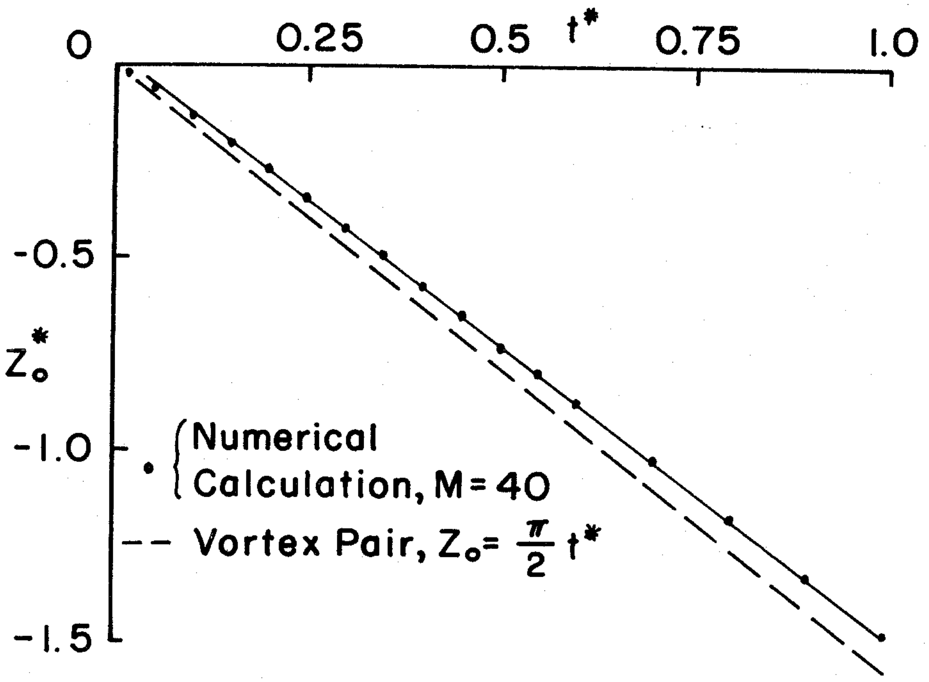

FIG. 7 VERTICAL POSITION OF VORTICITY CENTROID

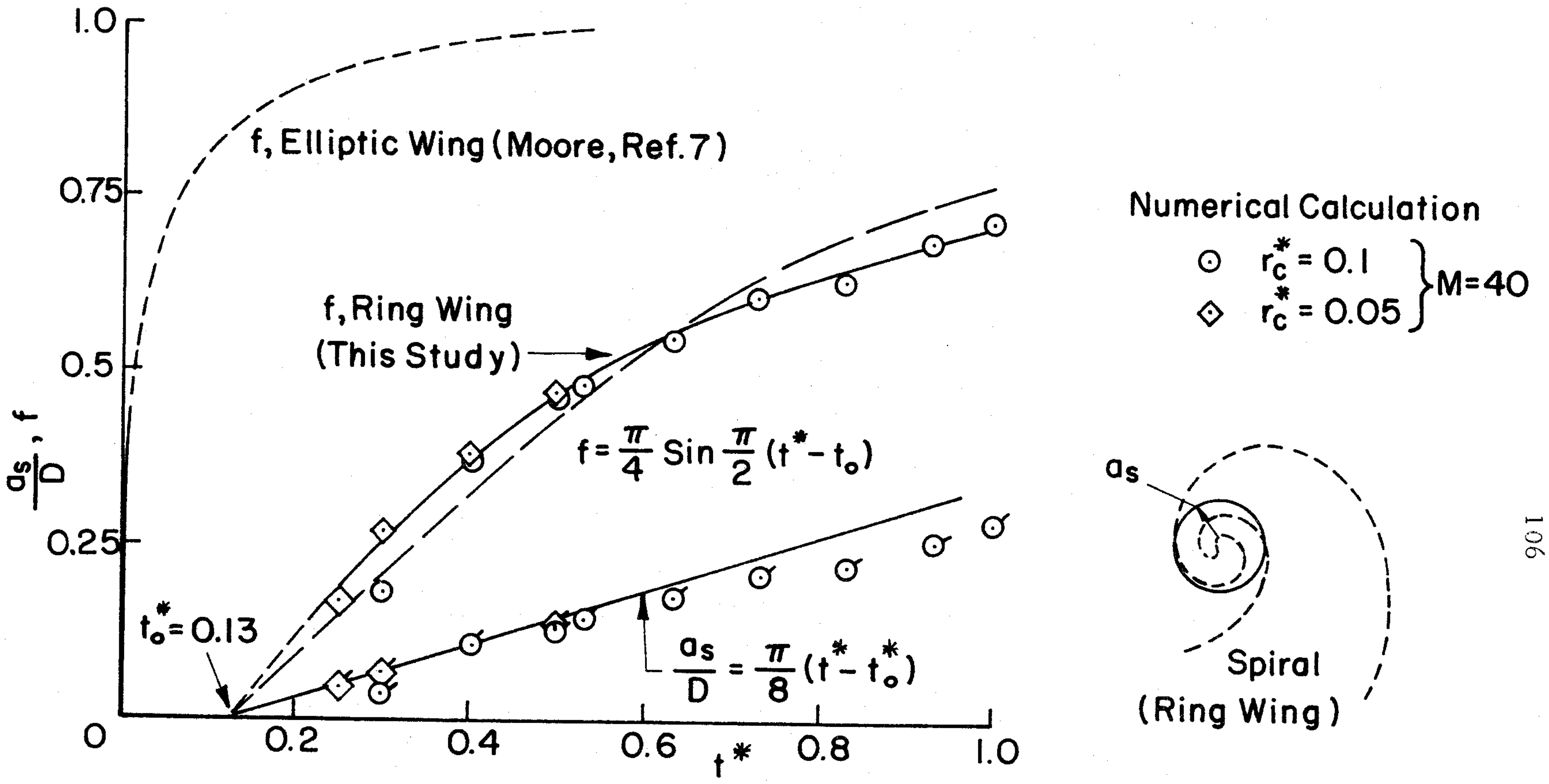

FIG. 8 ROLL-UP RATE OF VORTEX SHEET

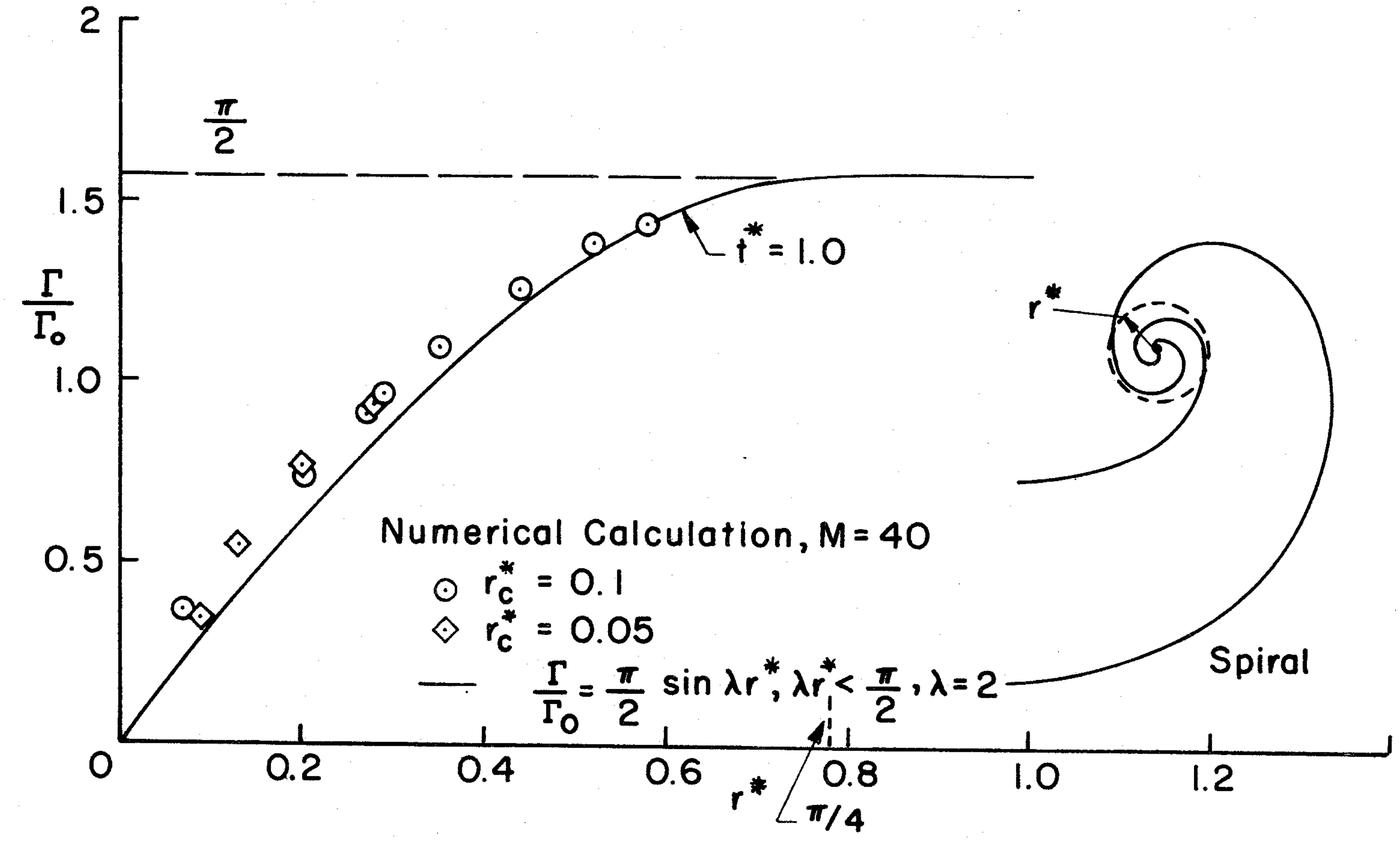

FIG. 9 CIRCULATION DISTRIBUTION IN ROLLED-UP SPIRAL

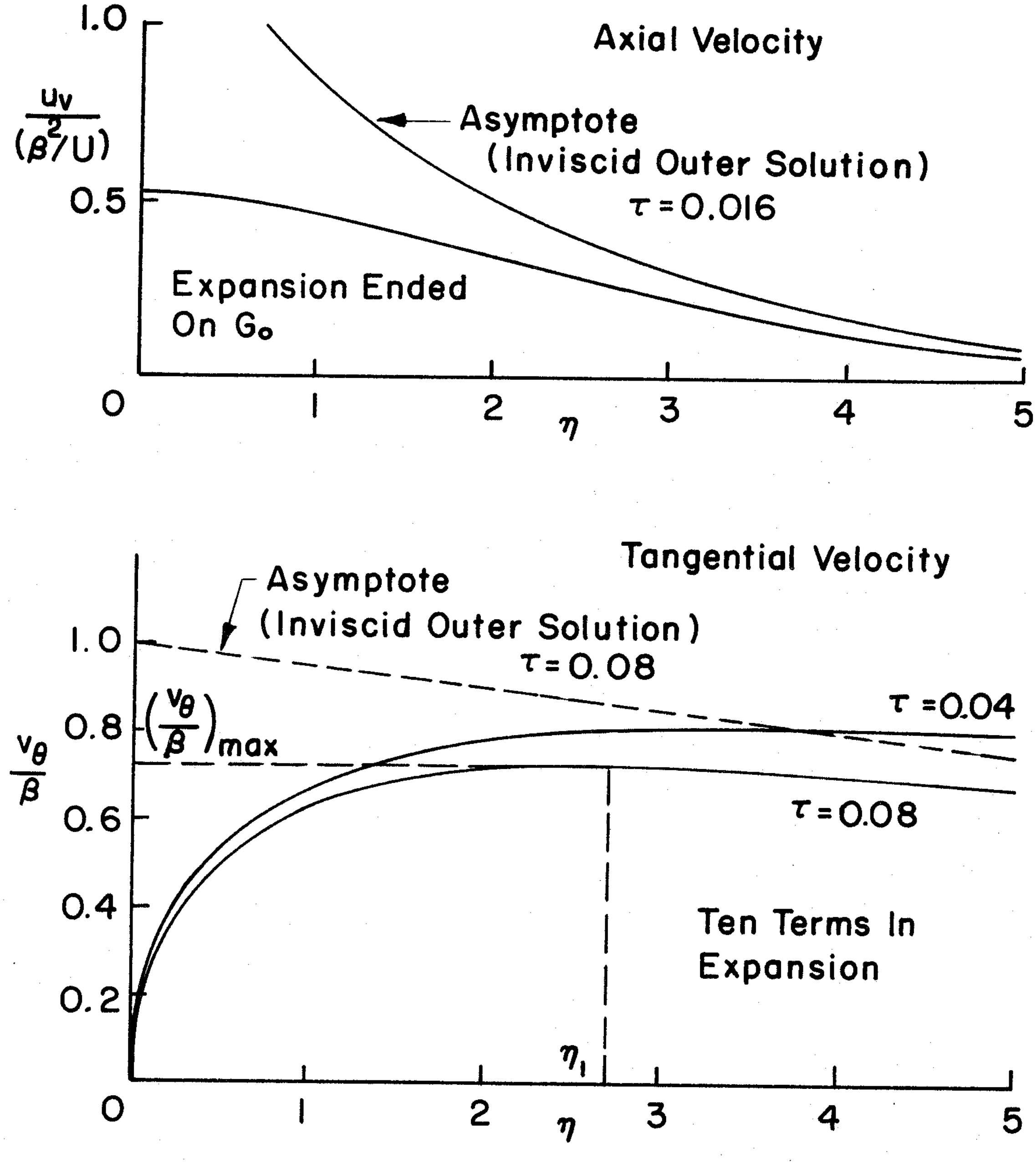

FIG. 10 TANGENTIAL AND AXIAL VELOCITY PROFILES IN VORTEX CORE

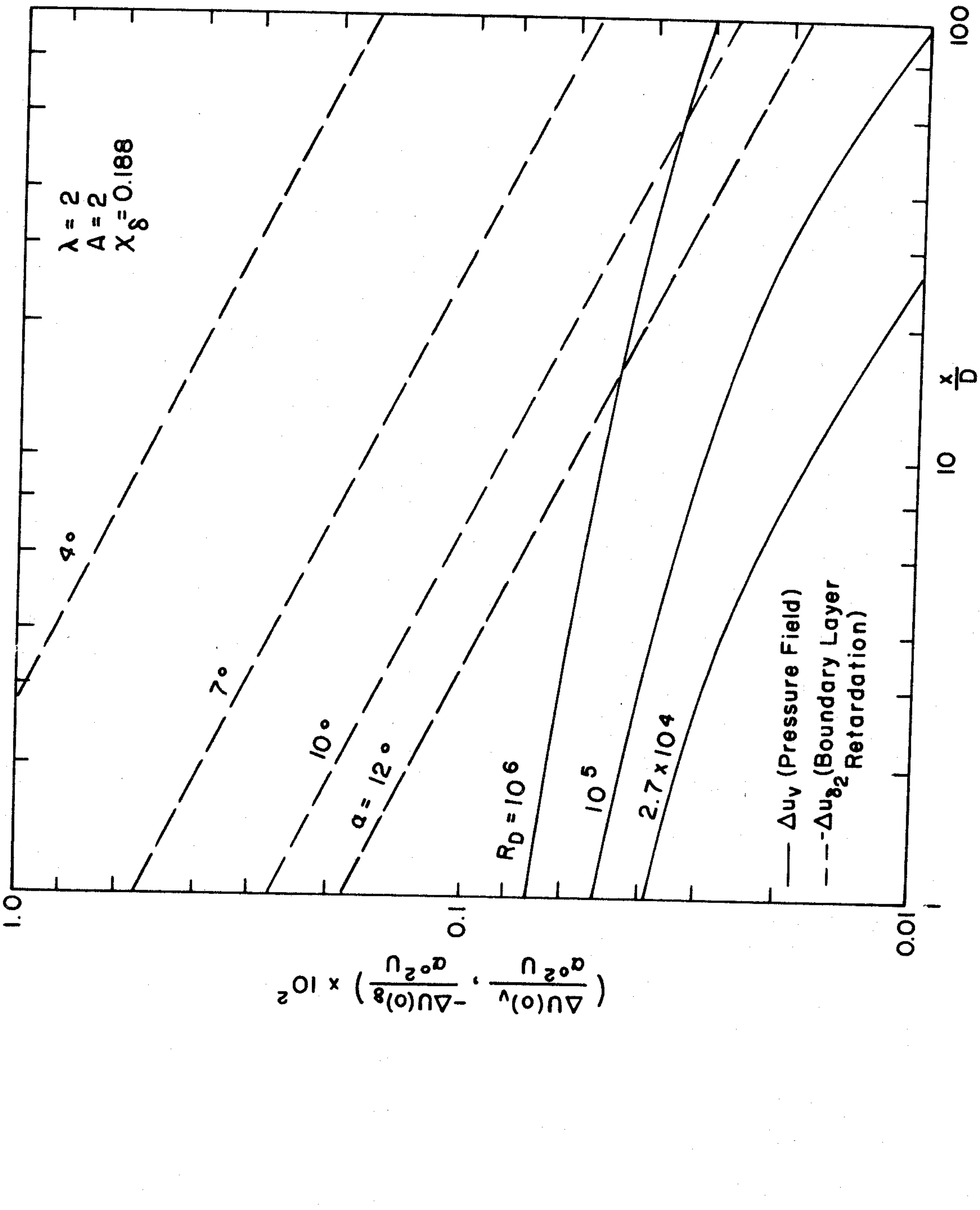

FIG. 11 COMPARISON OF Δu_v AND Δu_δ ON VORTEX AXIS

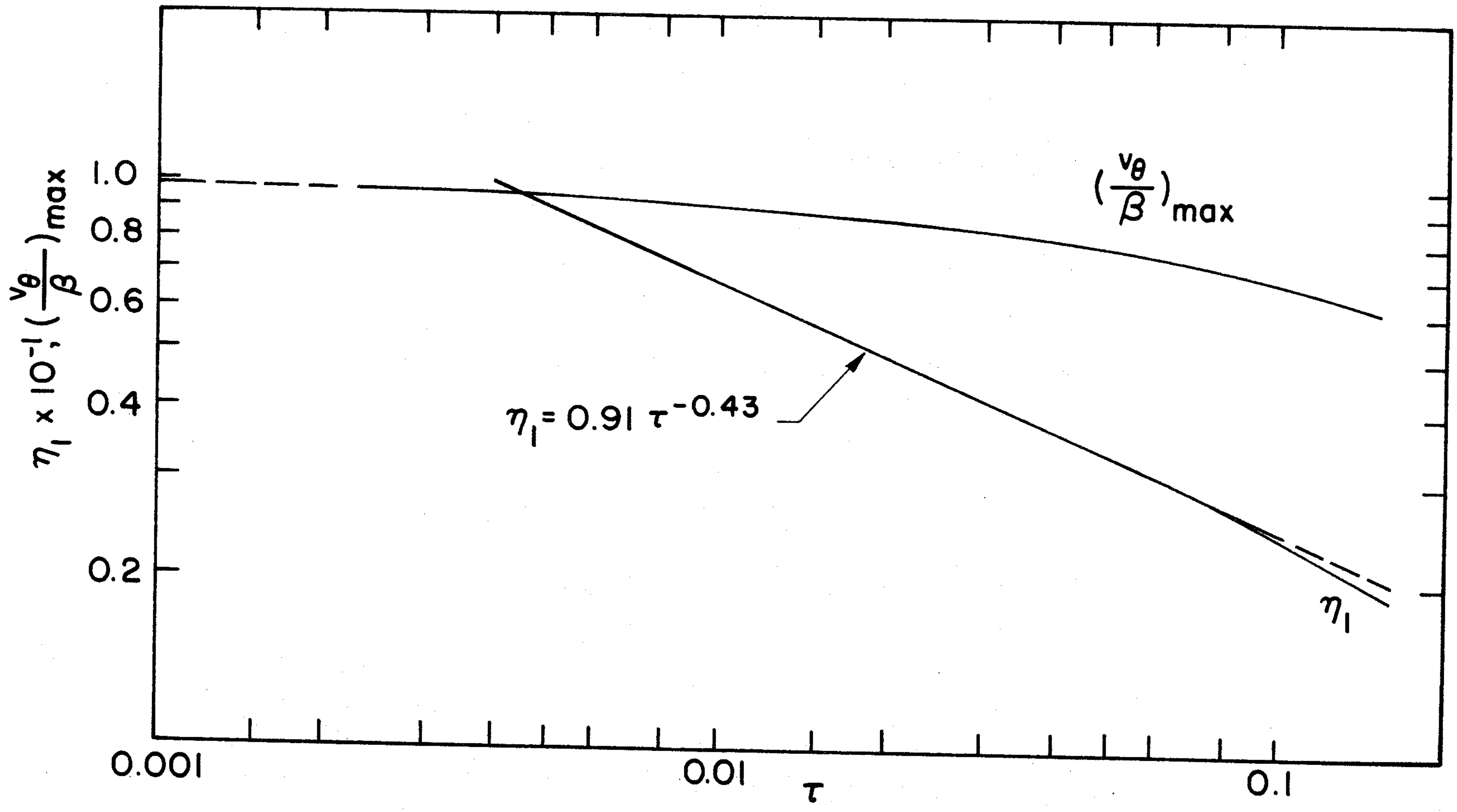

FIG. 12 PEAK TANGENTIAL VELOCITY AND ITS POSITION, η, AS A FUNCTION OF τ

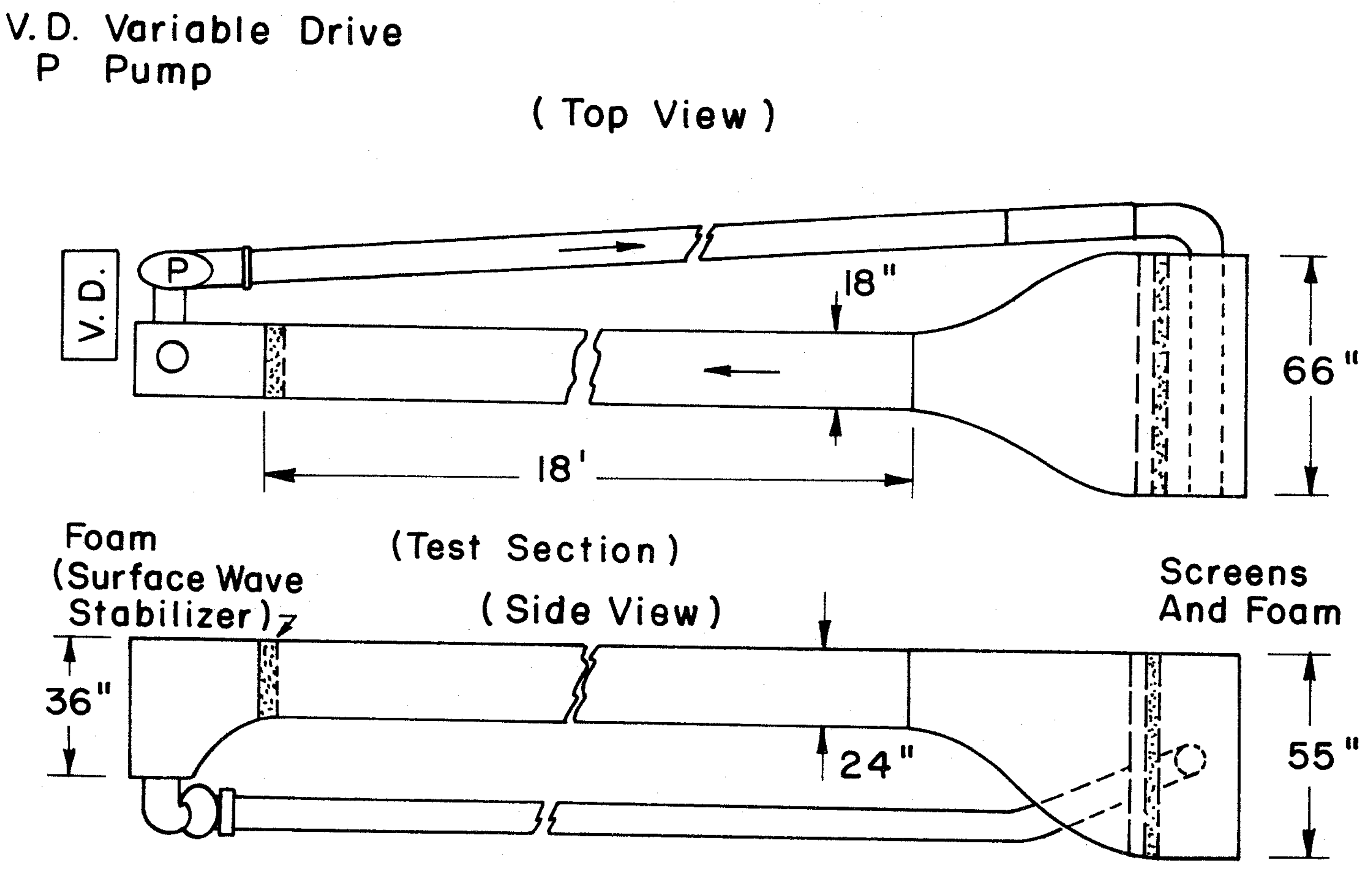

FIG. 13 GALCIT LOW SPEED WATER CHANNEL

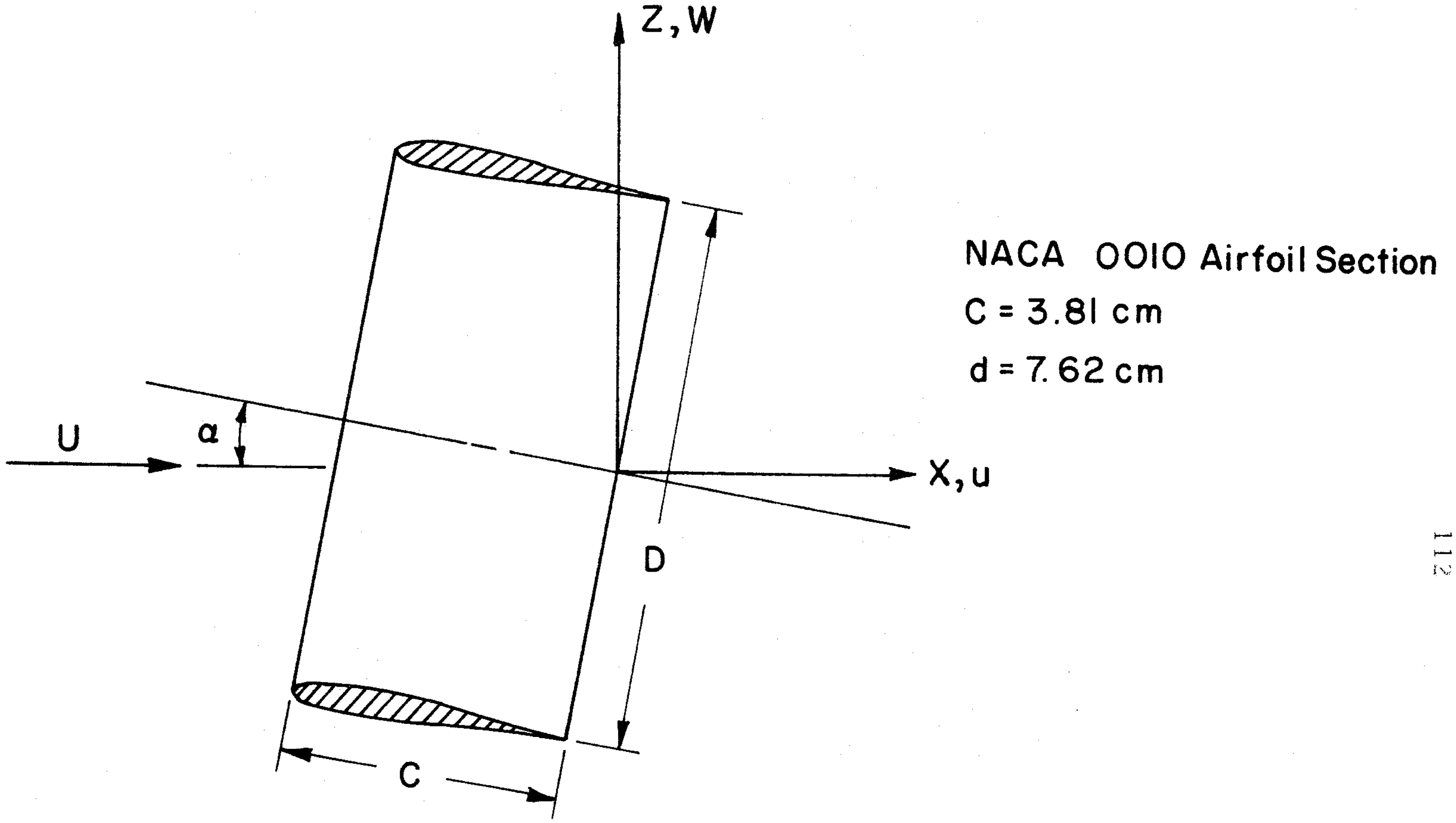

FIG. 14 RING WING TEST MODEL AND COORDINATE SYSTEM

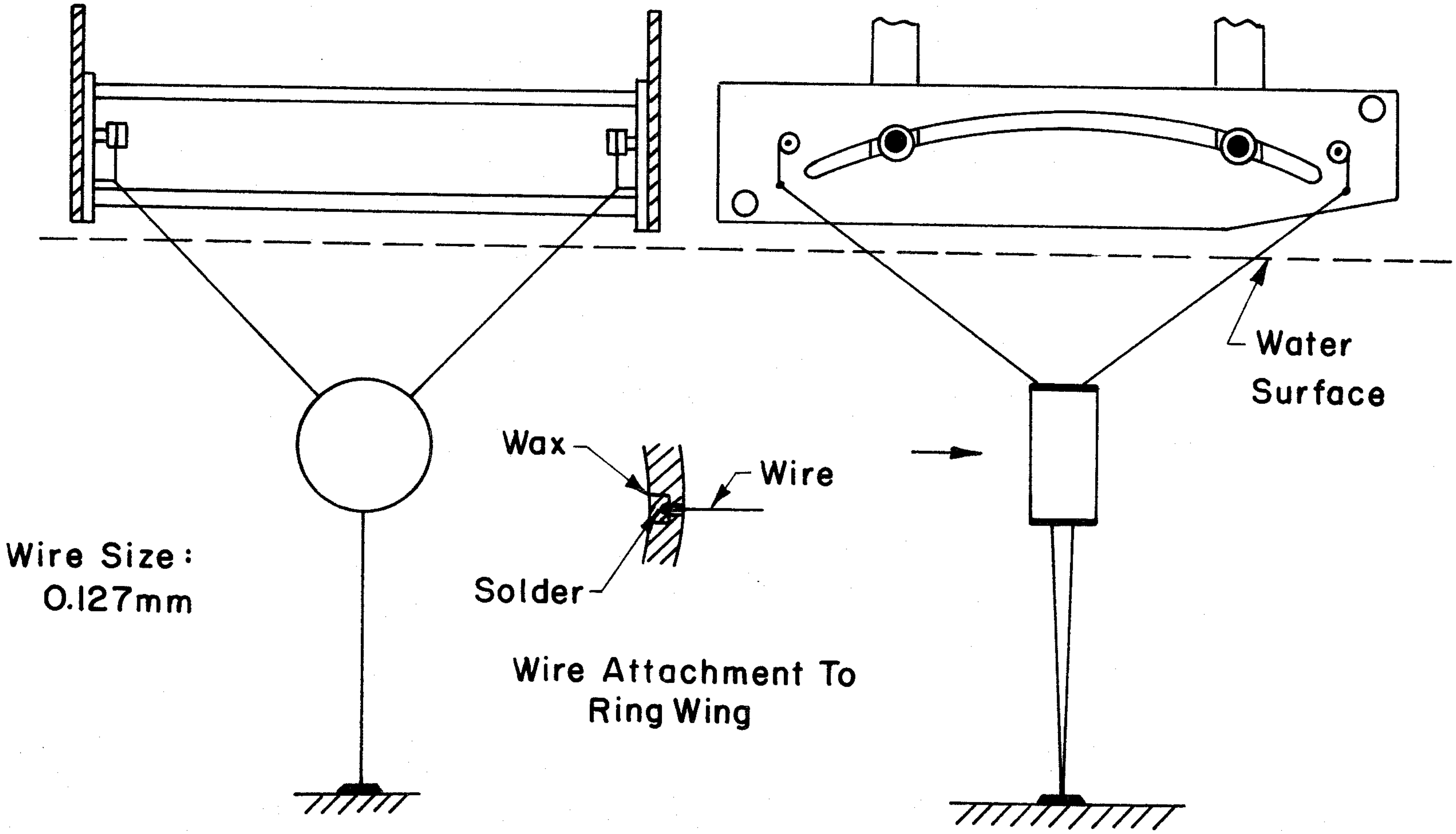

FIG. 15 WIRE SUPPORT MECHANISM (NOT TO SCALE)

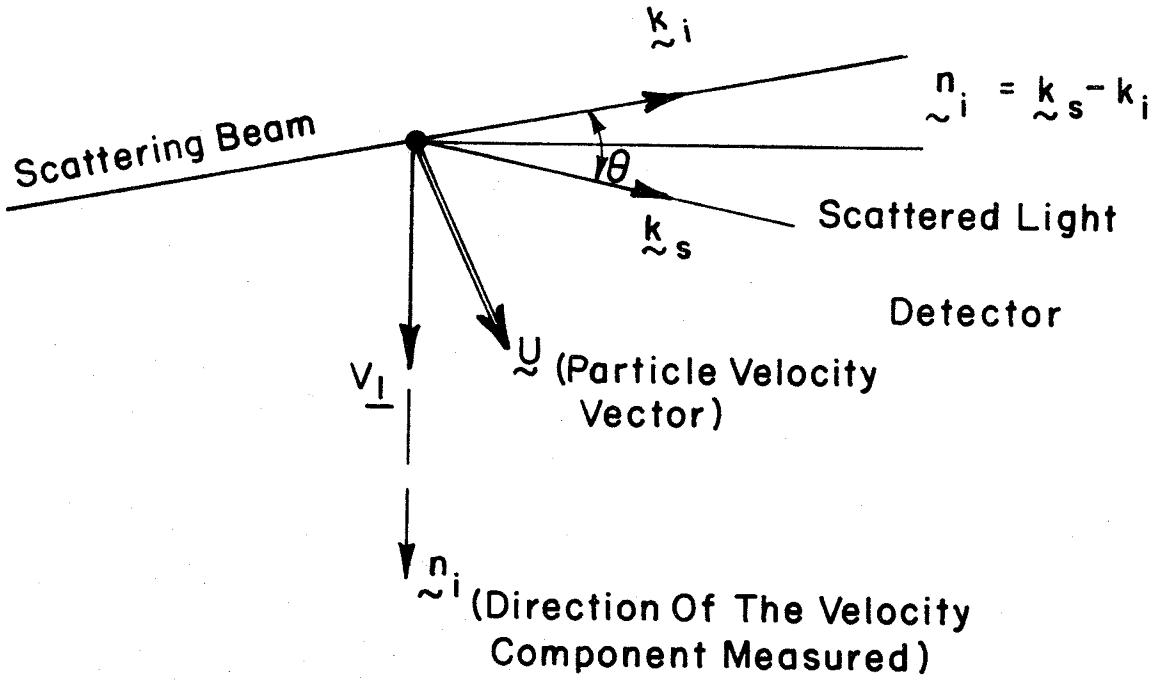

FIG. 16 SCATTERING ANGLE AND PARTICLE VELOCITY VECTOR

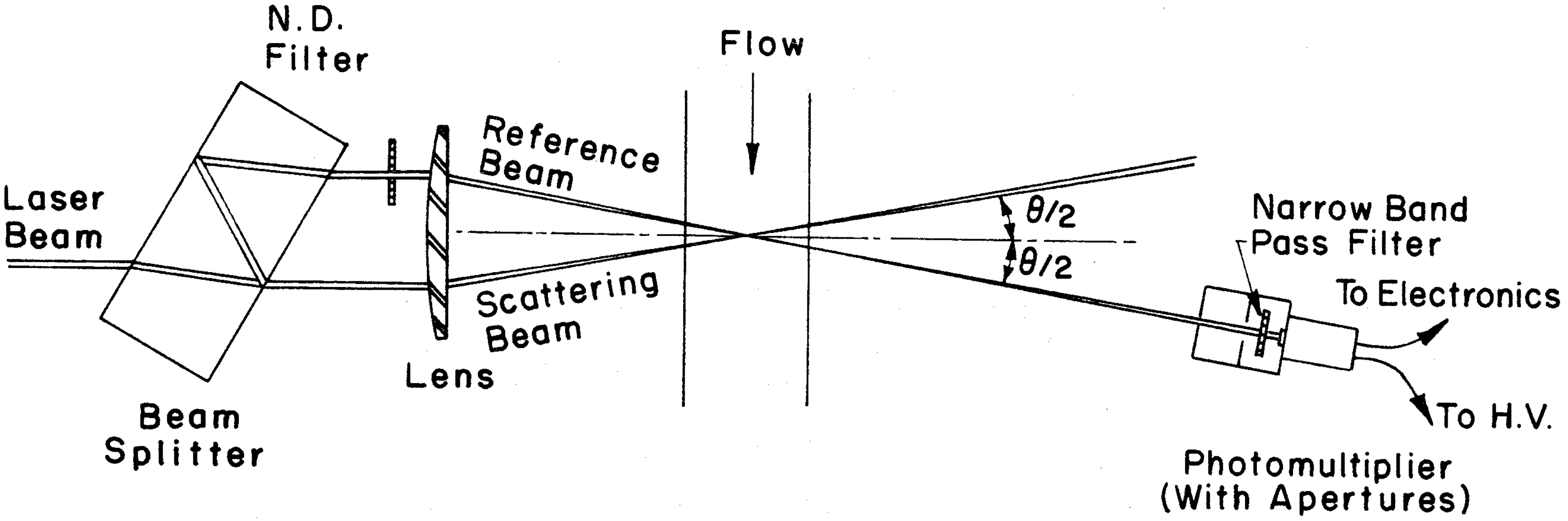

FIG. 17a REFERENCE SCATTER OPTICS

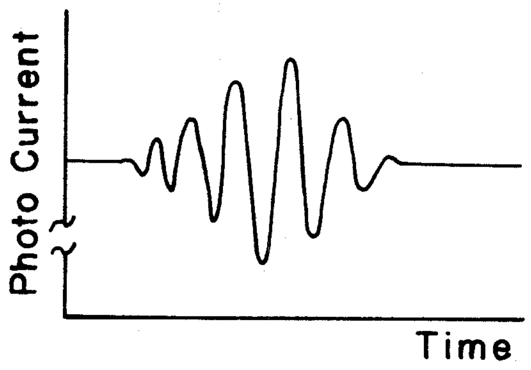

FIG.17b SIGNAL BURST

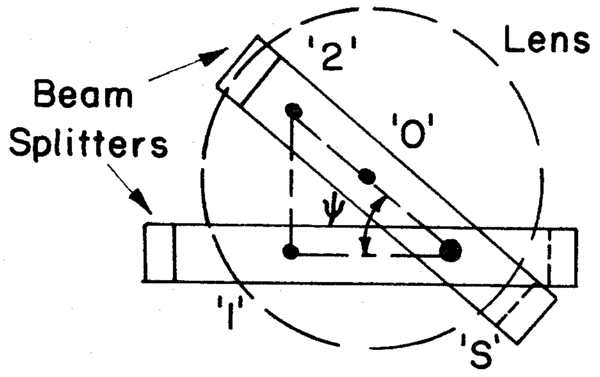

FIG.17c BEAM SPLITTERS
ARRANGEMENT
FOR TWO VELOCITY
COMPONENTS LDV

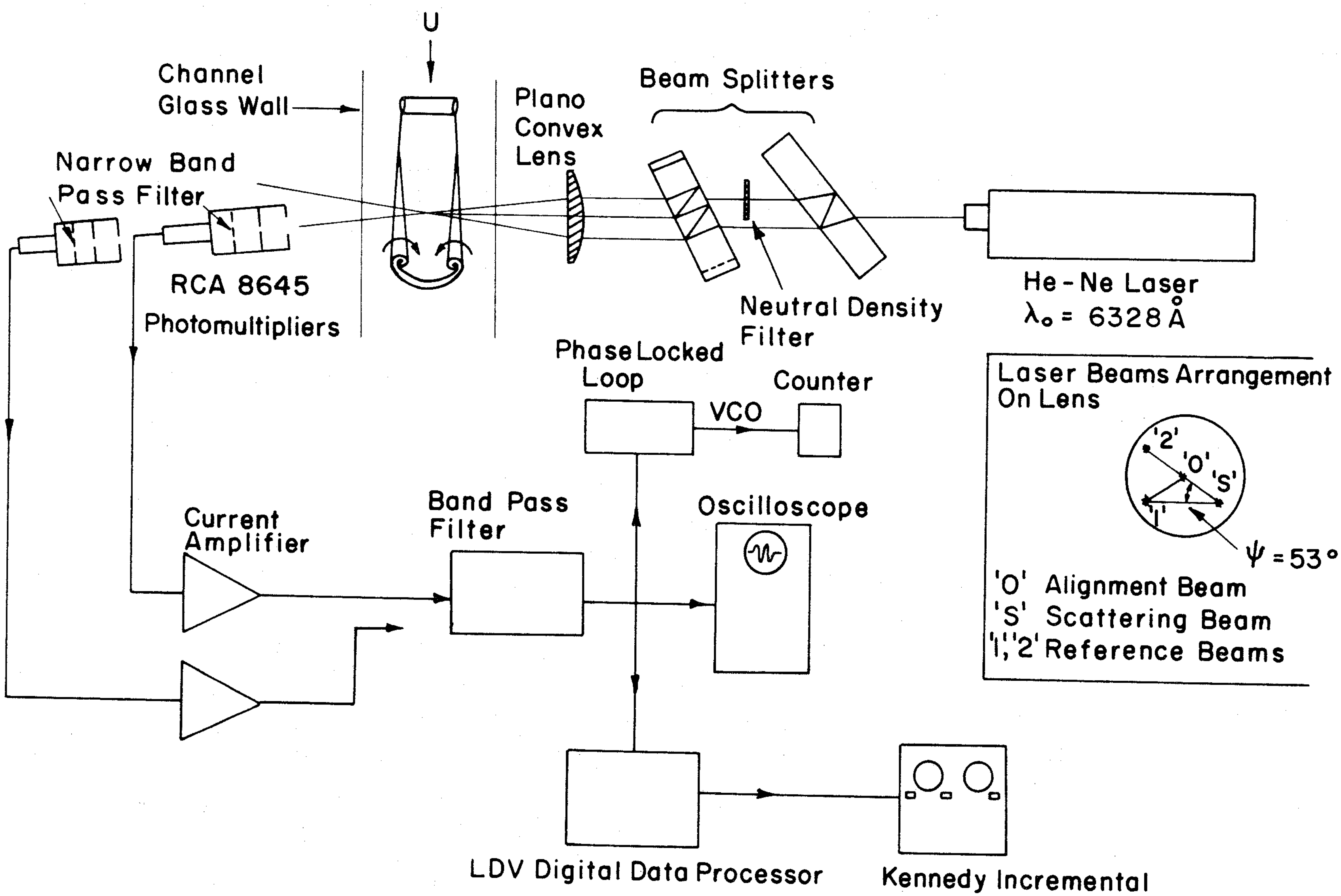

FIG. 18 LDV BLOCK DIAGRAM

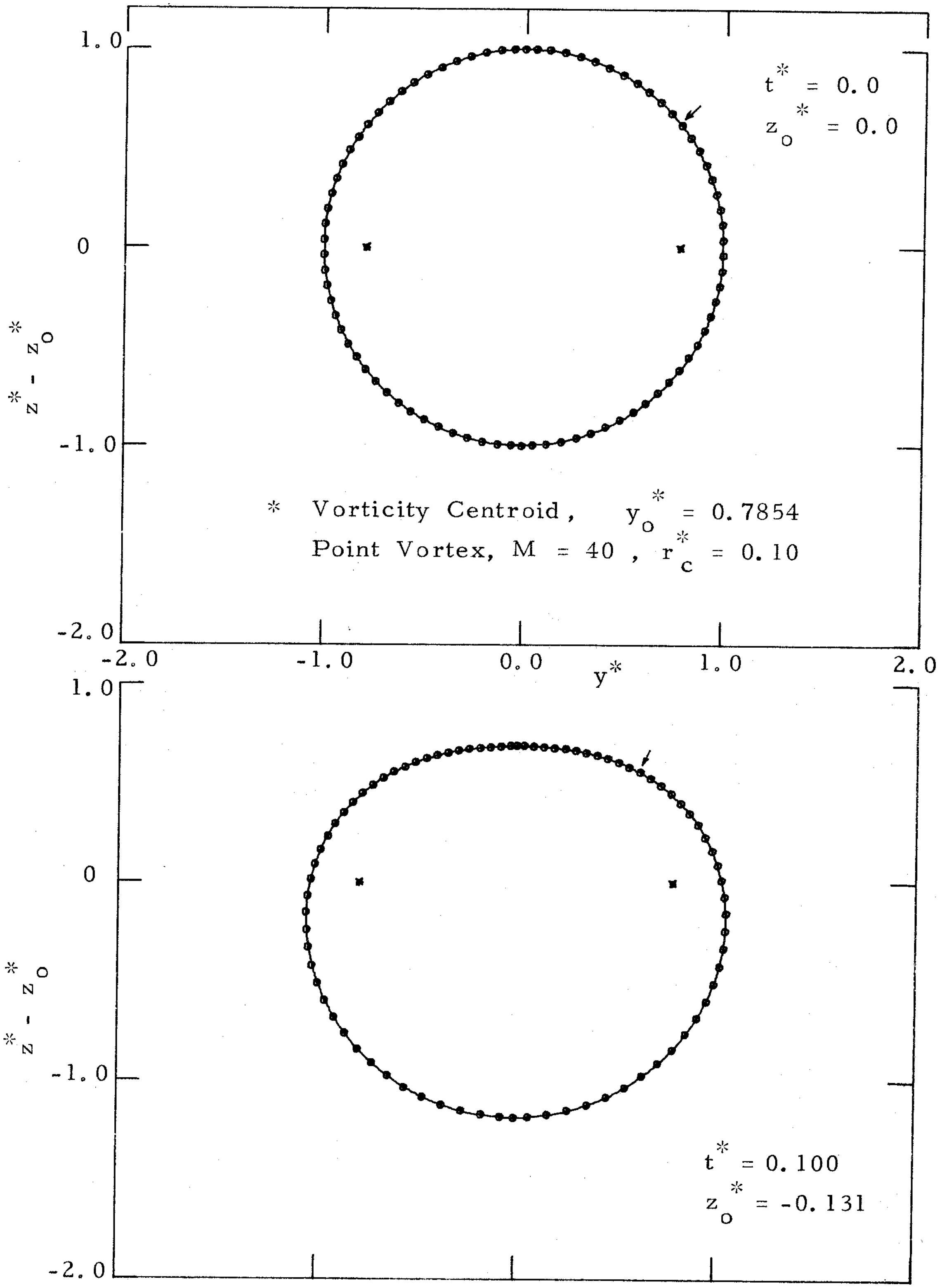

Figure 19a. Point Vortex Approximation to the Roll-up of Vortex Sheet Behind a Ring Wing

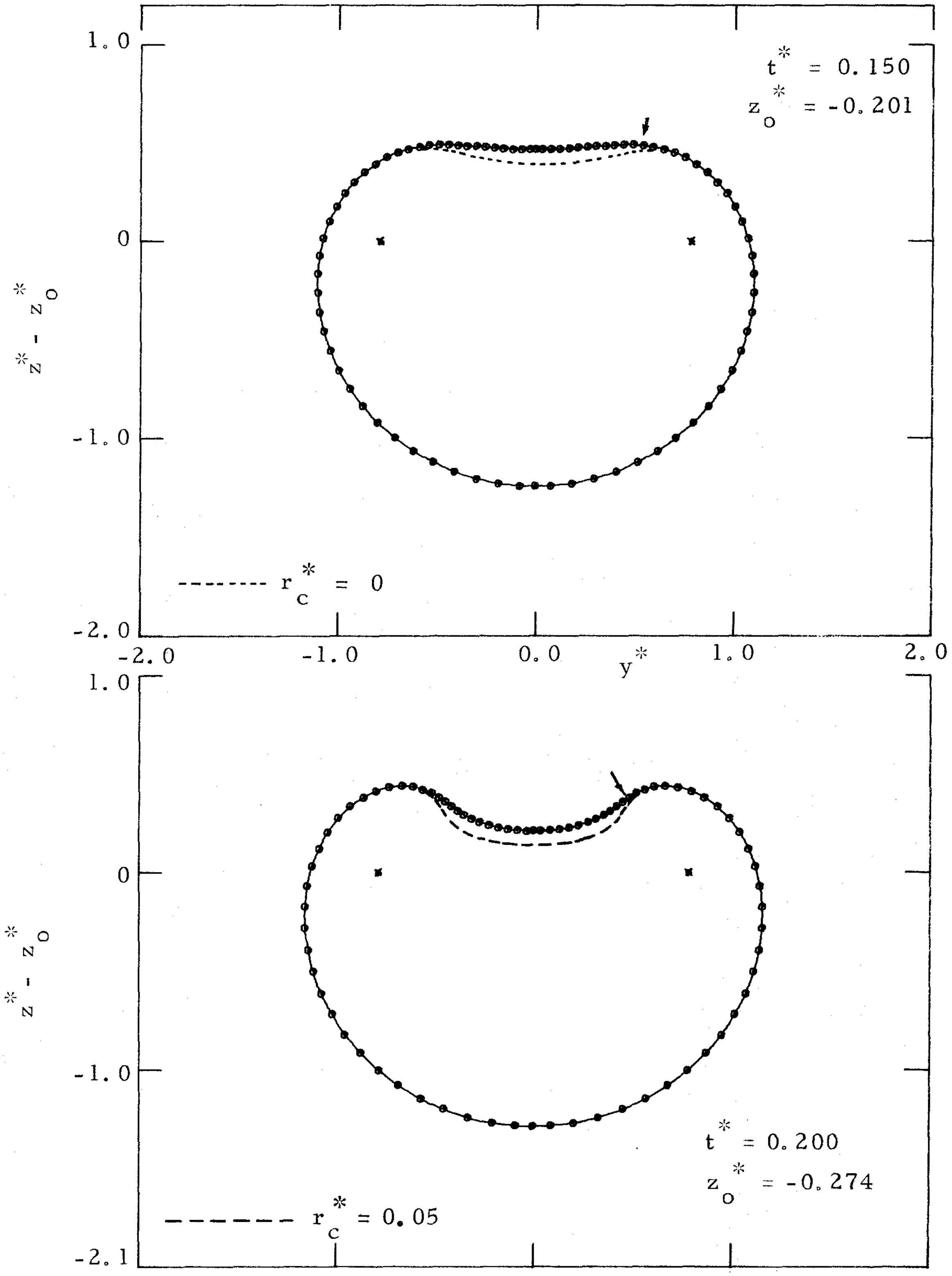

Figure 19b Point Vortex Approximation to the Roll-up of Vortex Sheet Behind a Ring Wing

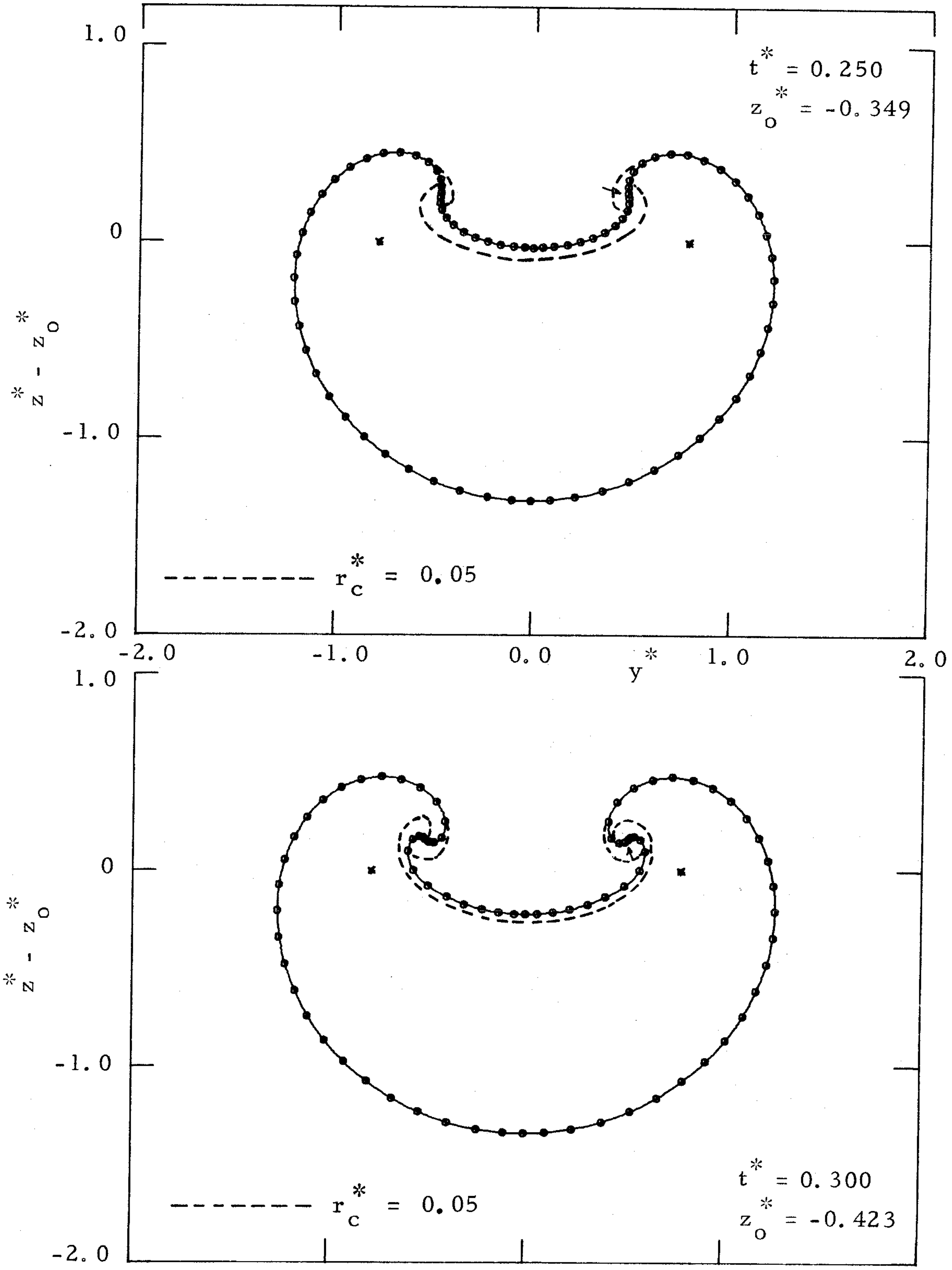

Figure 19c Point Vortex Approximation to the Roll-up of Vortex Sheet Behind a Ring Wing

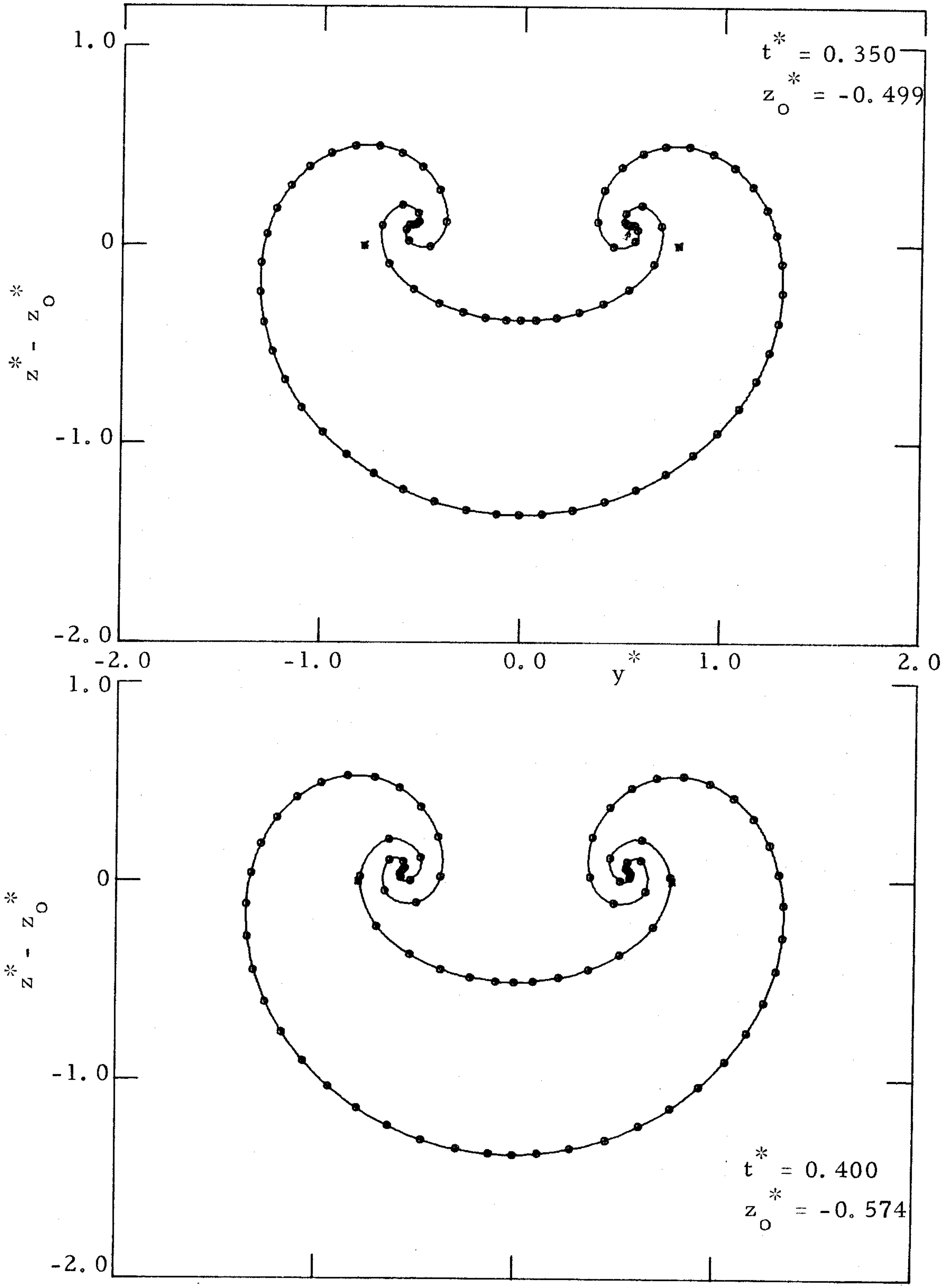

Figure 19d. Point Vortex Approximation to the Roll-up of Vortex Sheet Behind a Ring Wing

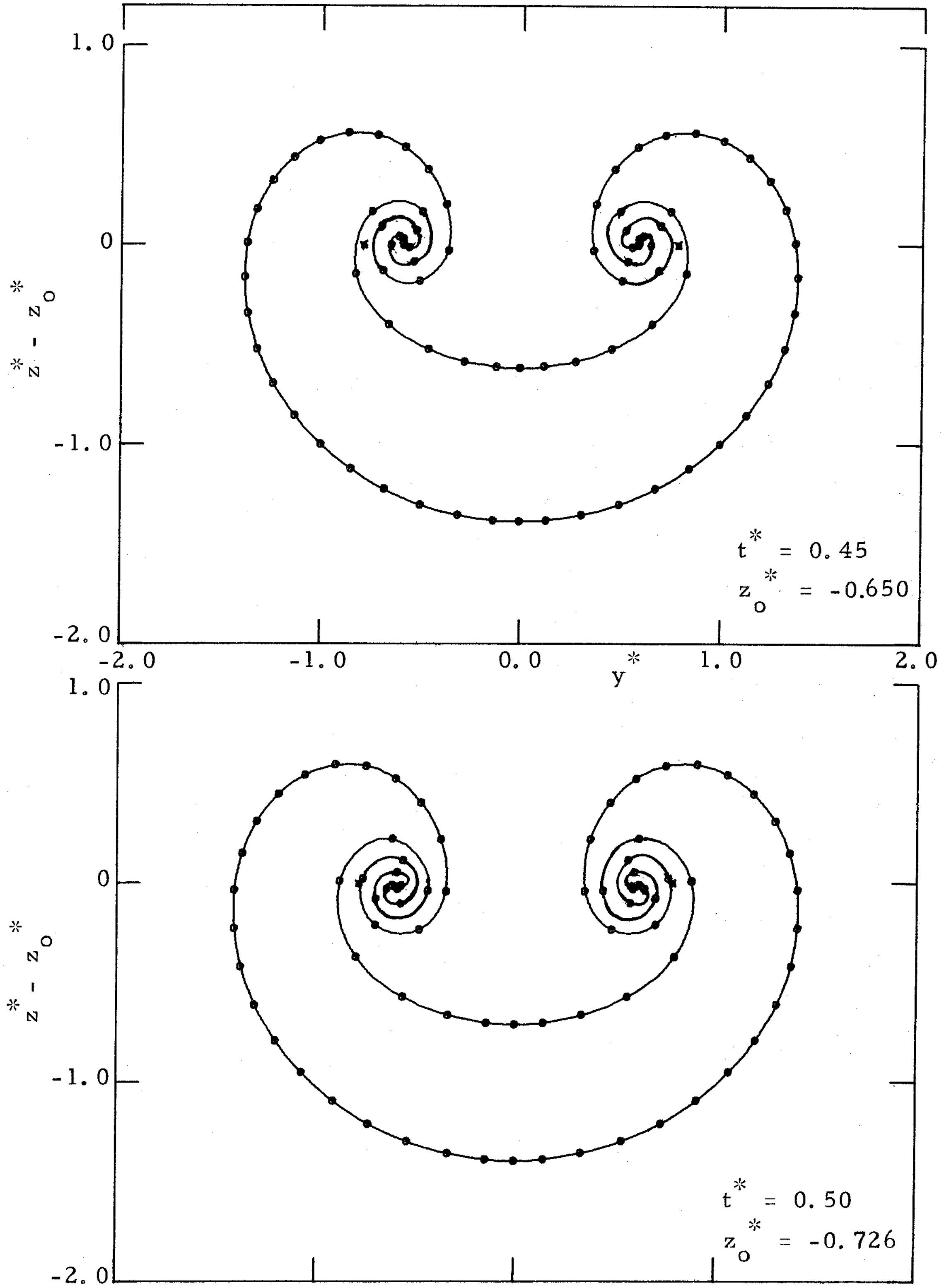

Figure 19e. Point Vortex Approximation to the Roll-up of Vortex Sheet Behind a Ring Wing

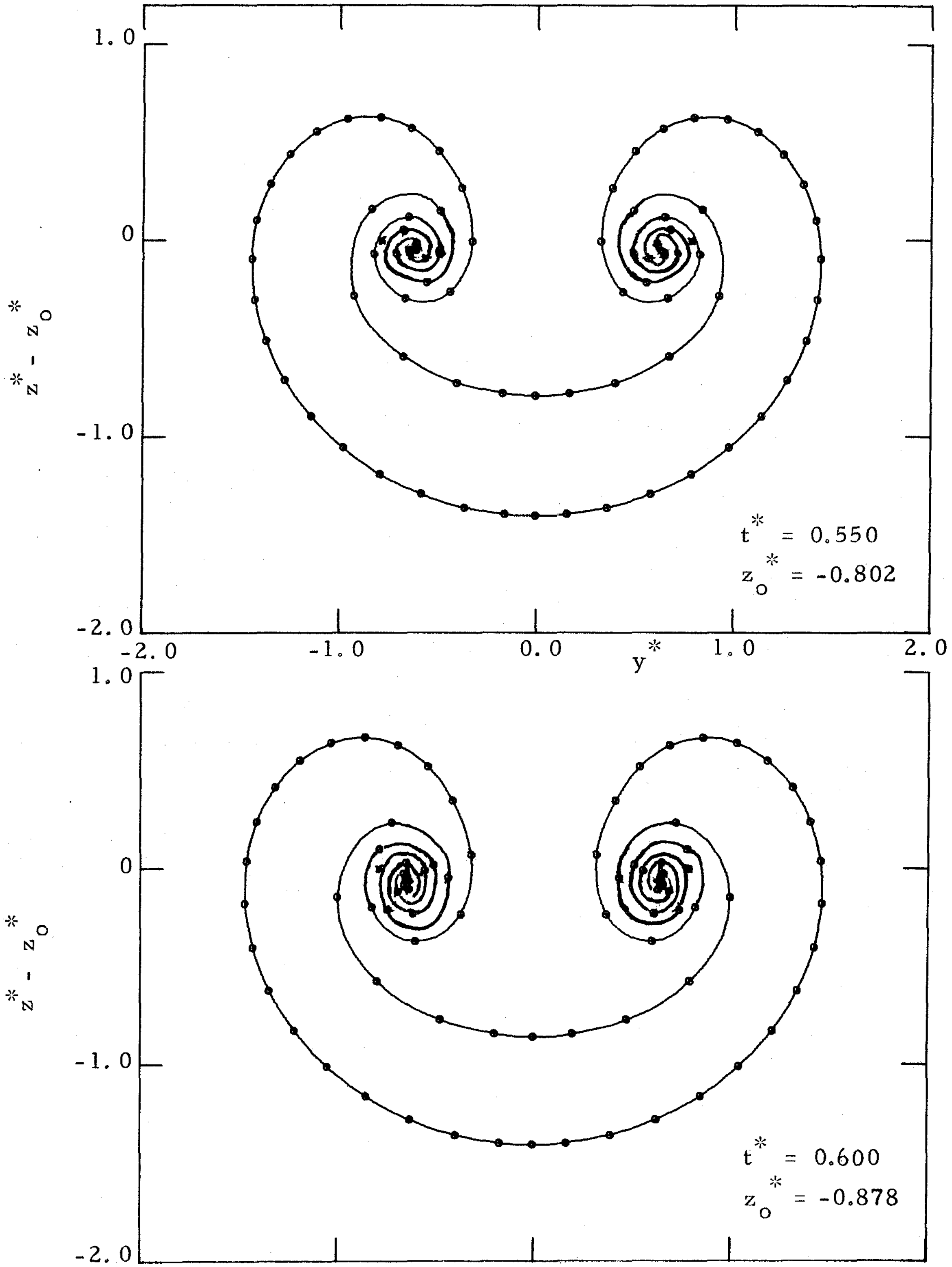

Figure 19f. Point Vortex Approximation to the Roll-up of Vortex Sheet Behind a Ring Wing

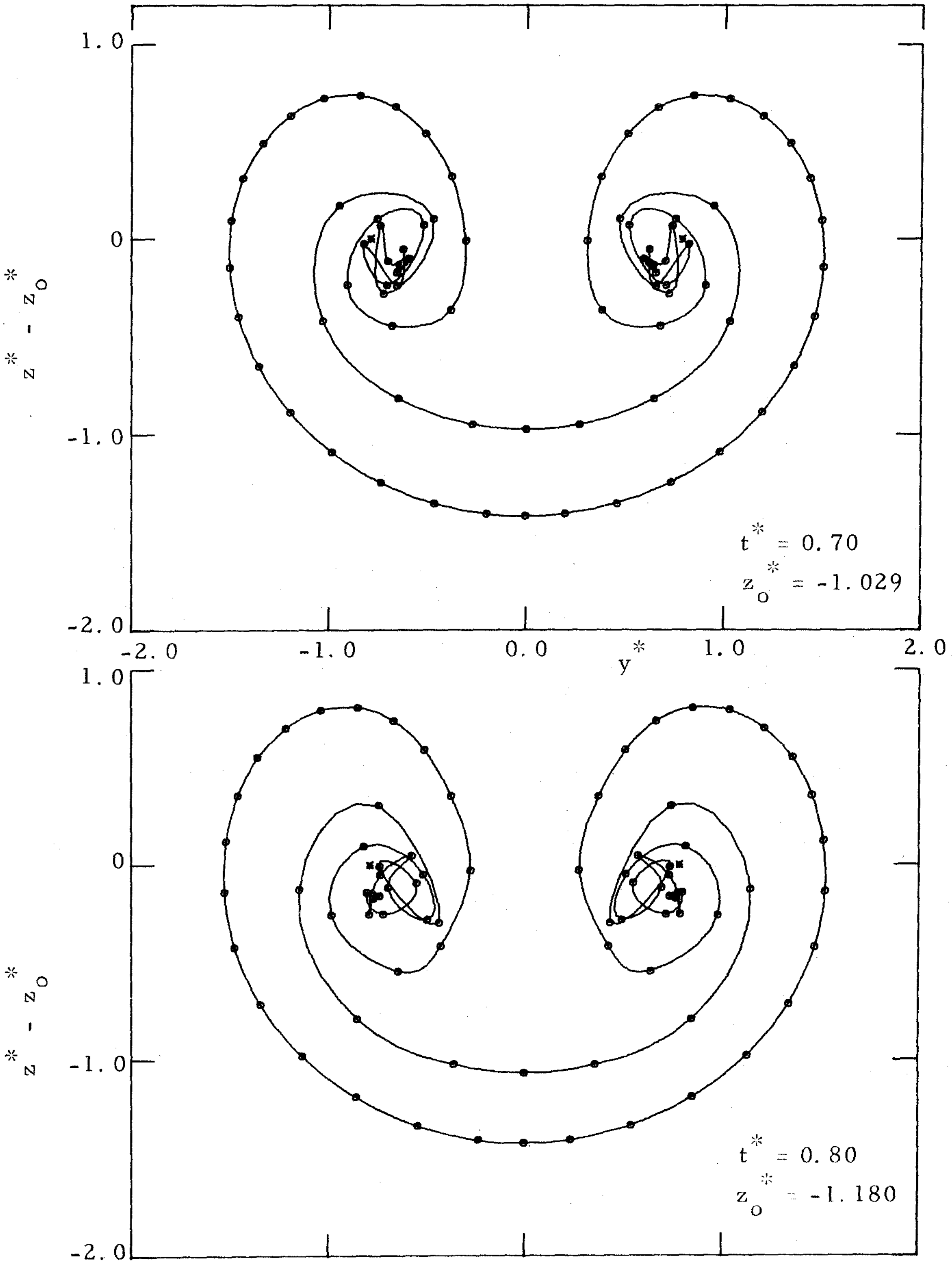

Figure 19g. Point Vortex Approximation to the Roll-up of Vortex Sheet Behind a Ring Wing

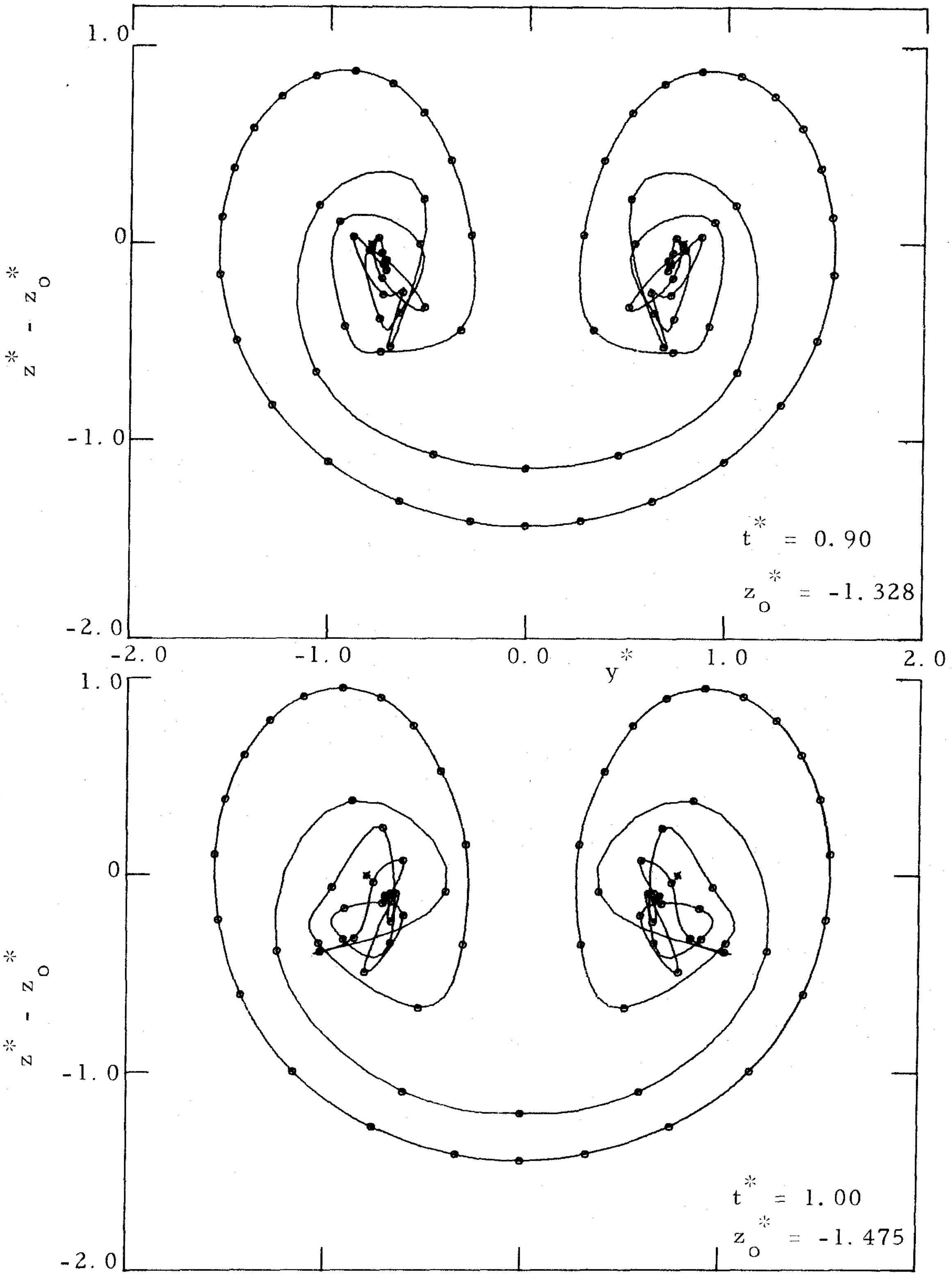

Figure 19h. Point Vortex Approximation to the Roll-up of Vortex Sheet Behind a Ring Wing

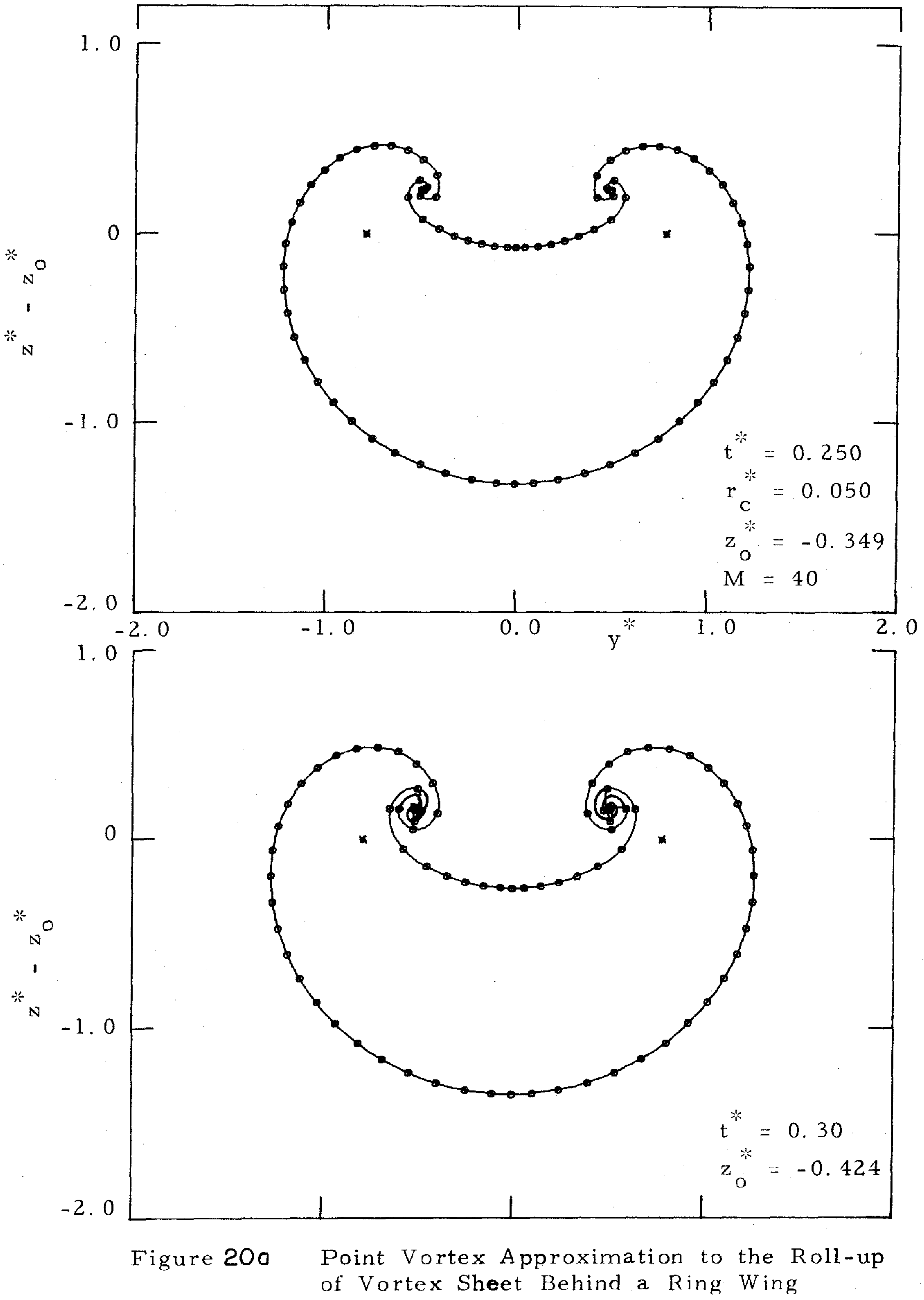

Figure 20a Point Vortex Approximation to the Roll-up of Vortex Sheet Behind a Ring Wing

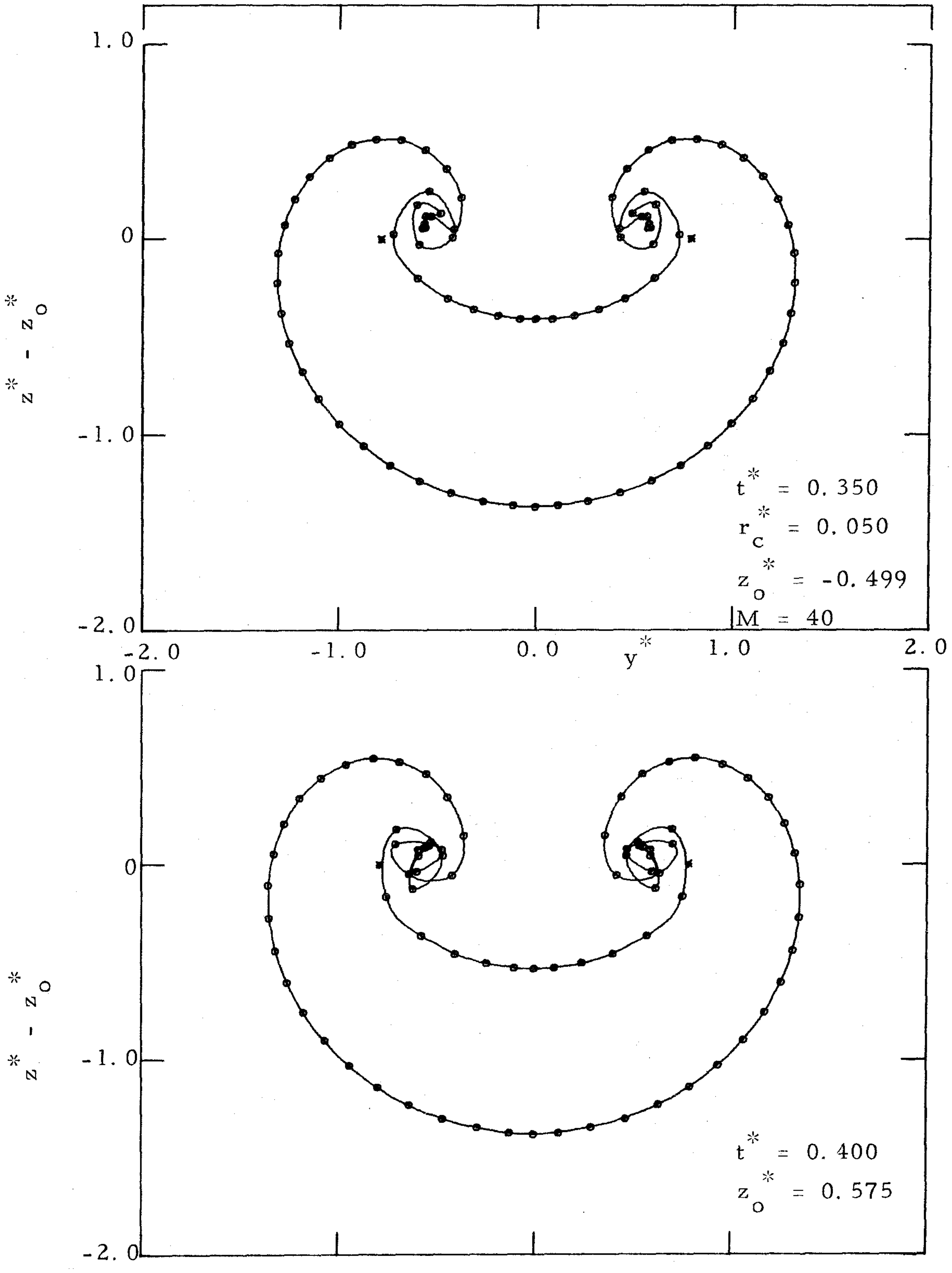

Figure 20b. Point Vortex Approximation to the Roll-up of Vortex Sheet Behind a Ring Wing

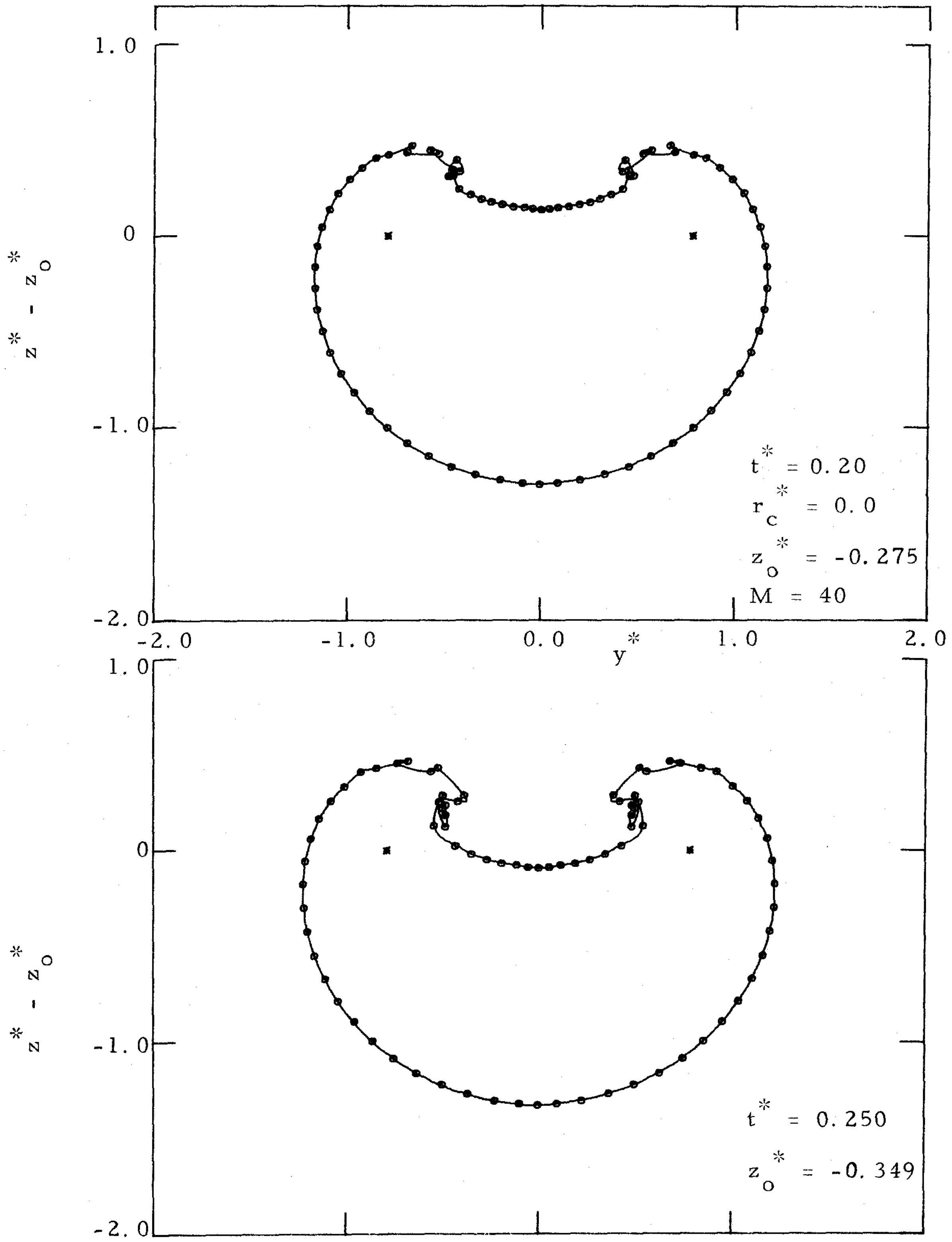

Figure 21. Point Vortex Approximation to the Roll-up of Vortex Sheet Behind a Ring Wing

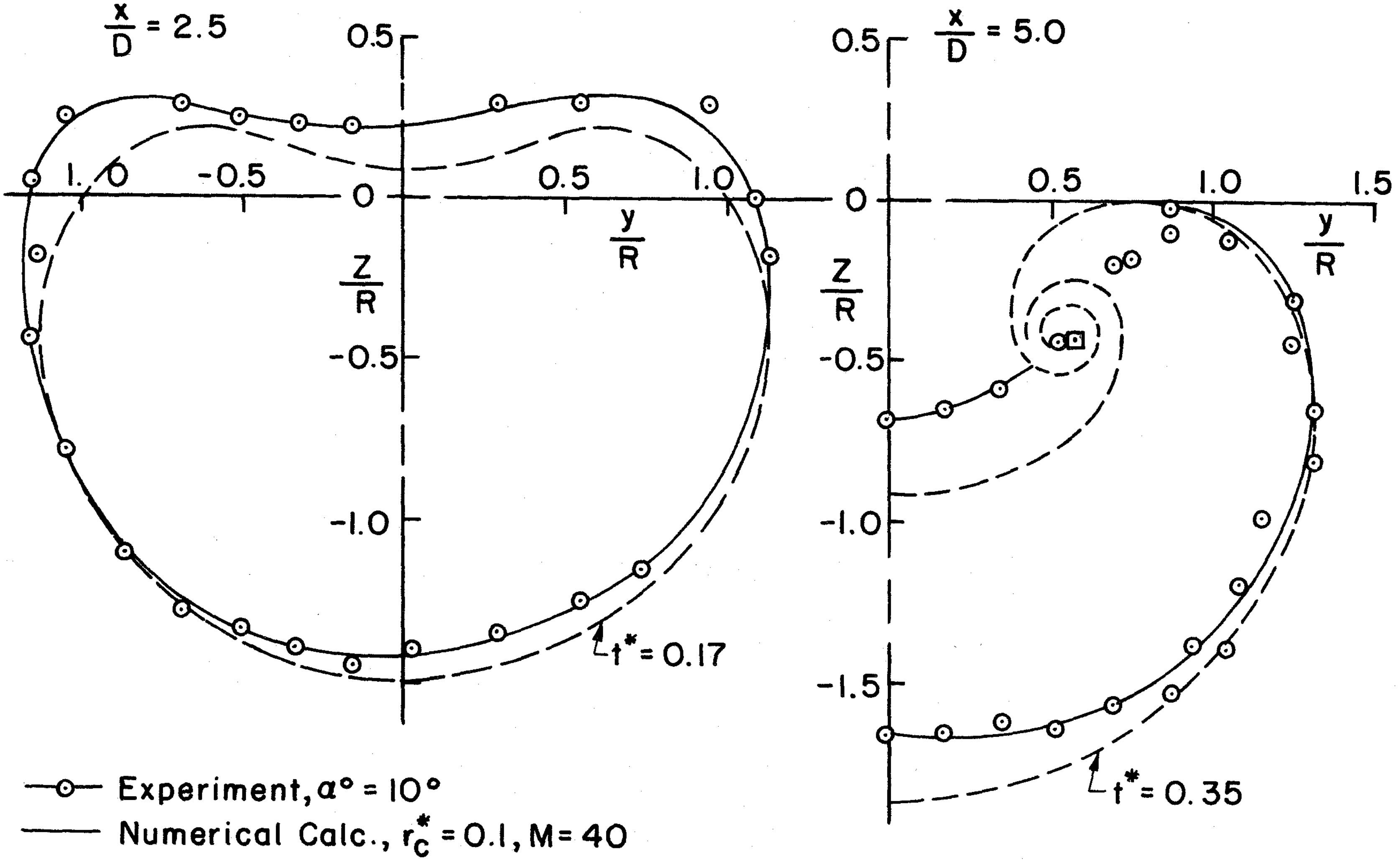

FIG. 22 POSITION OF WAKE BEHIND RING WING

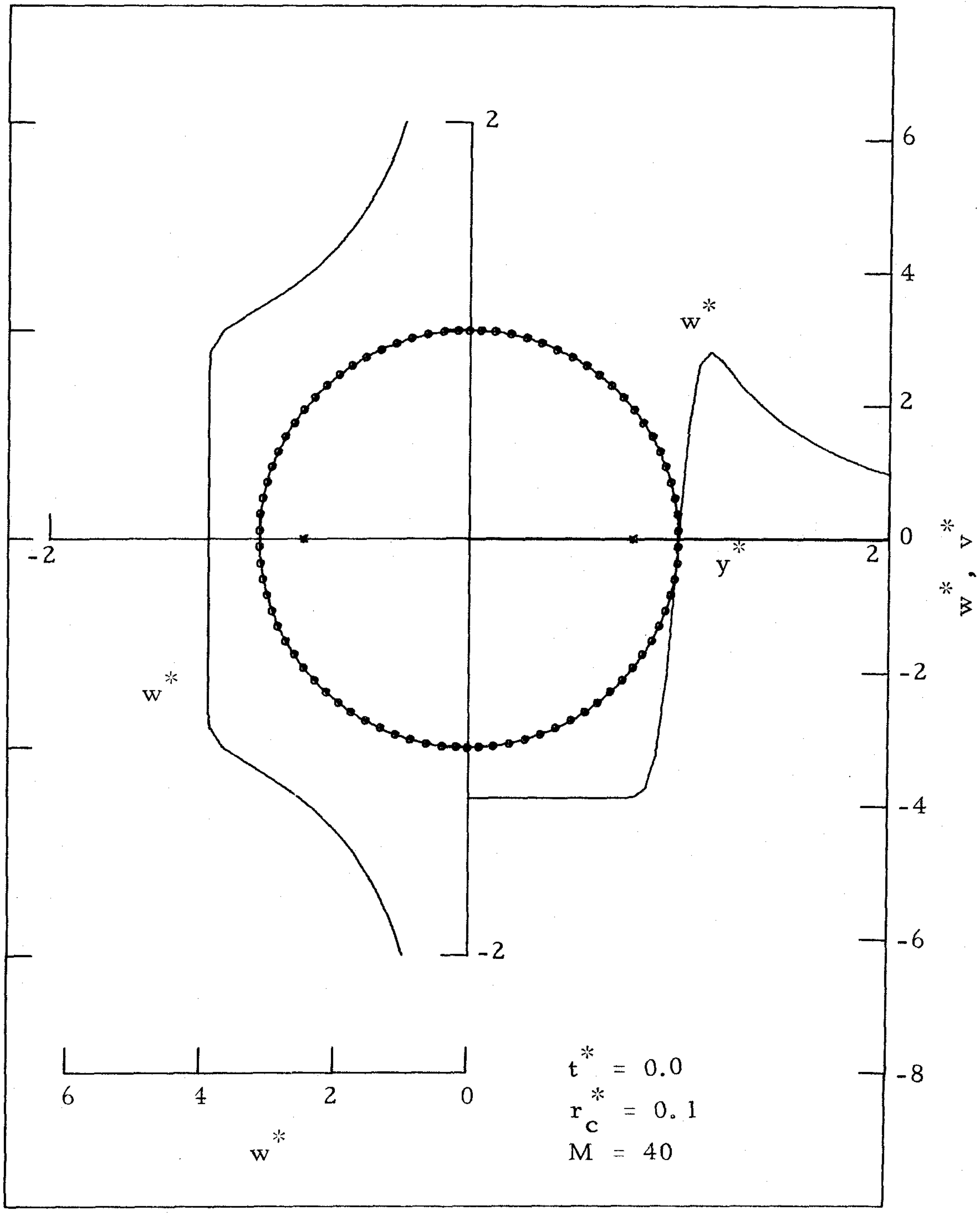

Figure 23a. Numerically Calculated Velocity Profiles in Rolled-up Vortex Sheet

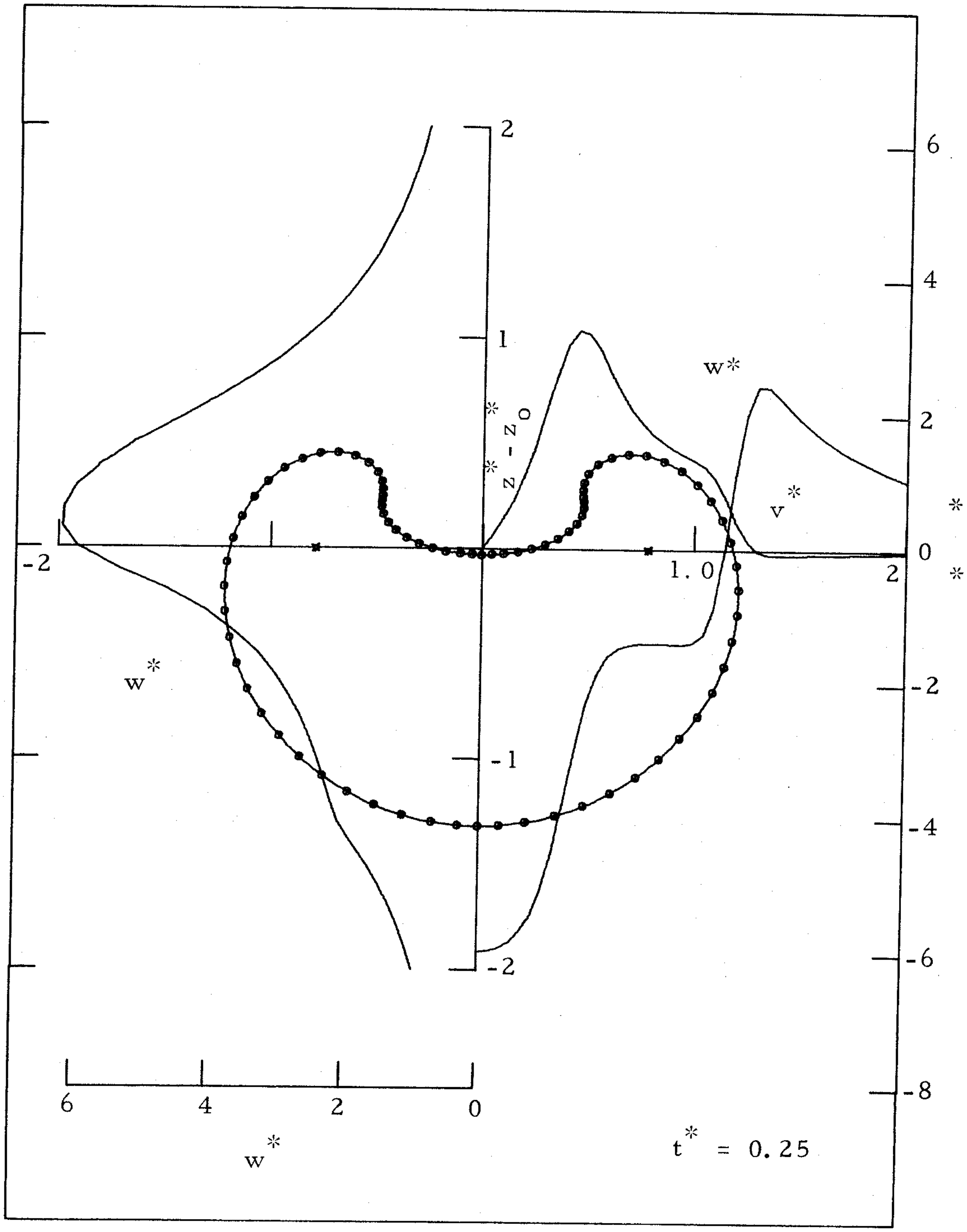

Figure 23c. Numerically Calculated Velocity Profiles in Rolled-up Vortex Sheet

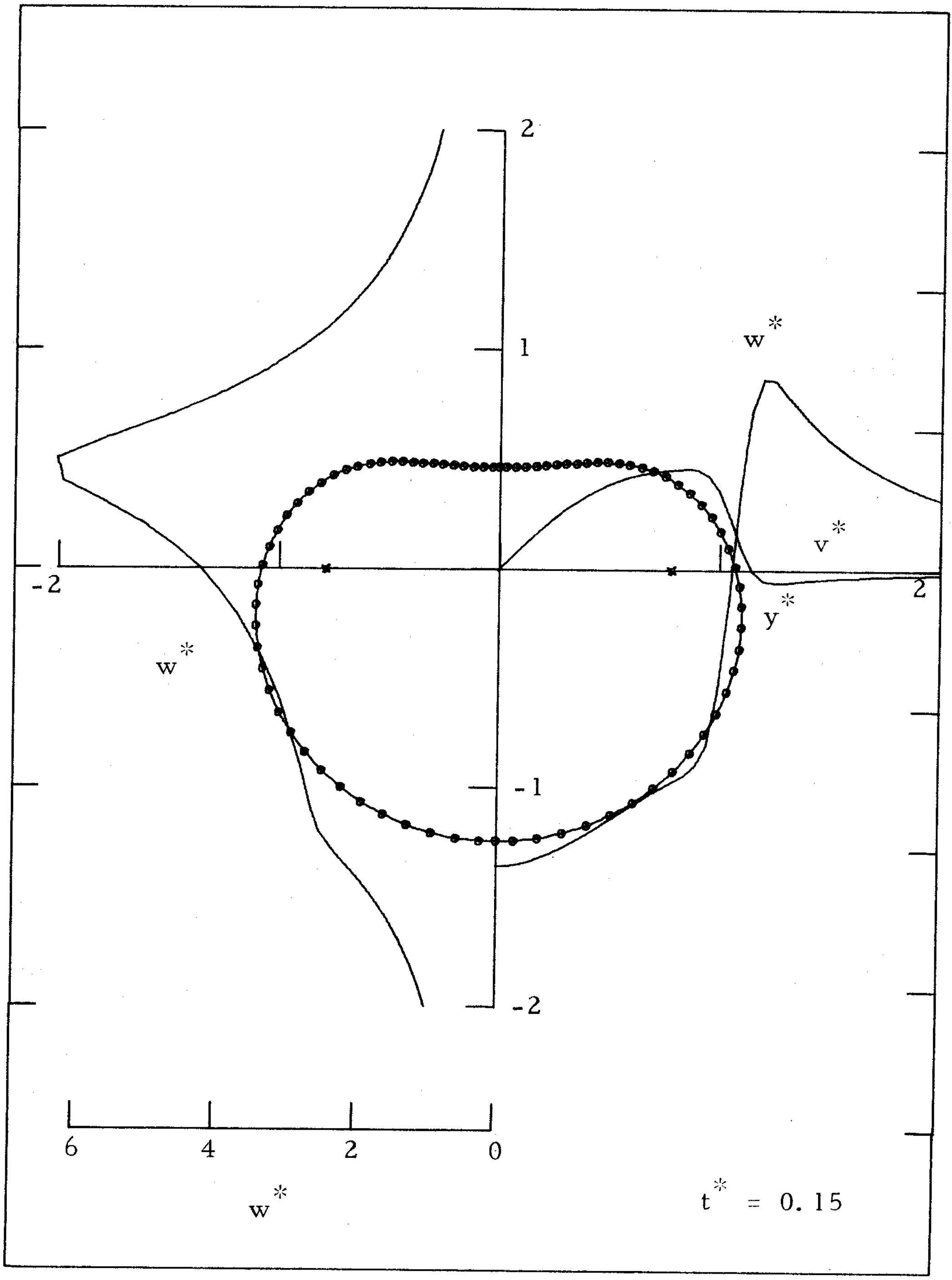

Figure 23b. Numerically Calculated Velocity Profiles in Rolled-up Vortex Sheet

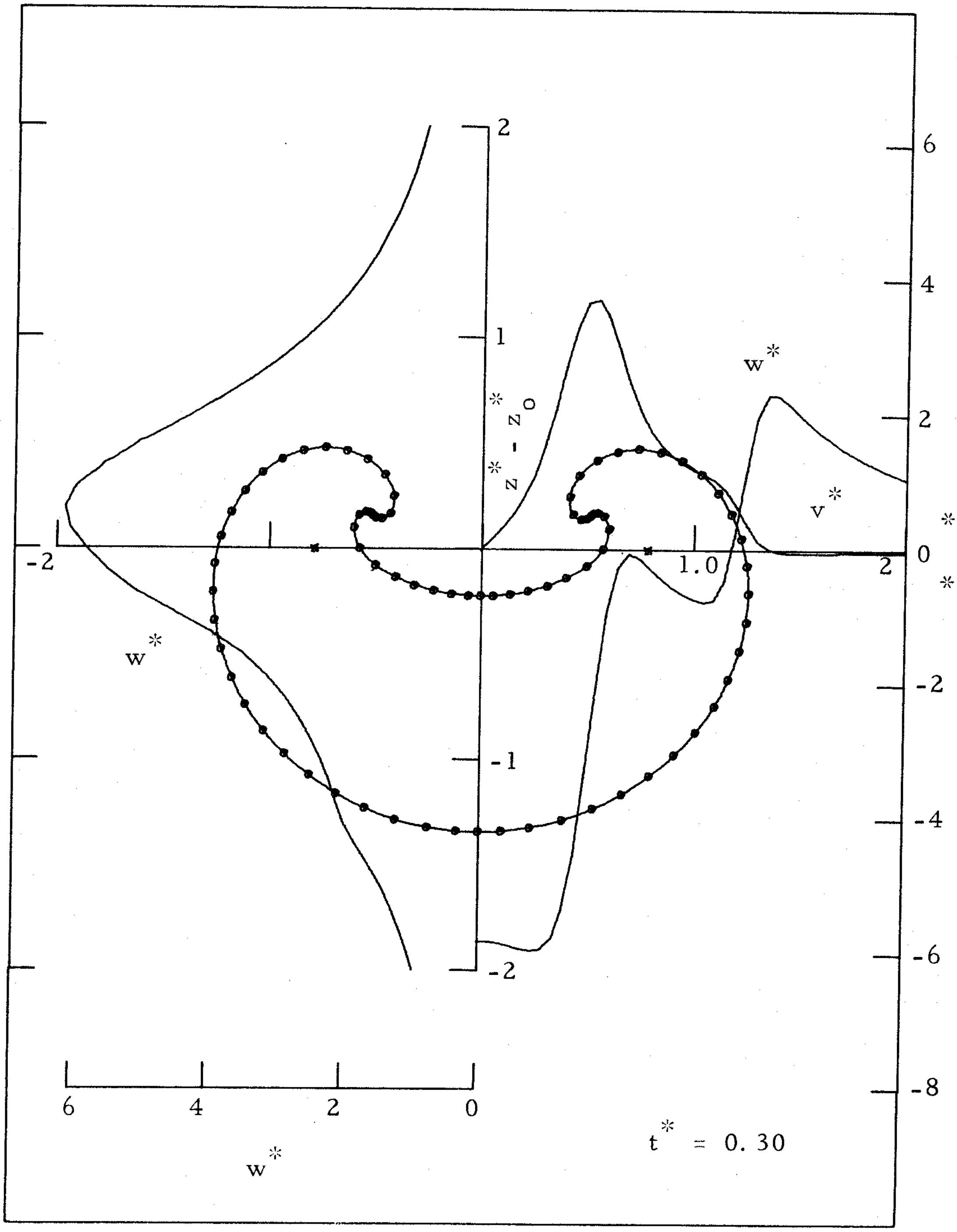

Figure 23d. Numerically Calculated Velocity Profiles in Rolled-up Vortex Sheet

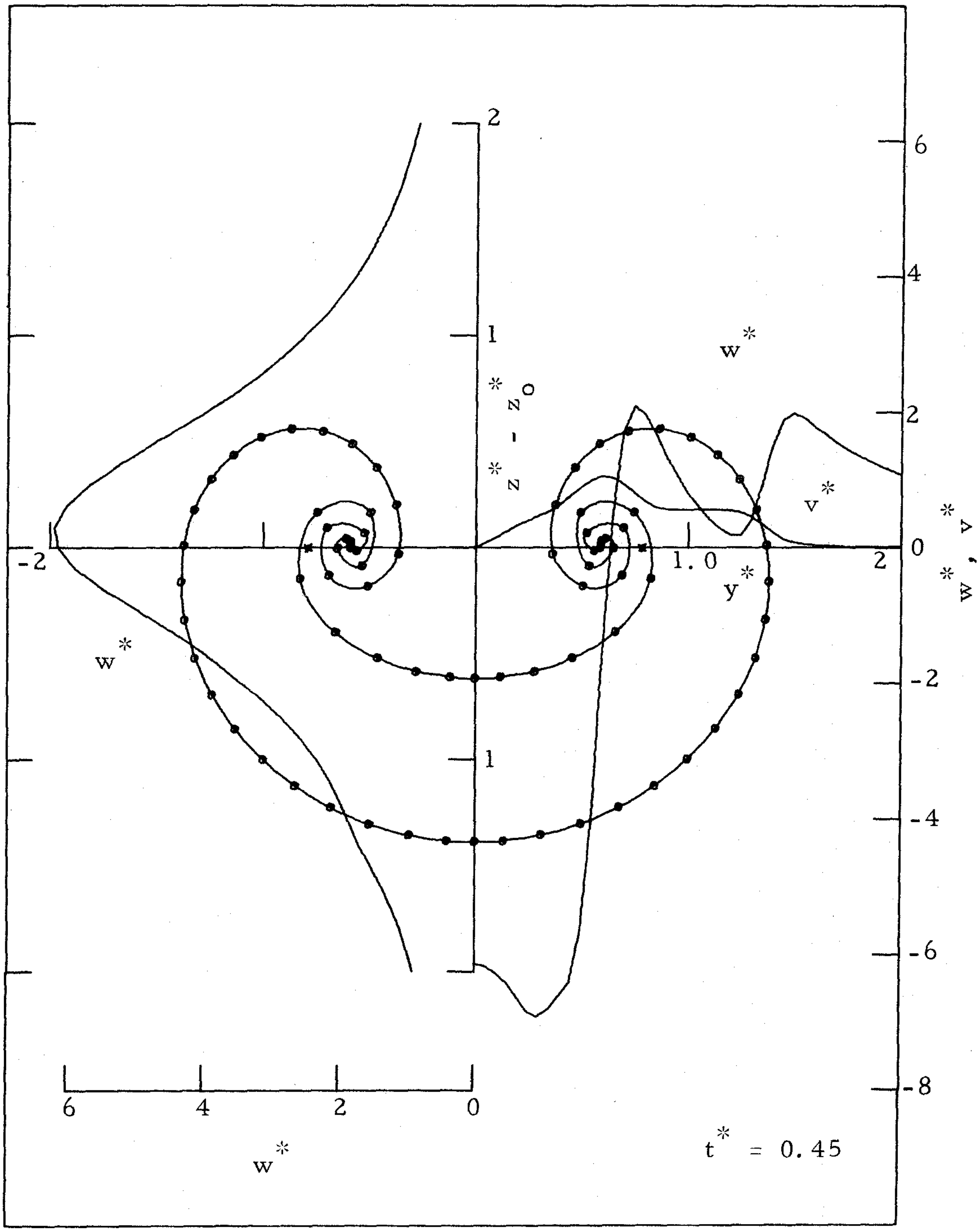

Figure 23e. Numerically Calculated Velocity Profiles in Rolled-up Vortex Sheet

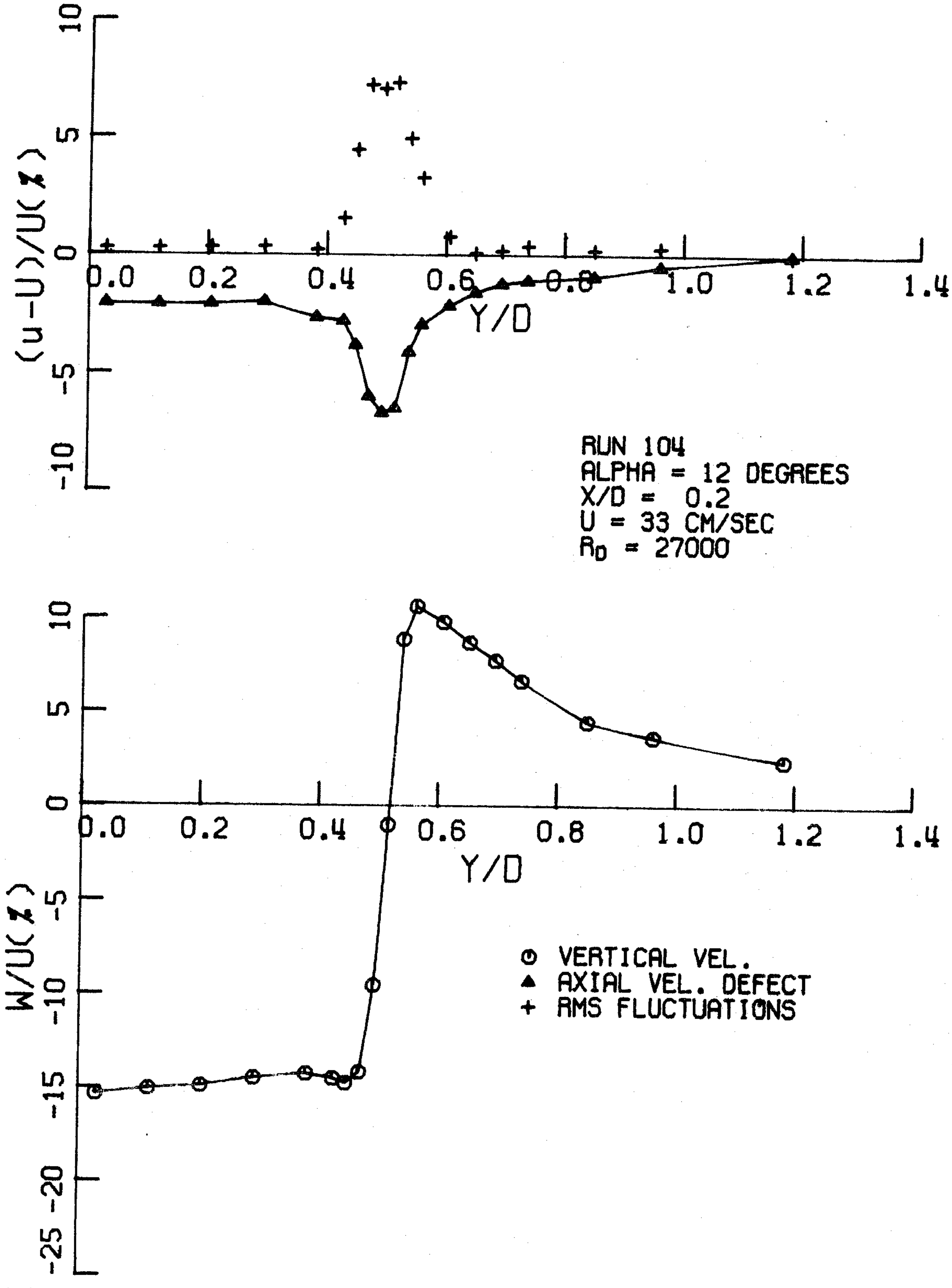

FIG.24a VELOCITY PROFILES IN VORTEX (RING WING)

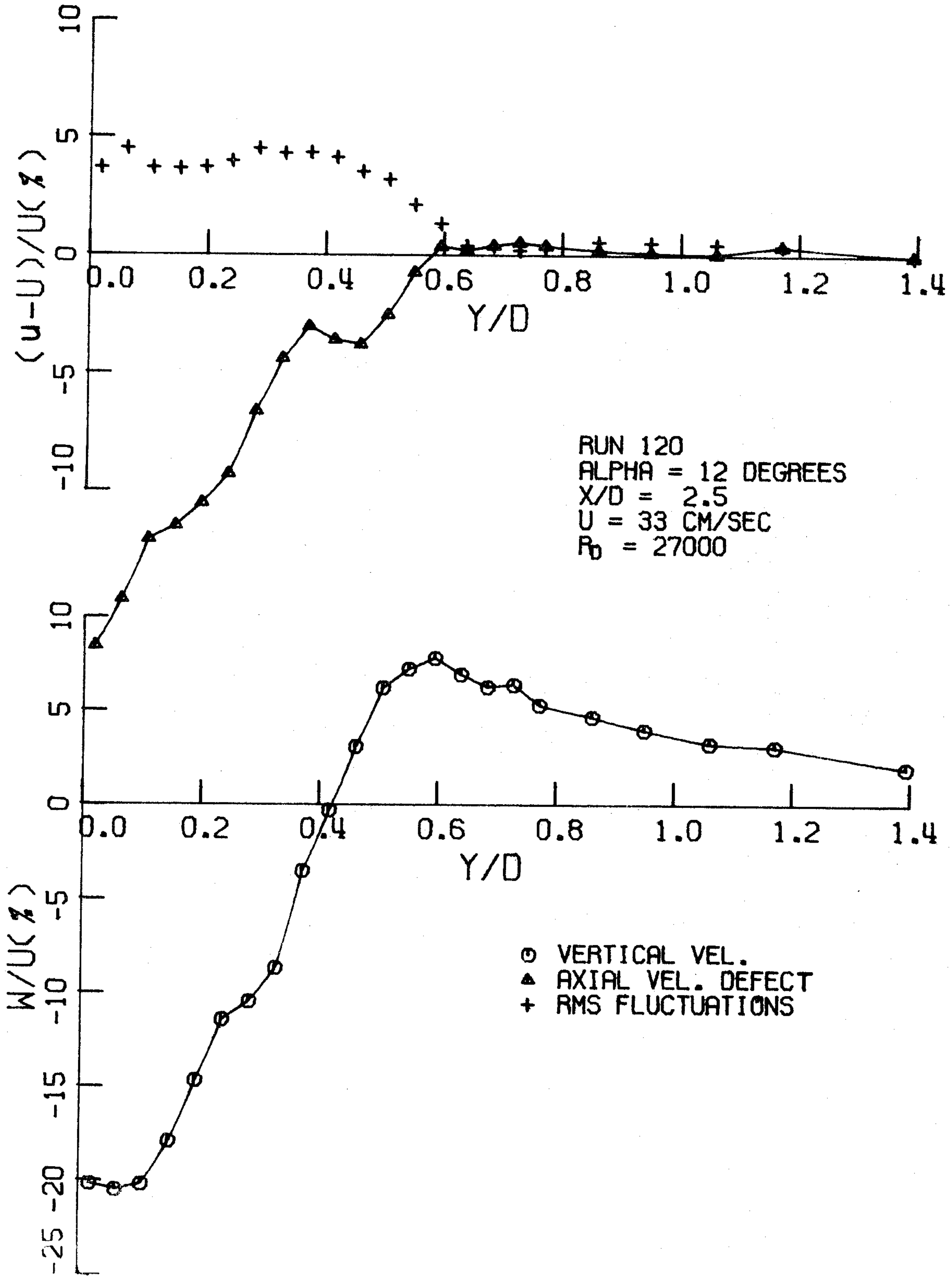

FIG.24b VELOCITY PROFILES IN VORTEX (RING WING)

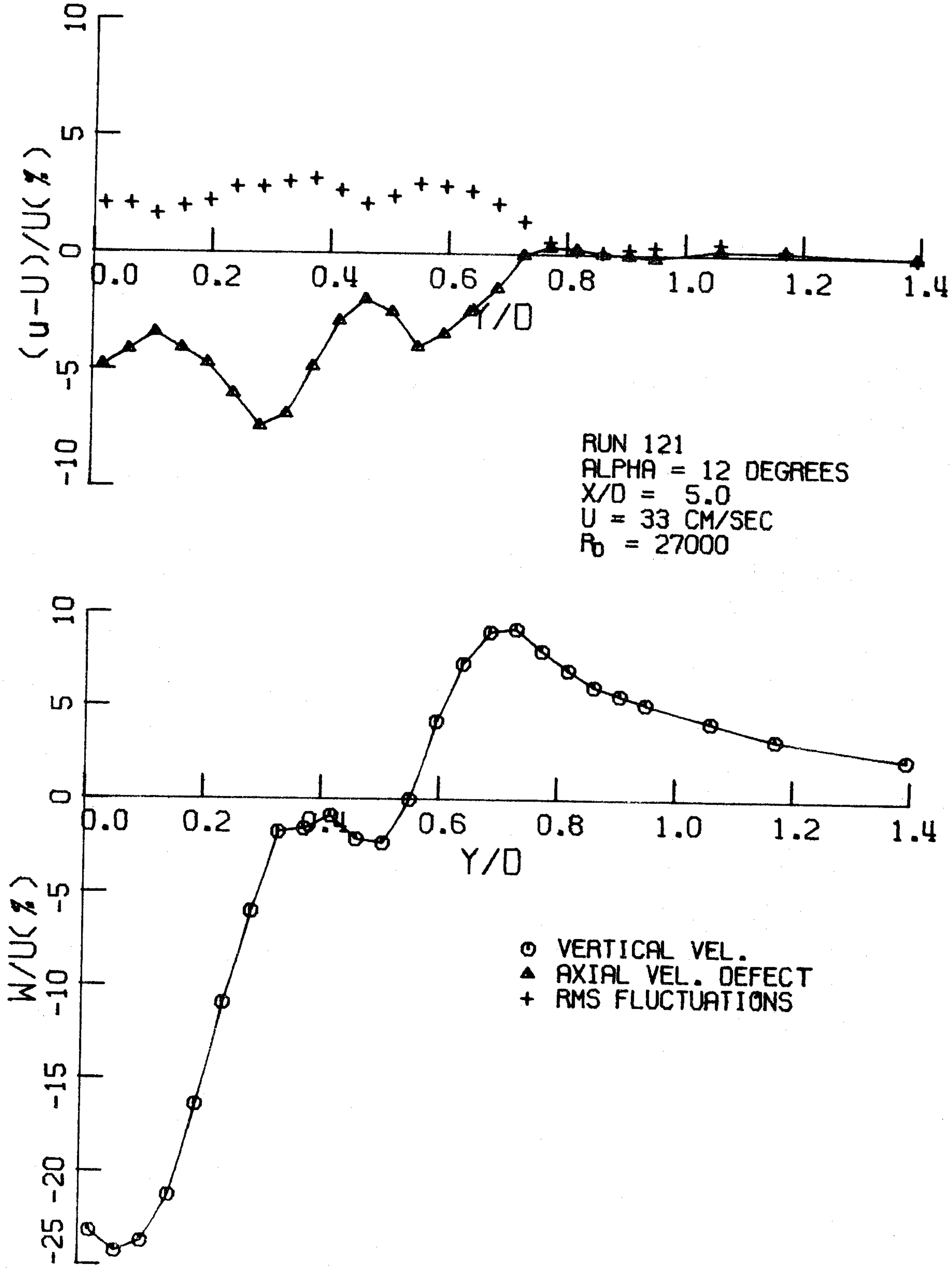

FIG. 24c VELOCITY PROFILES IN VORTEX (RING WING)

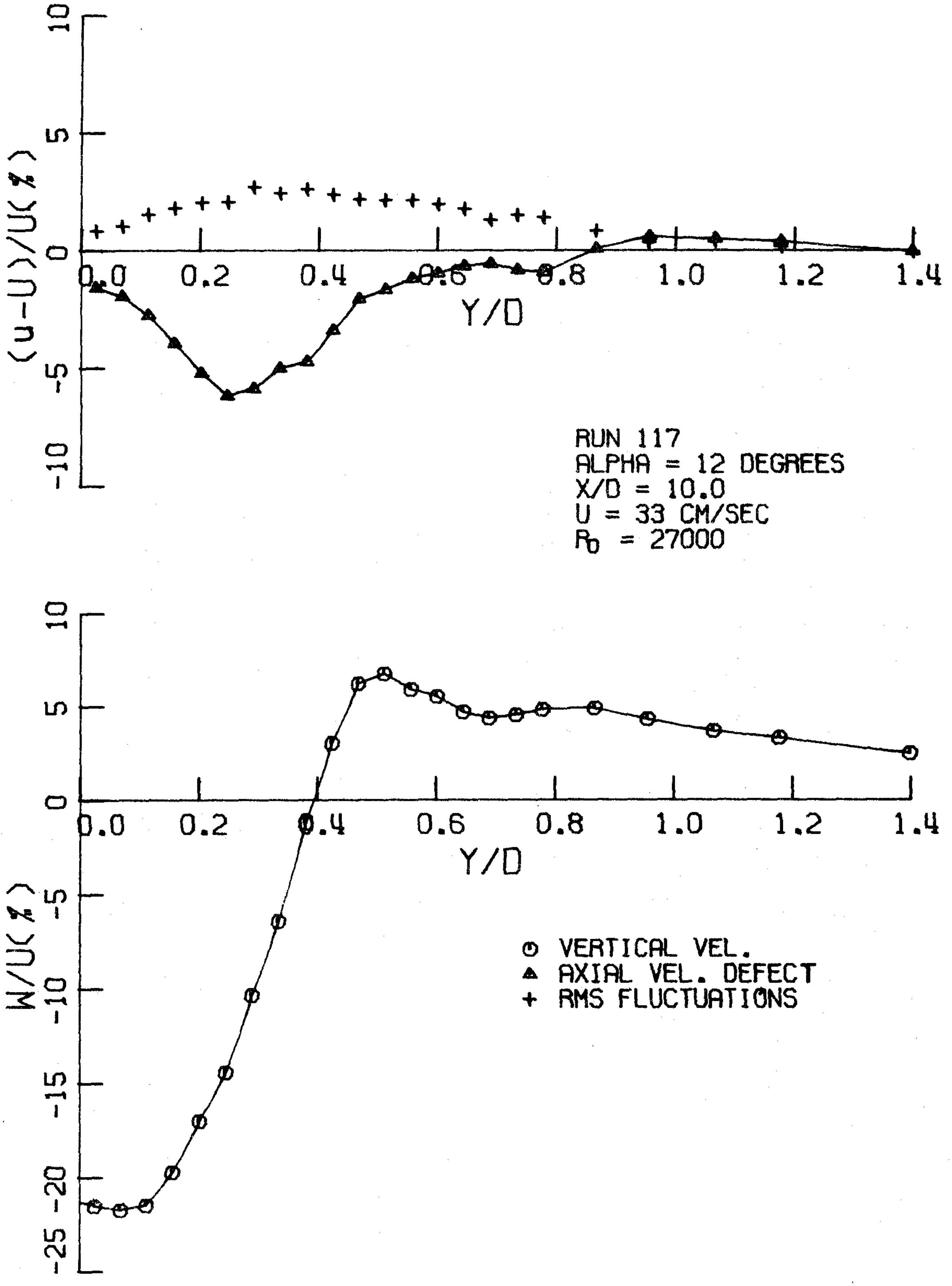

FIG.24d VELOCITY PROFILES IN VORTEX (RING WING)

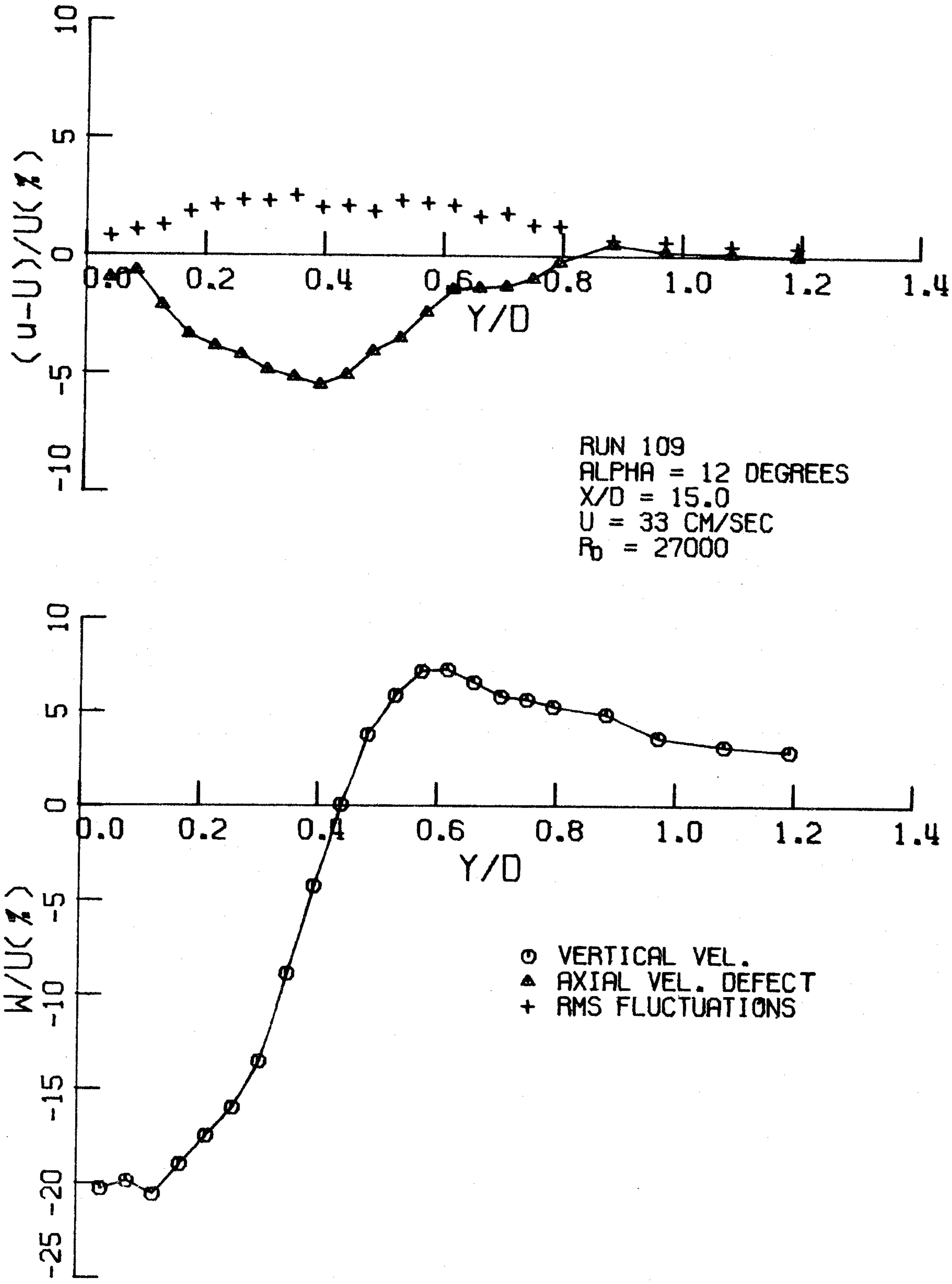

RUN 109
ALPHA = 12 DEGREES
X/D = 15.0
U = 33 CM/SEC
R_D = 27000

FIG.24e VELOCITY PROFILES IN VORTEX (RING WING)

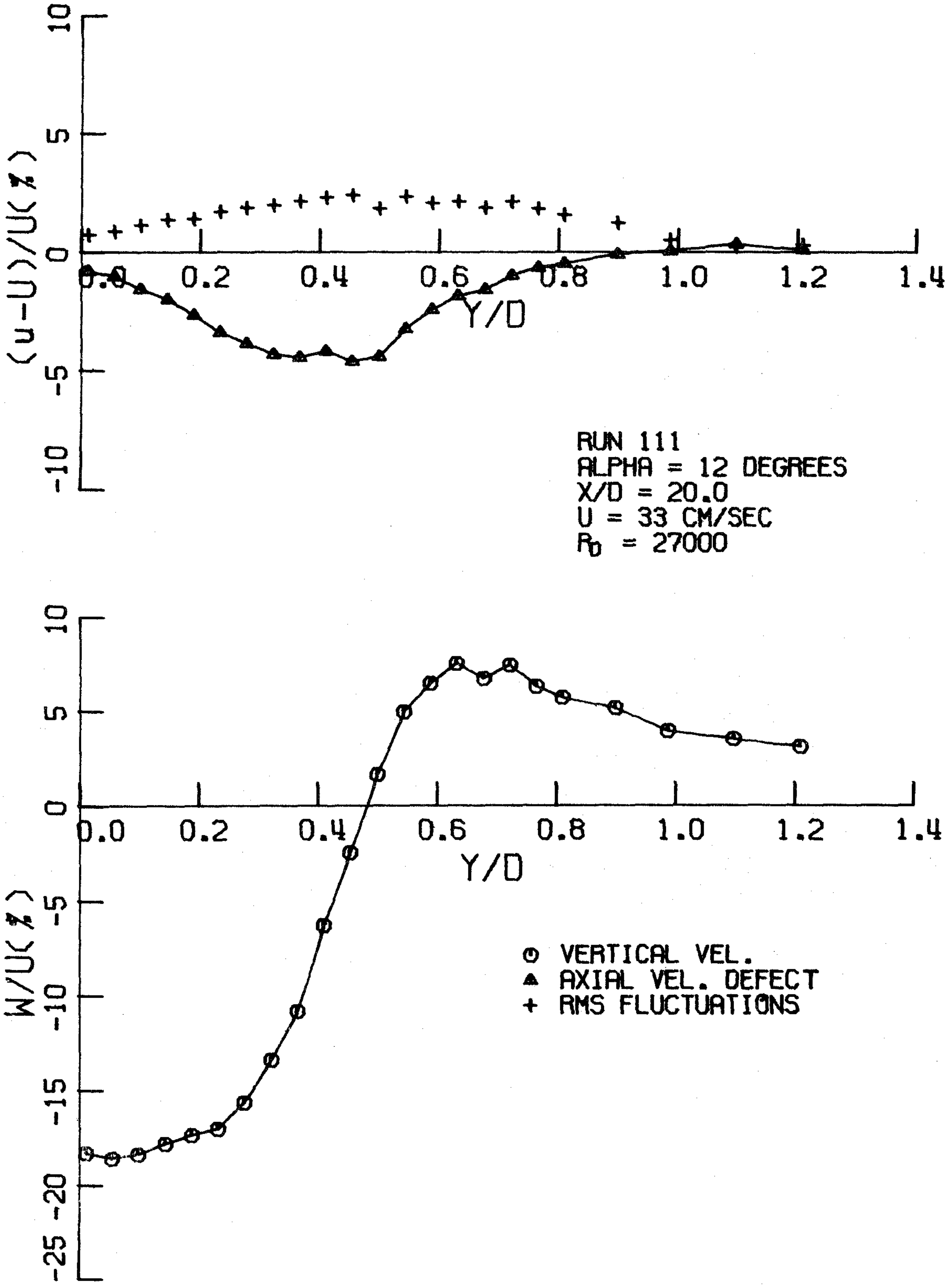

RUN 111
ALPHA = 12 DEGREES
X/D = 20.0
U = 33 CM/SEC
R_D = 27000

FIG.24f VELOCITY PROFILES IN VORTEX (RING WING)

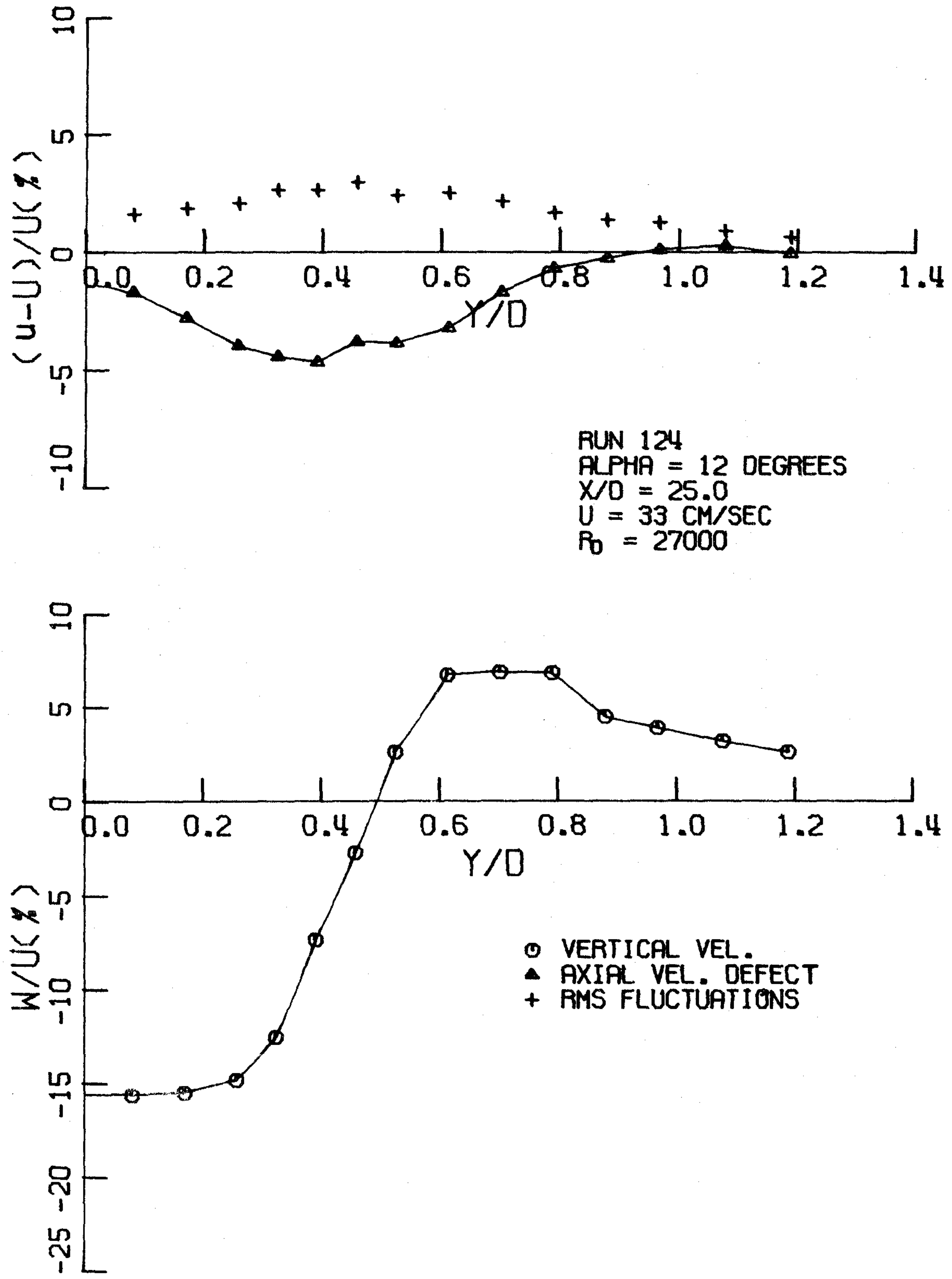

FIG.24g VELOCITY PROFILES IN VORTEX (RING WING)

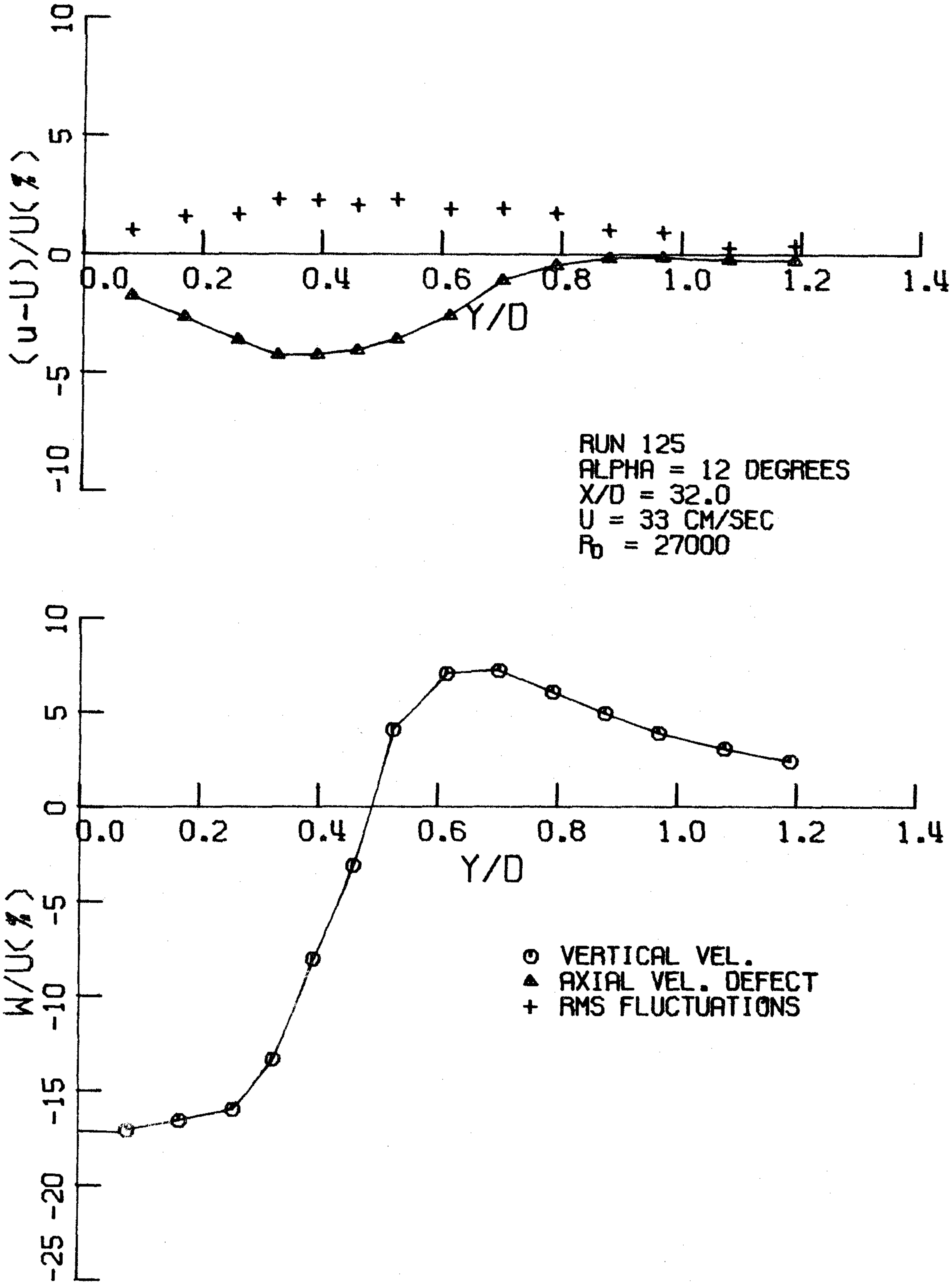

RUN 125
ALPHA = 12 DEGREES
X/D = 32.0
U = 33 CM/SEC
R_D = 27000

FIG.24h VELOCITY PROFILES IN VORTEX (RING WING)

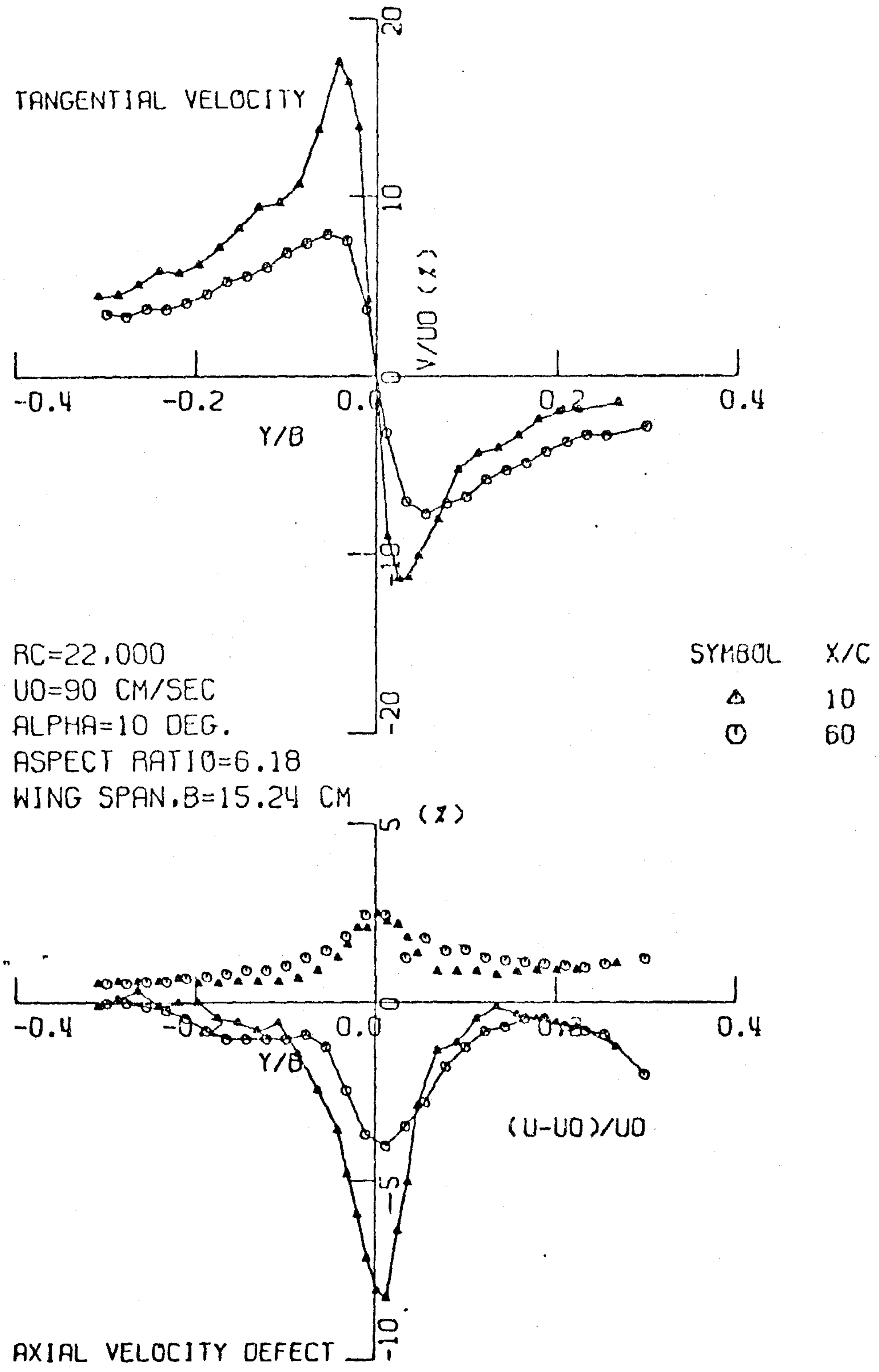

Fig. 24i. **Velocity profiles in trailing vortex.**
(Rectangular Wing, Ref. 25)

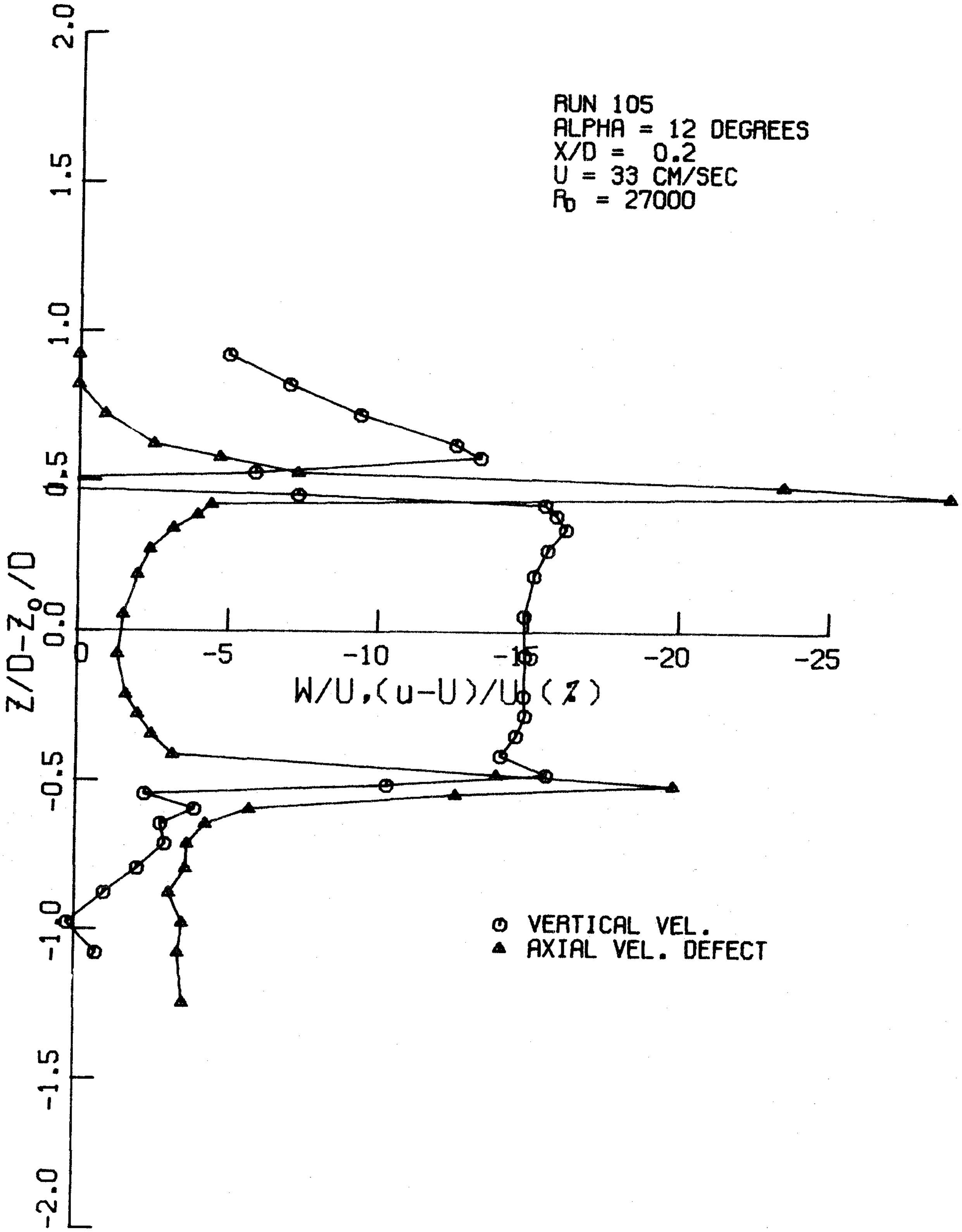

FIG.25a VELOCITY PROFILES IN PLANE OFSYMMETRY

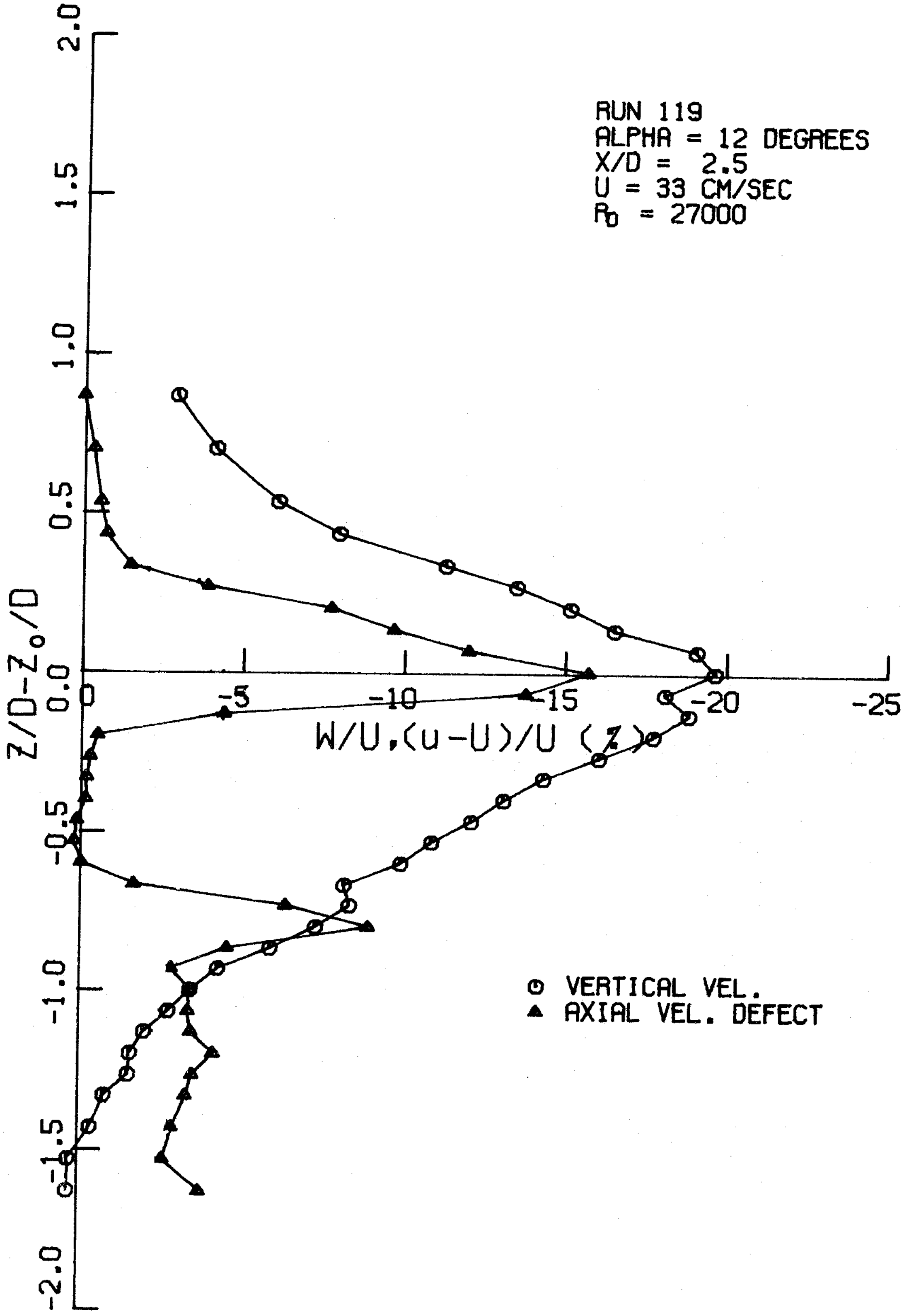

FIG. 25b VELOCITY PROFILES IN PLANE OFSYMMETRY

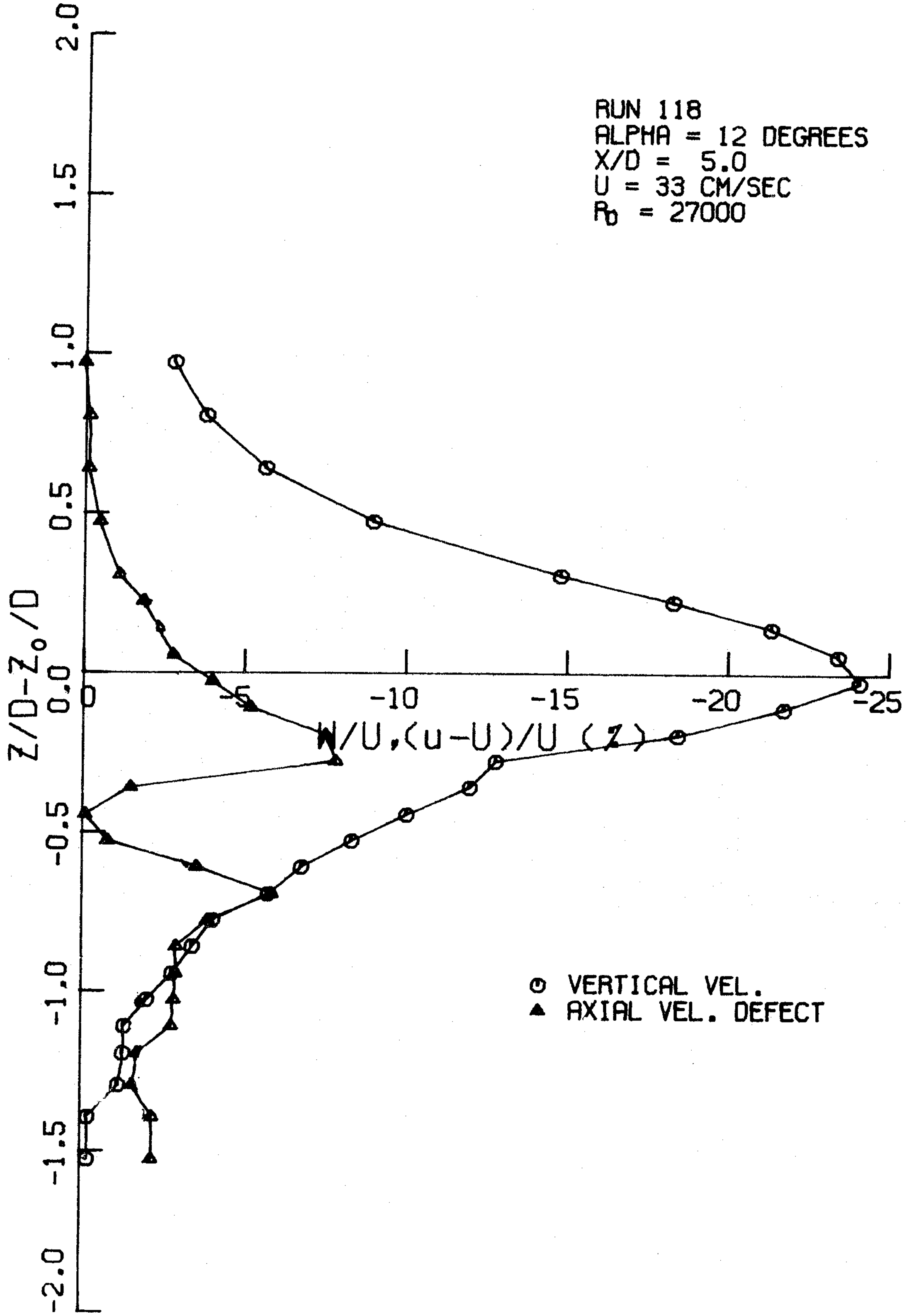

FIG. 25c VELOCITY PROFILES IN PLANE OFSYMMETRY

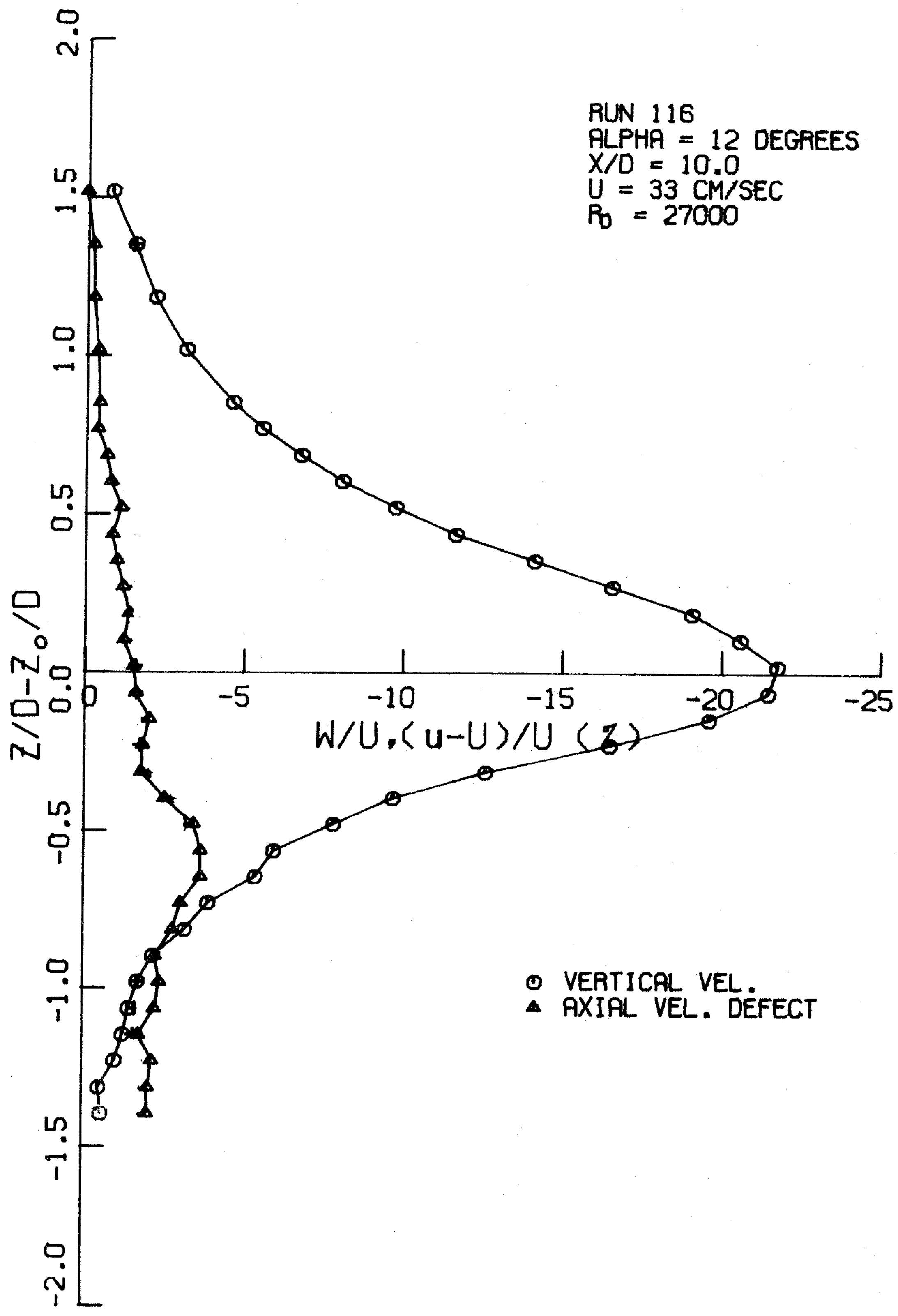

FIG. 25d VELOCITY PROFILES IN PLANE OFSYMMETRY

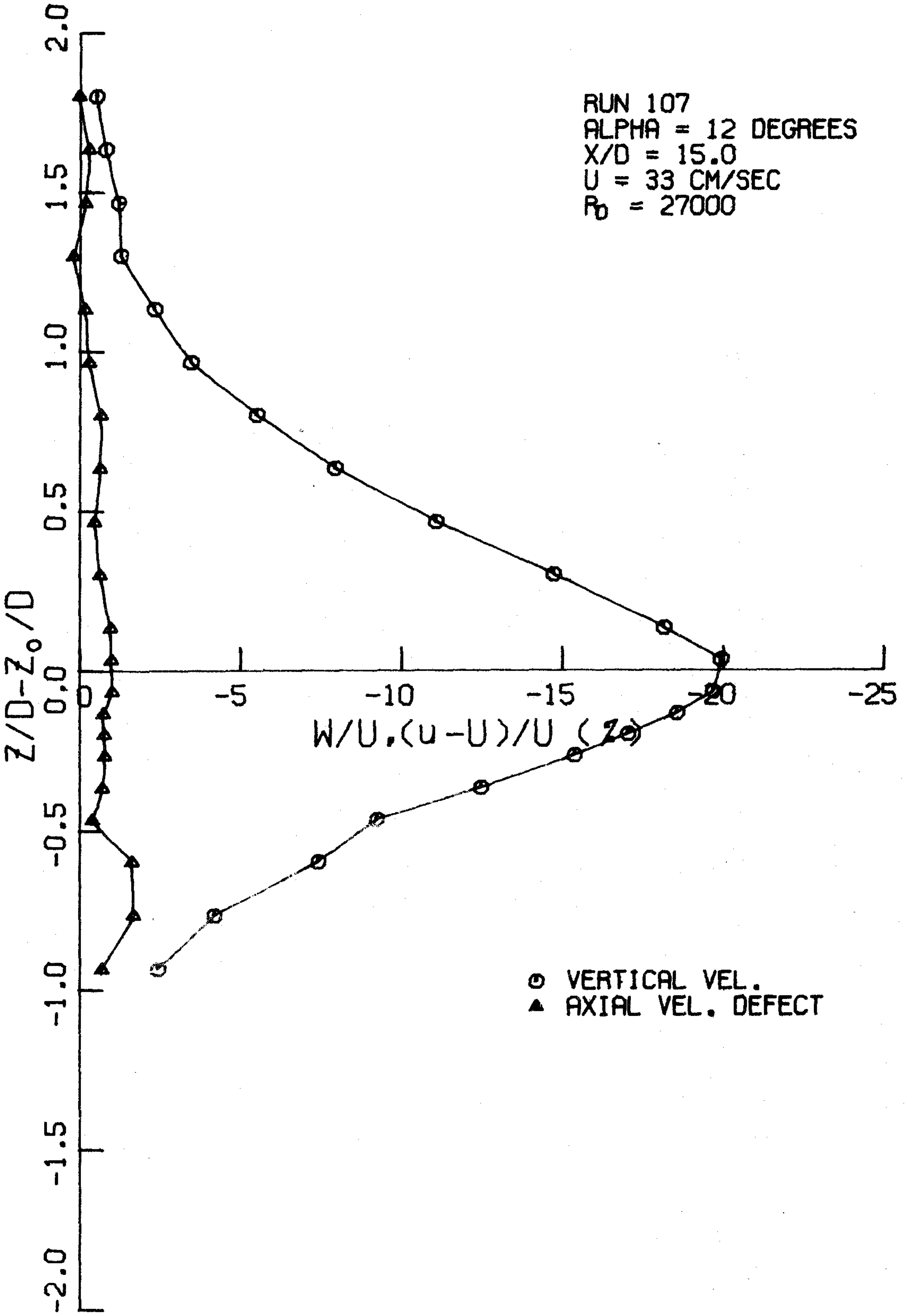

FIG. 25e VELOCITY PROFILES IN PLANE OFSYMMETRY

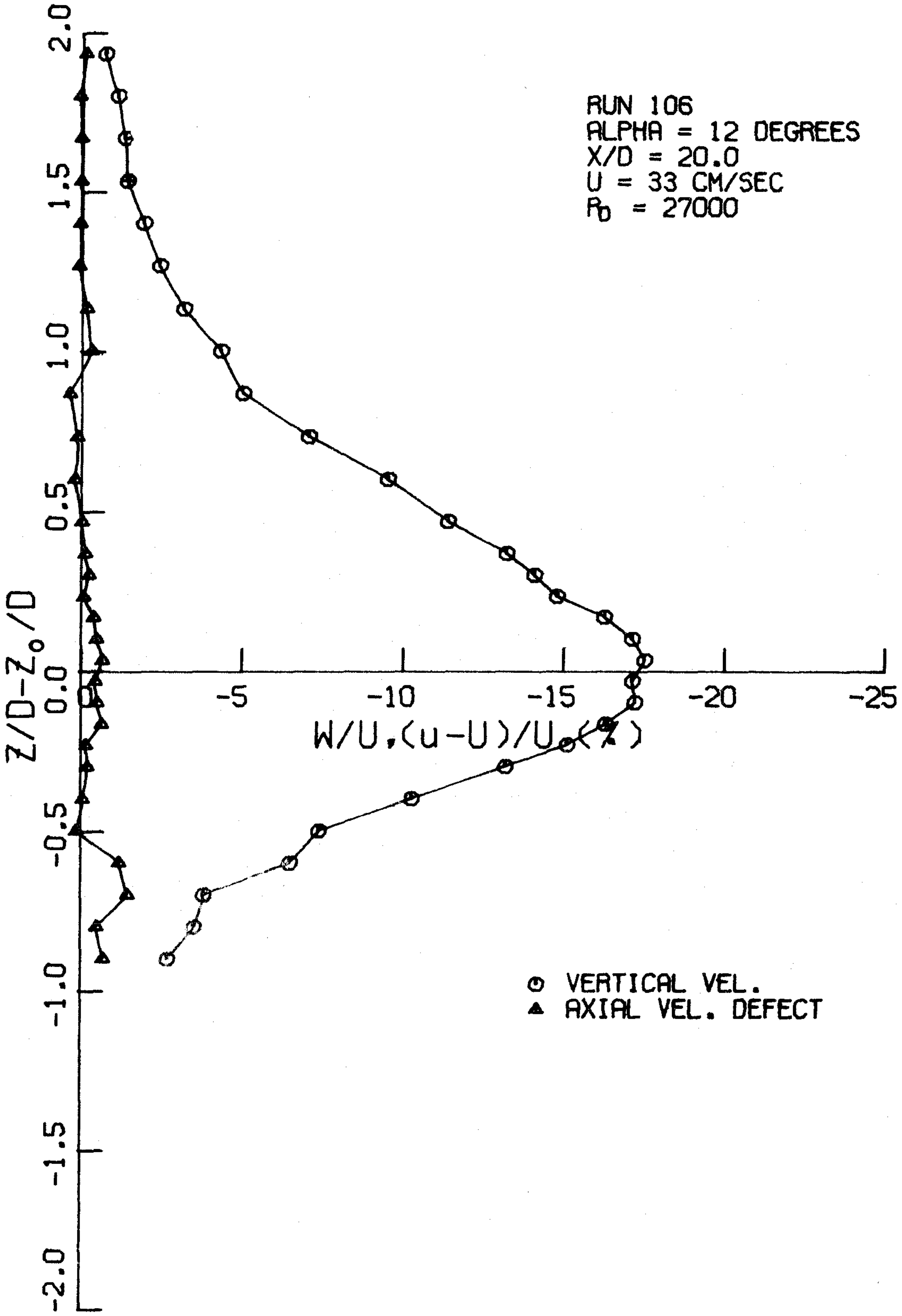

FIG. 25f VELOCITY PROFILES IN PLANE OFSYMMETRY

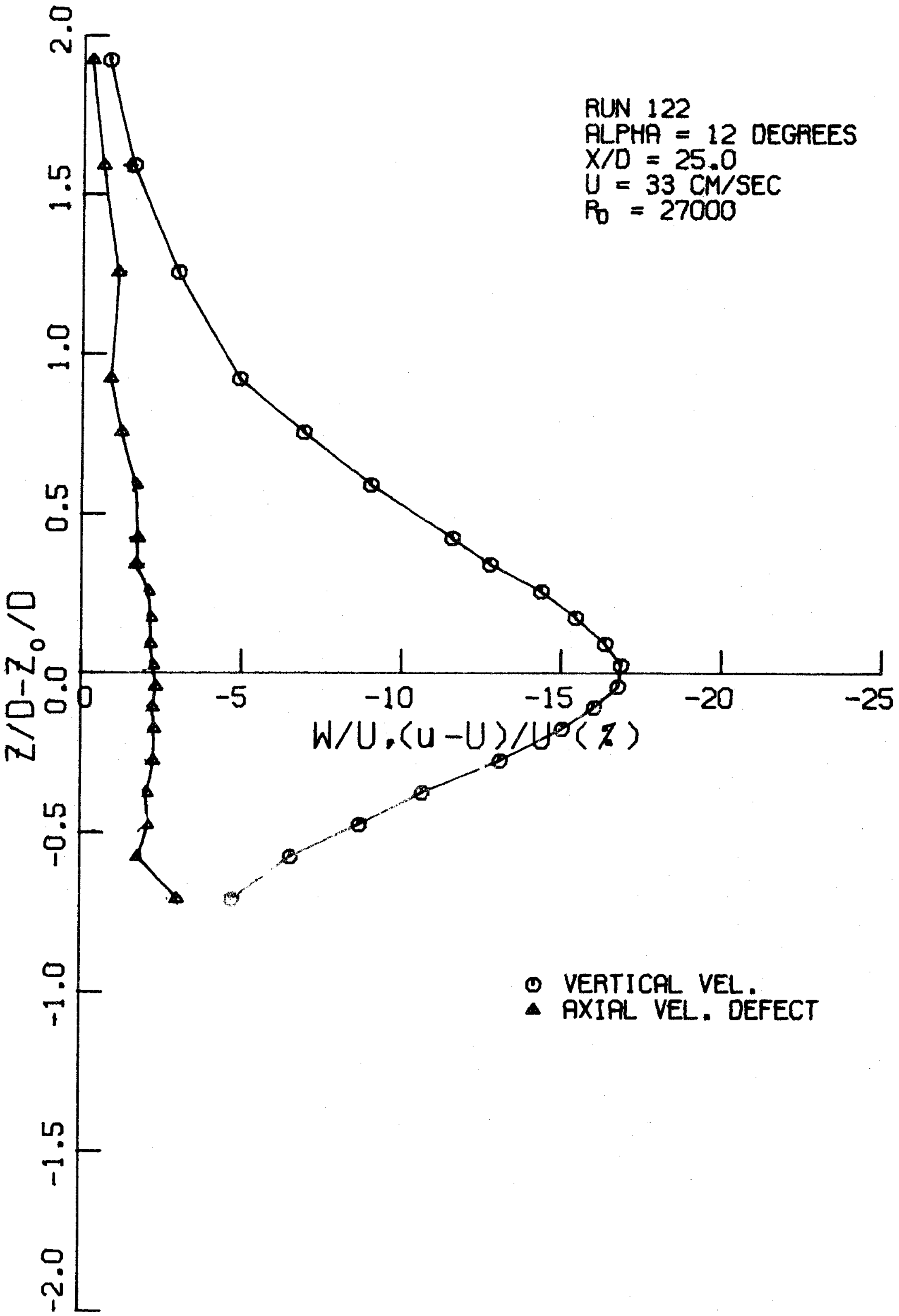

FIG.25g VELOCITY PROFILES IN PLANE OFSYMMETRY

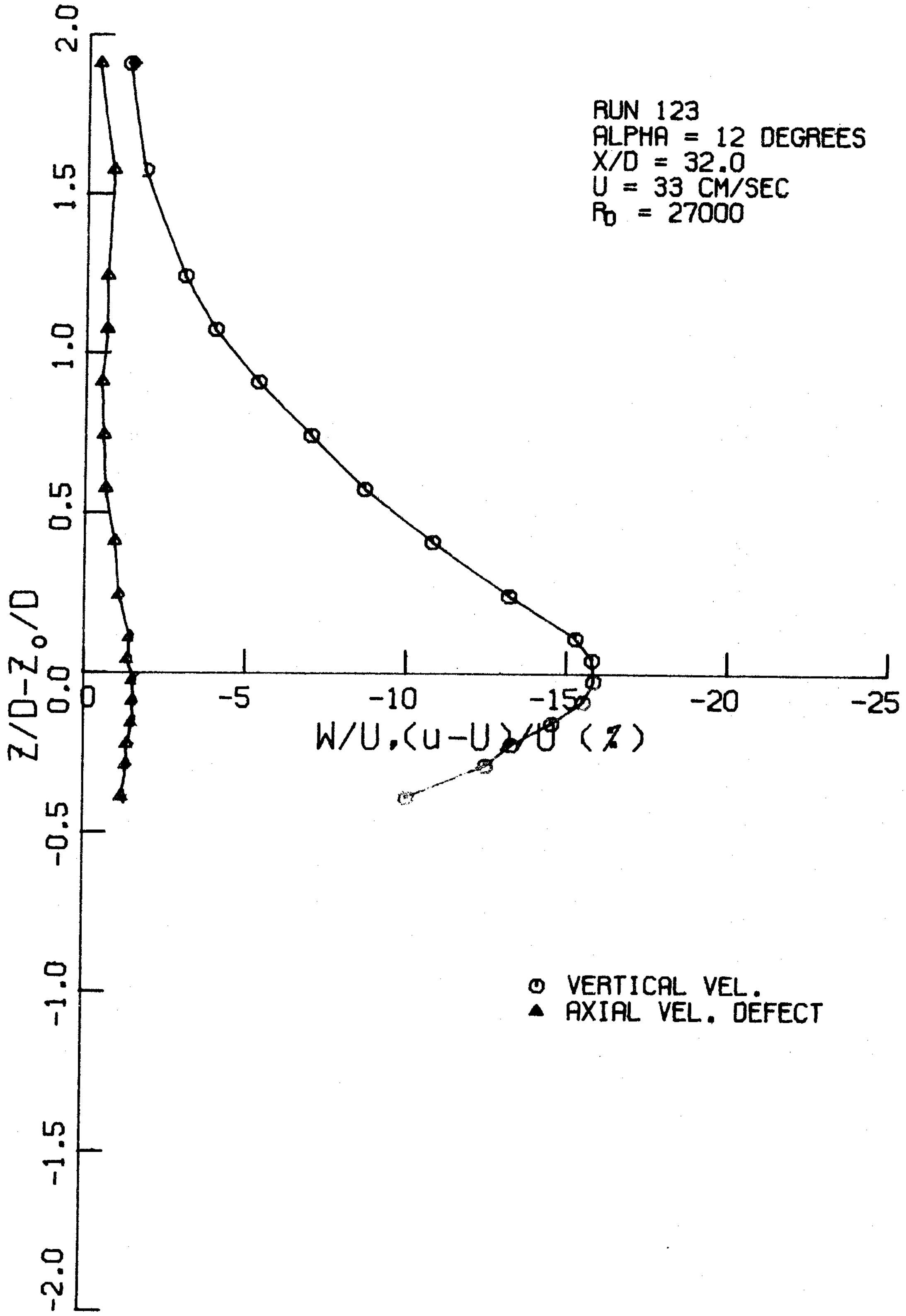

FIG. 25h VELOCITY PROFILES IN PLANE OF SYMMETRY

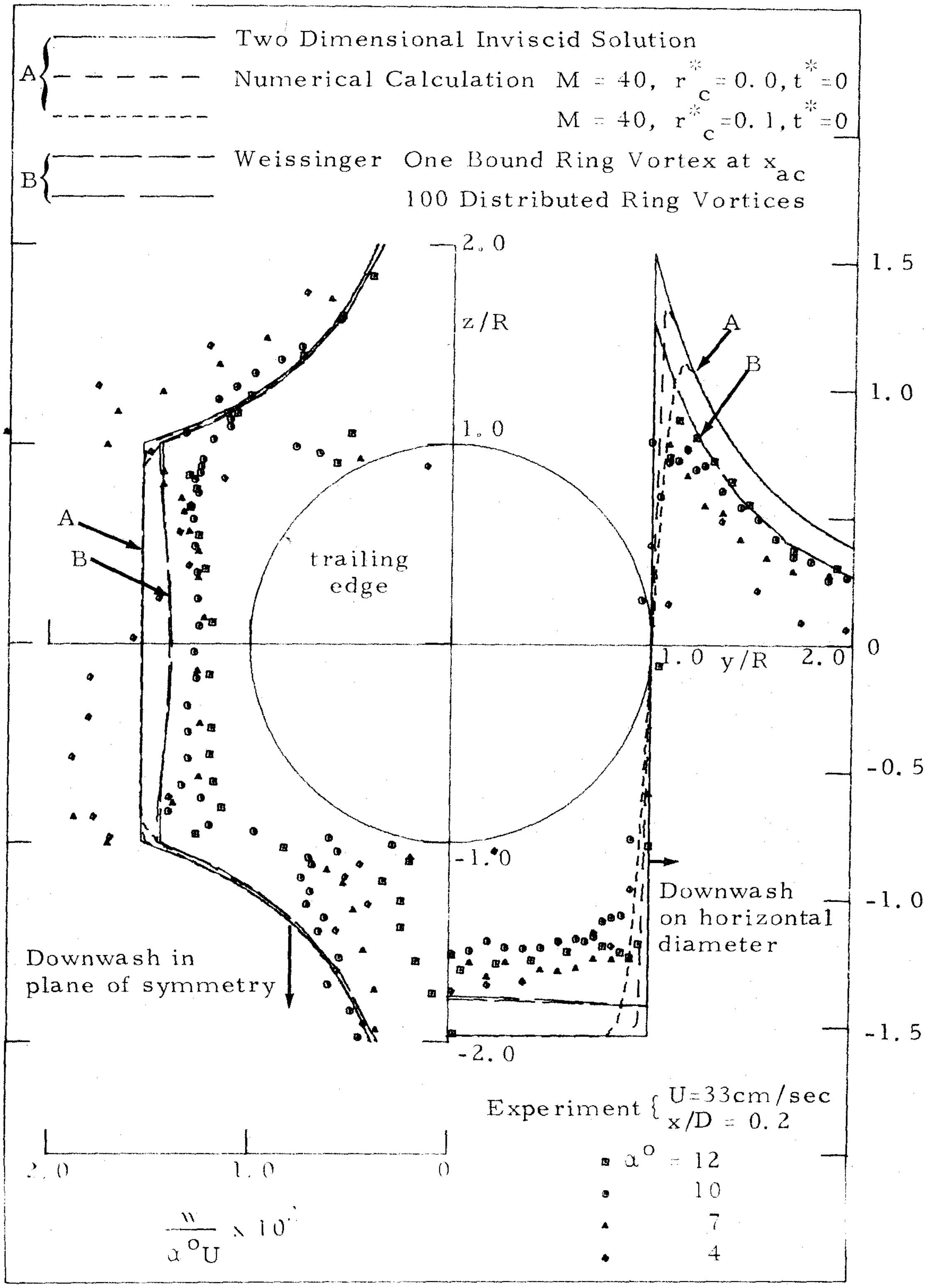

Figure 26. Comparison of Velocity Profiles Near Trailing Edge of Ring Wing.

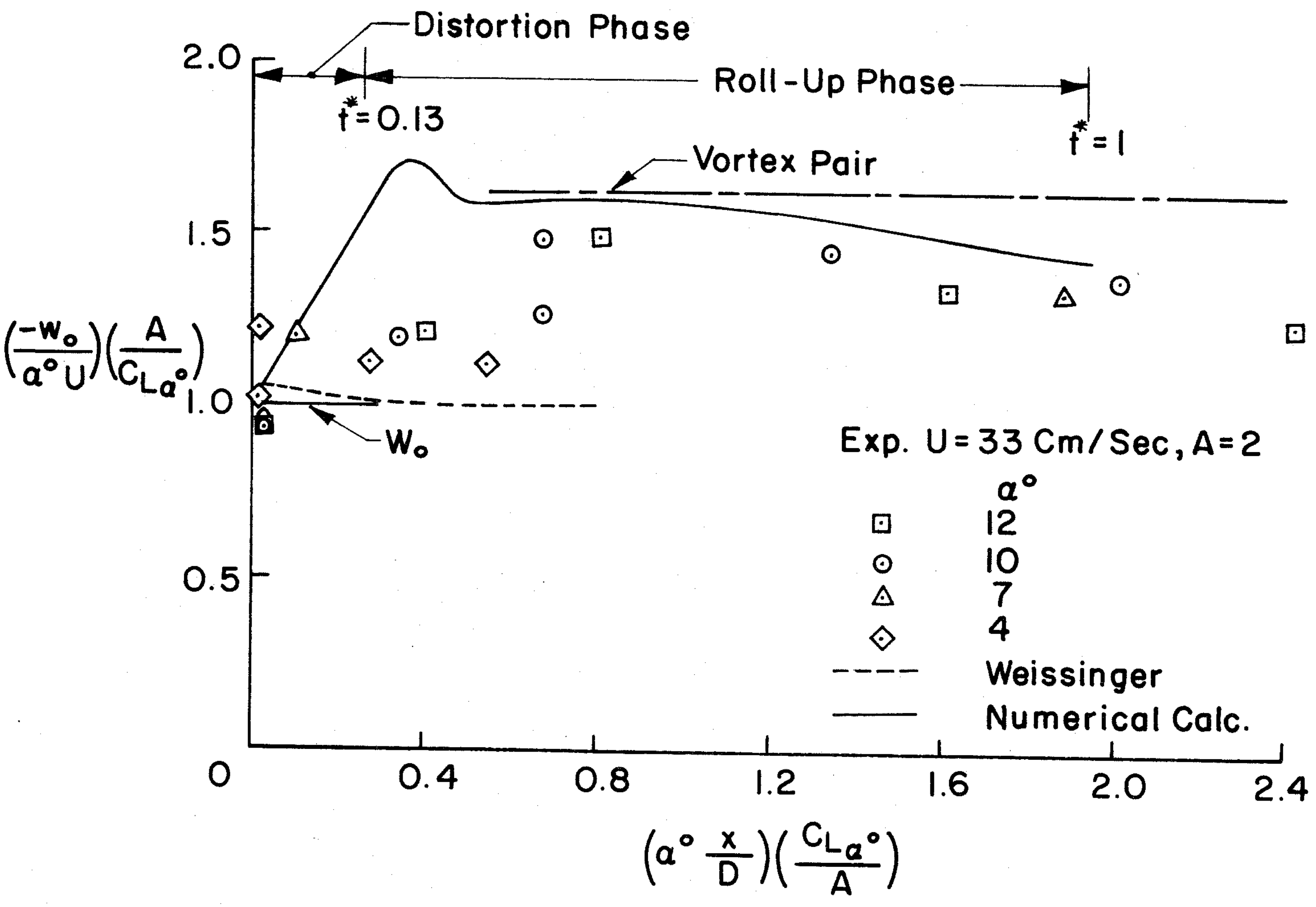

FIG. 27 MAXIMUM DOWNWASH IN PLANE OF SYMMETRY DURING ROLL-UP

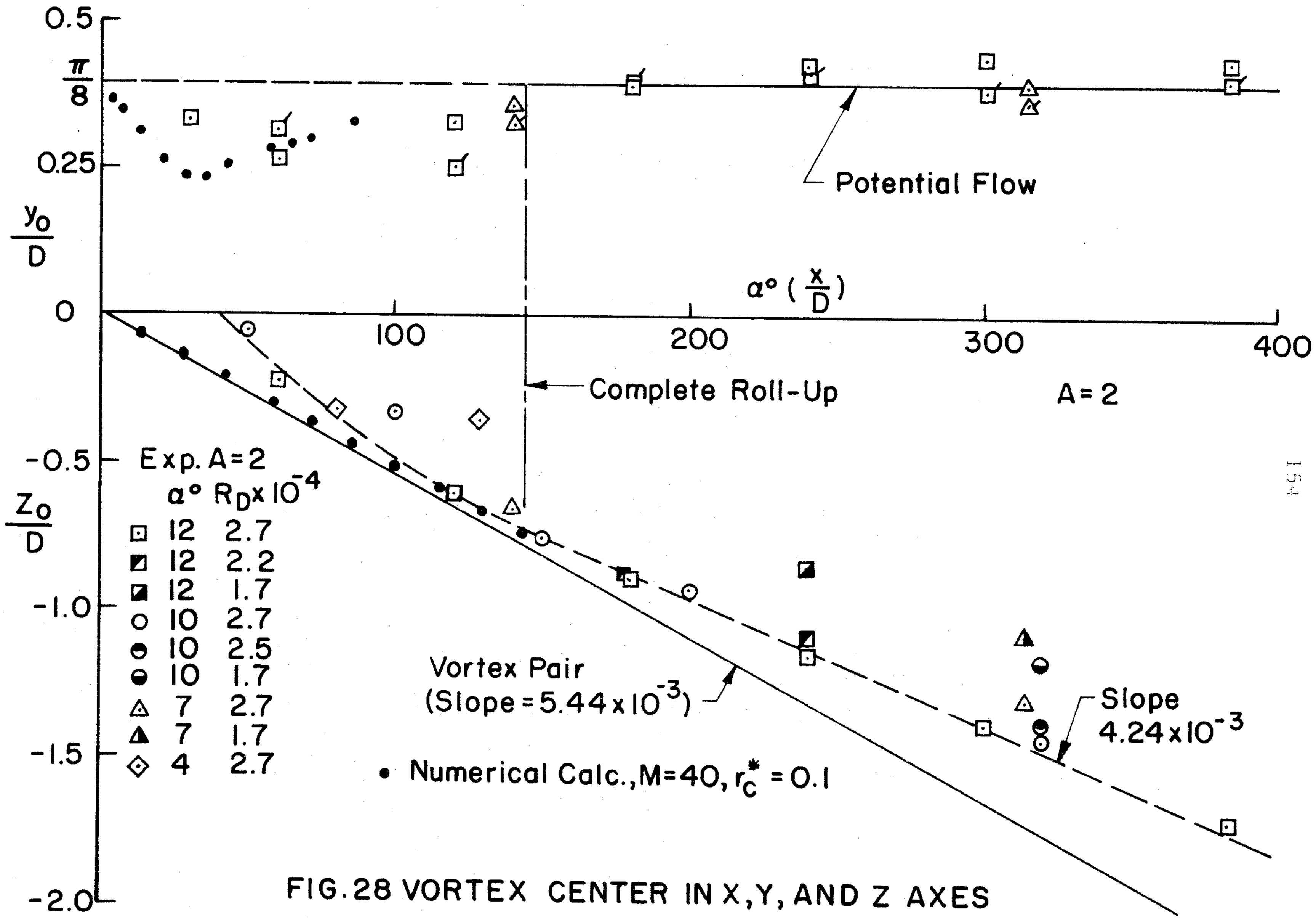

FIG. 28 VORTEX CENTER IN X, Y, AND Z AXES

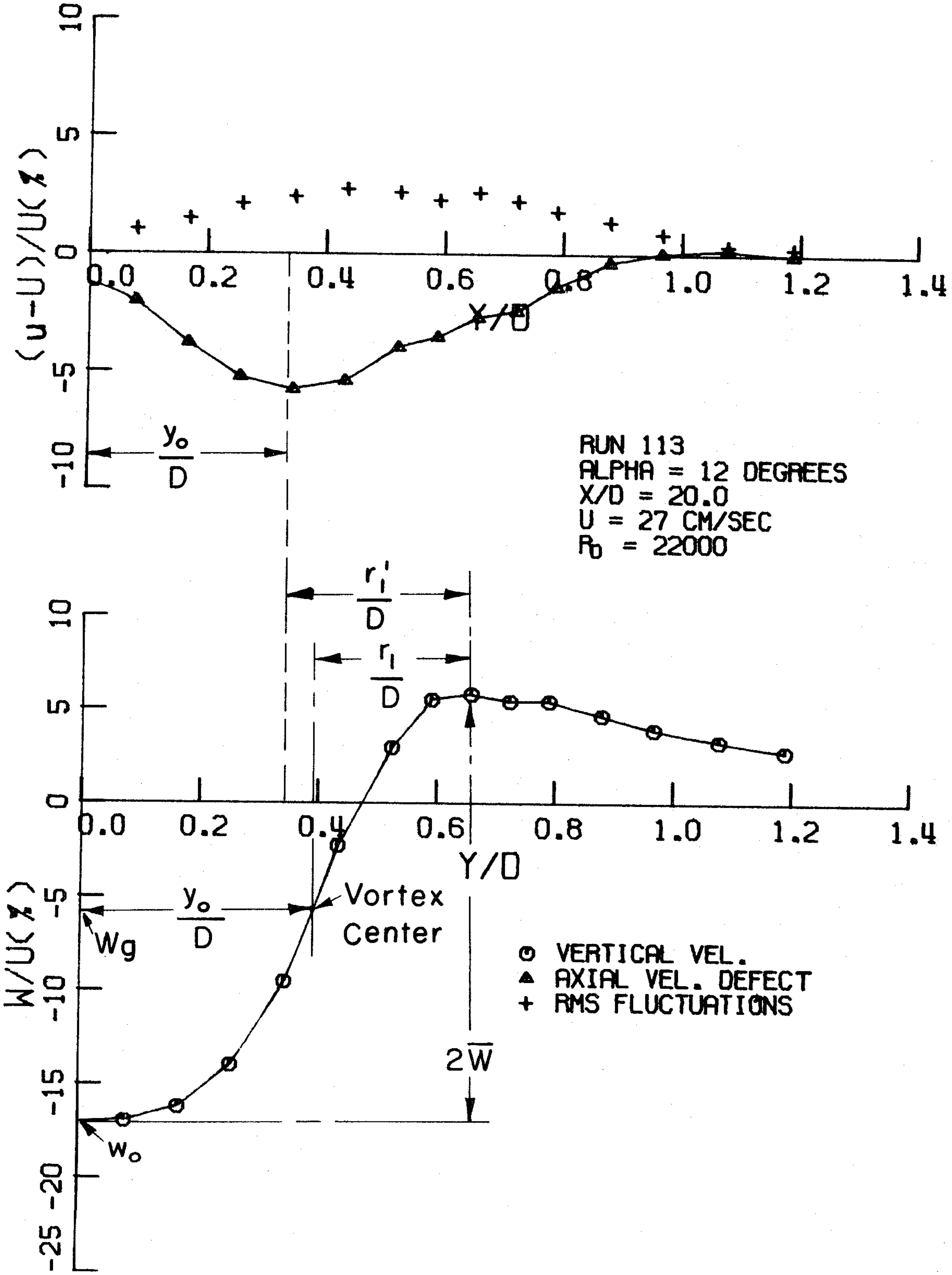

FIG. 29 DEFINITION OF VORTEX CORE

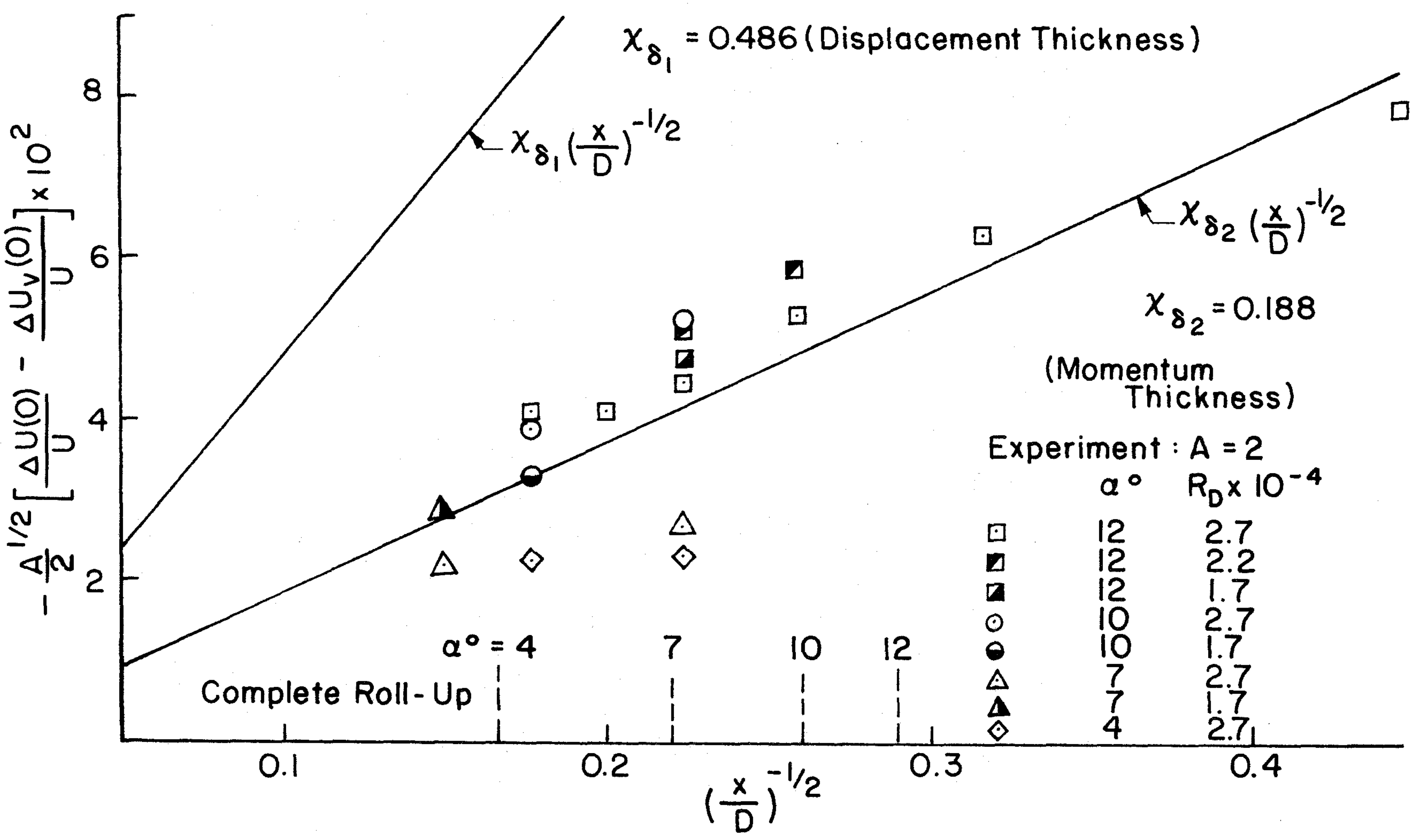

FIG.30 DIMENSIONLESS AXIAL VELOCITY DEFECT ON VORTEX CORE AS FUNCTION OF DOWNSTREAM DISTANCE

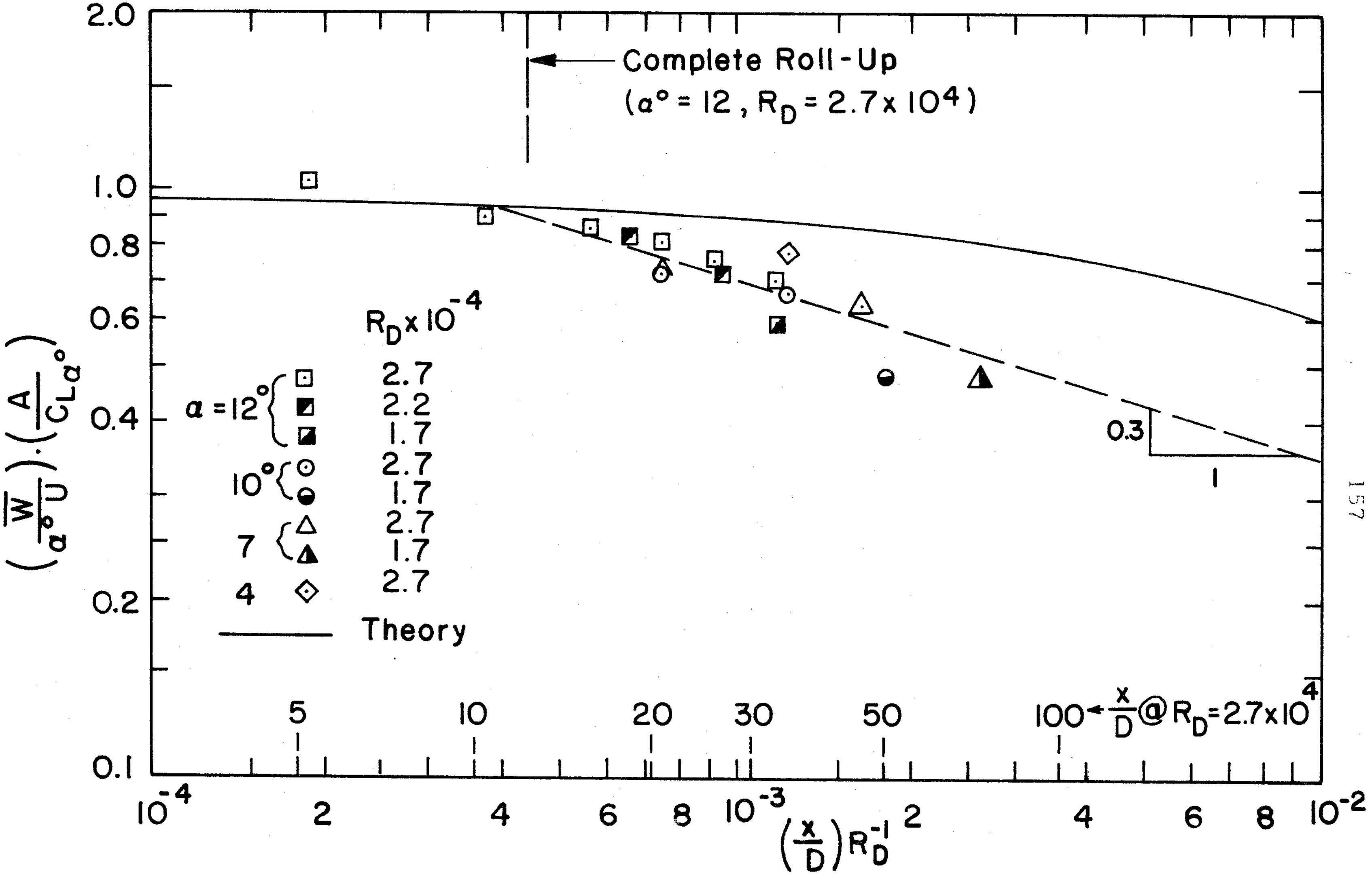

FIG. 31 DIMENSIONLESS PEAK TANGENTIAL VELOCITY AS A FUNCTION OF DOWNSTREAM DISTANCE AND REYNOLDS NUMBER

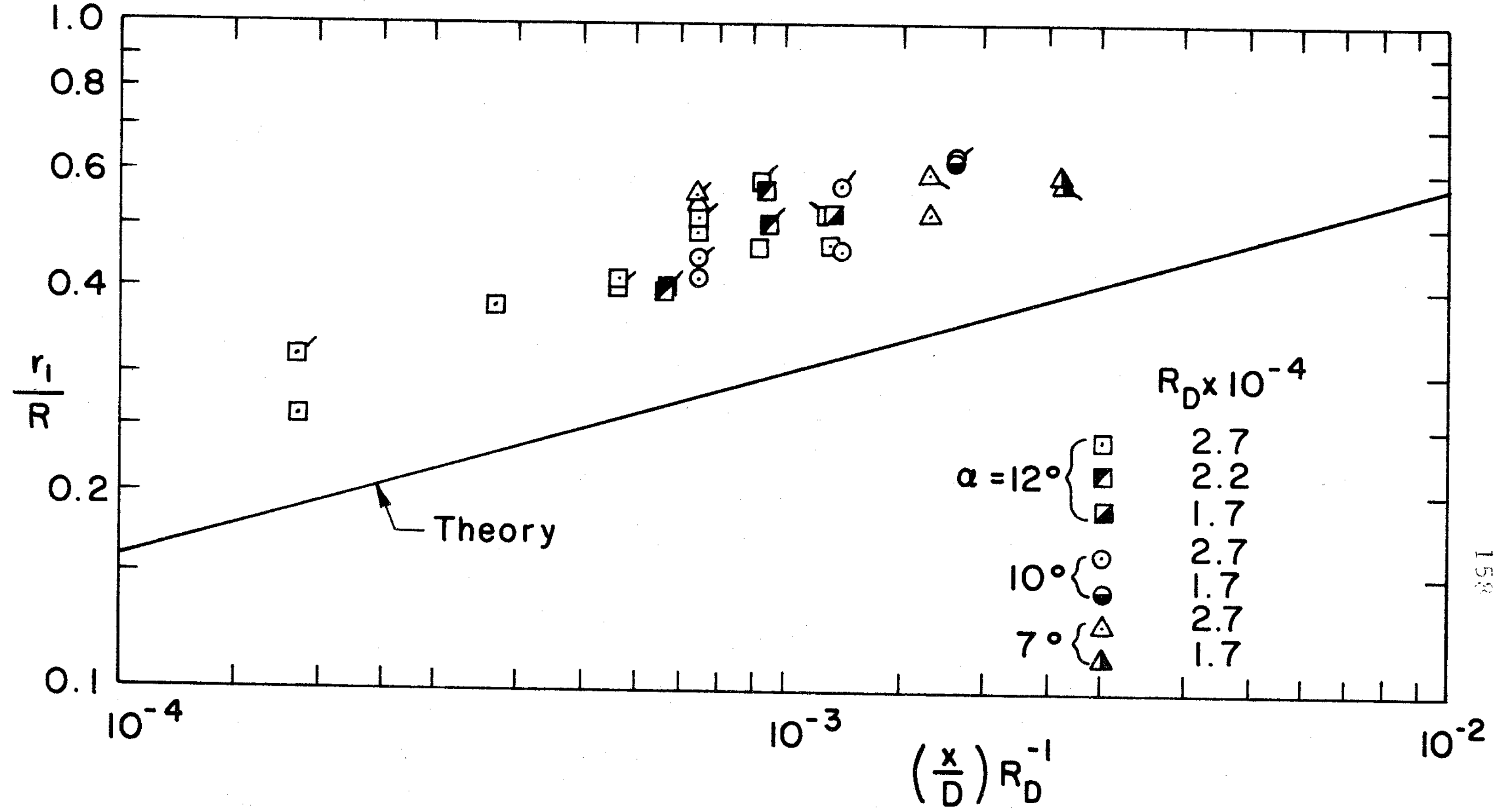

FIG. 32 VORTEX CORE RADIUS AS A FUNCTION OF DOWNSTREAM DISTANCE AND REYNOLDS NUMBER

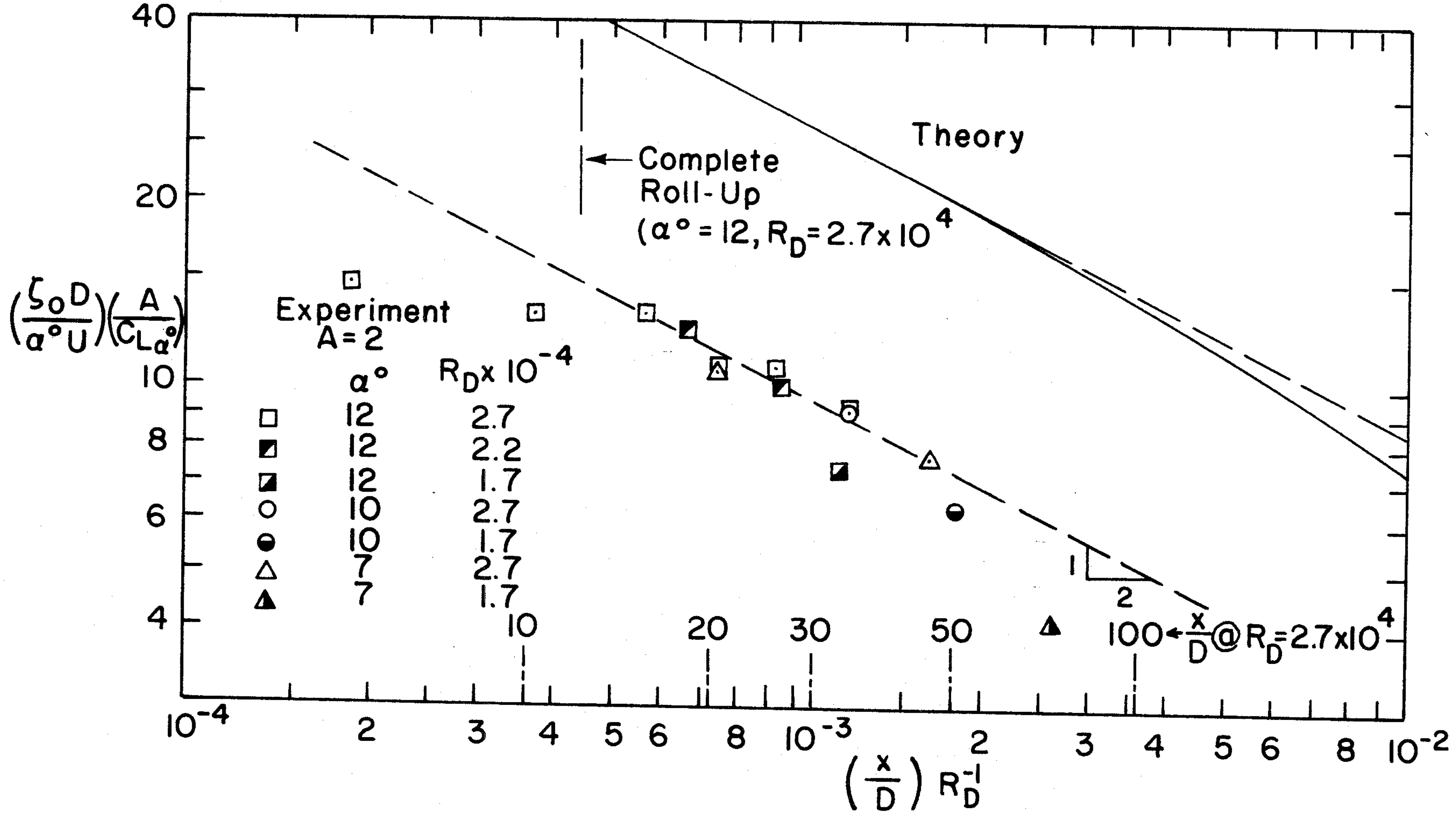

FIG. 33 DIMENSIONLESS AXIAL VORTICITY ON VORTEX CORE AXIS AS A FUNCTION OF DOWNSTREAM DISTANCE AND REYNOLDS NUMBER

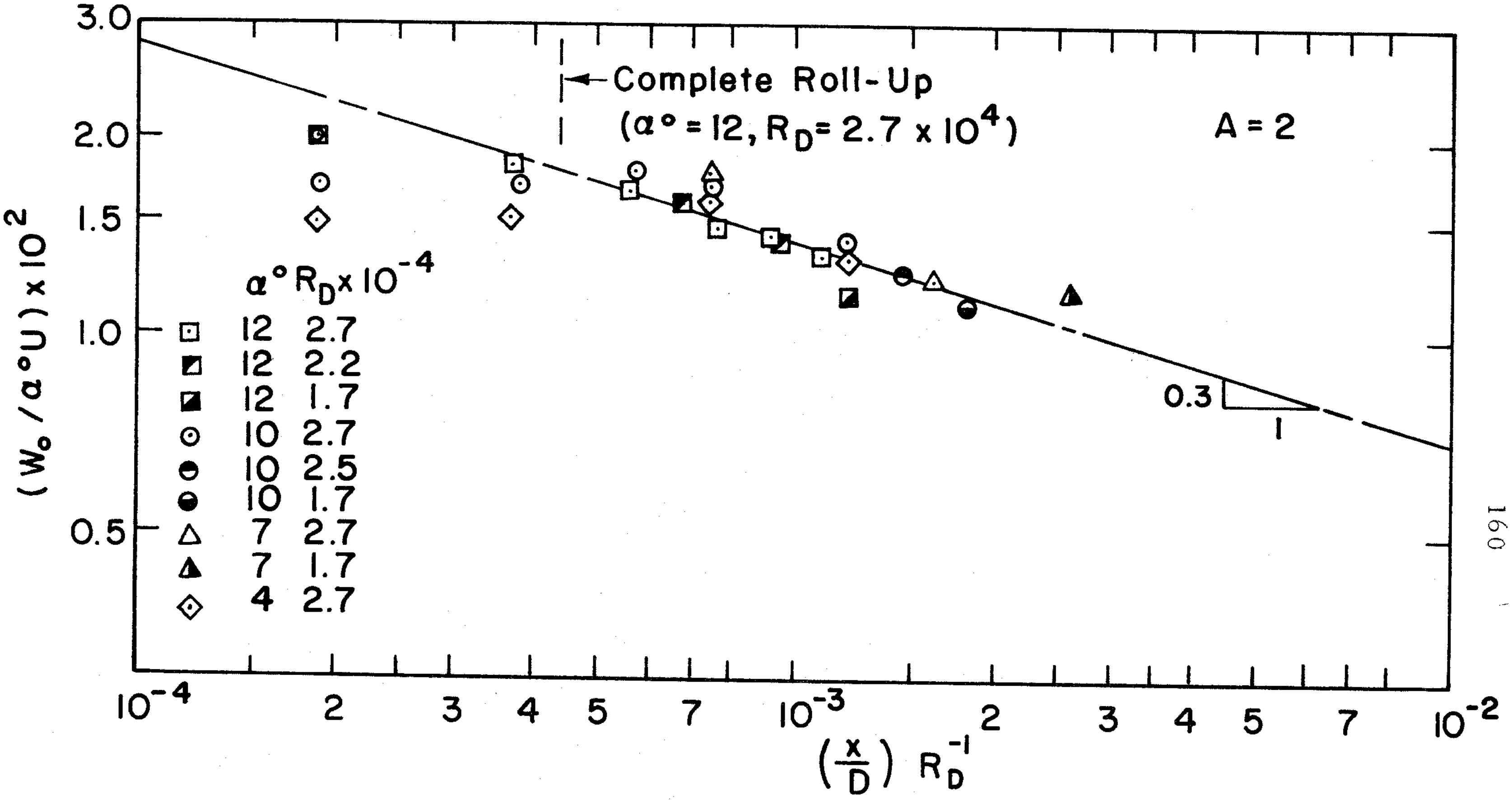

FIG. 34 MAXIMUM DOWNWASH AS FUNCTION OF DOWNSTREAM DISTANCE AND REYNOLDS NUMBER